



MSc in Physics

Spectral analysis of the CASSOWARY 31 lensing system

Hao Zhang

Supervised by Lise Bech Christensen

May 2023



Hao Zhang

Spectral analysis of the CASSOWARY 31 lensing system

MSc in Physics, May 2023

Supervisors: Lise Bech Christensen

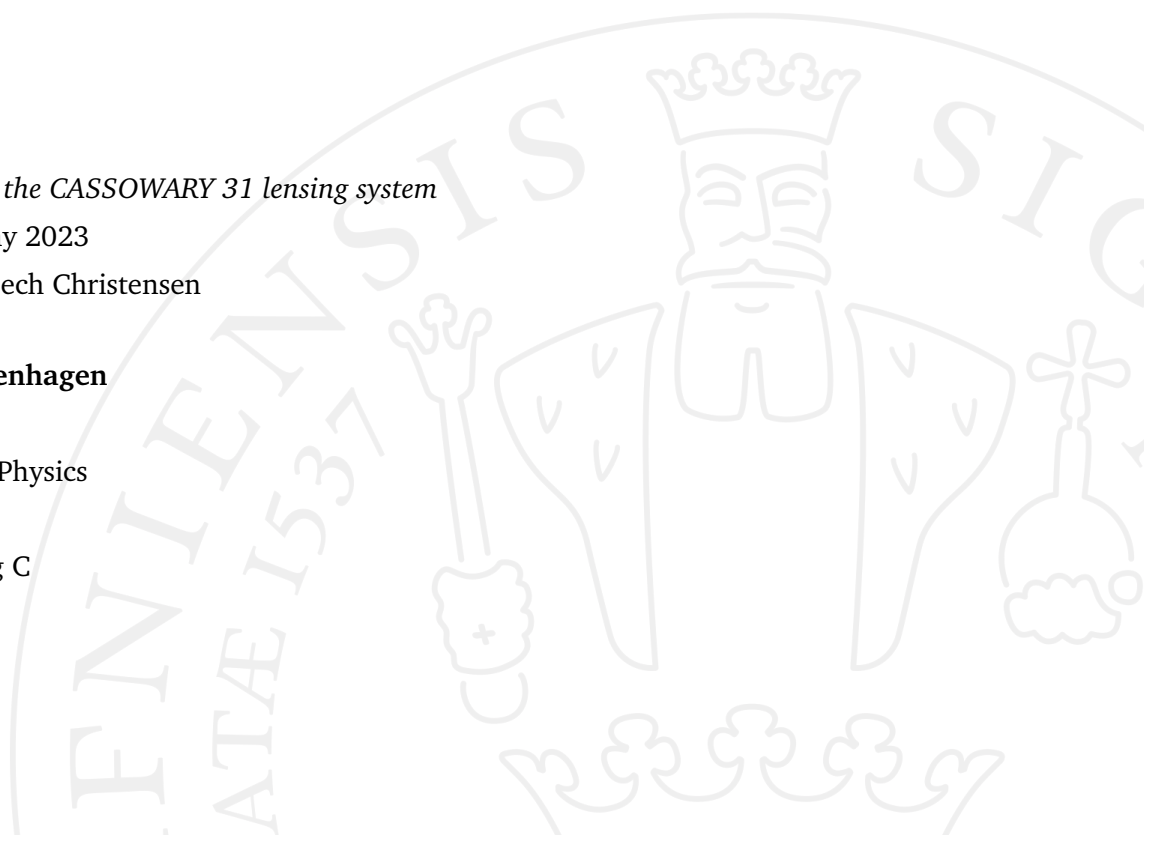
University of Copenhagen

Faculty of Sciences

Masters Degree in Physics

Bülowsvej 17

1870 Frederiksberg C



Acknowledgements

During the writing process of this paper, I got help from many people. First of all, I would like to thank my supervisor, Prof. Lise Christensen, for her careful guidance.

I would also like to thank Prof. Dawn K. Erb, Prof. Anne Jaskot, Dr. Raul Ortega Ochoa, and Dr. Guozhen Ma for their help in completing the research.

Finally, I would like to thank my family who have always supported me. Their support will always be my strongest backing.

Abstract

We analyzed the five objects in the CASSOWARY 31 lensing system based on the MUSW UV spectrum and studied the properties of the object with the highest signal-to-noise ratio through simulations, and found it to be a dwarf galaxy with low metallicity, and its spectrum is probably derived from the joint action of stellar population and shock in the galaxy. Firstly, we remeasured the redshifts of 4 of the lensed objects, paying particular attention to two objects with good signal-to-noise ratios: S0 and S3. We measured the column densities of some of these elements through their unsaturated absorption lines. Their absorption features show a clear blue shift, suggesting the presence of outflows. The outflow is further evidenced by the existence of resonant scattering Fe II* emission lines in S0 and its spatial extension in the corresponding narrow band. Next, we used various diagnostics to estimate the properties of S3. We finally got that the stellar mass of S3 is around $10^9 M_{\odot}$, the value of the metallicity of the stellar population is about $0.2 - 0.3 Z_{\odot}$, and the star formation rate is between $1.5 - 4.5 M_{\odot} \text{ yr}^{-1}$. The ionization parameter is about $\log(U) = -2.14$, and the value of $\log(\text{sSFR})$ is between -8 and -9 . According to these properties, we think S3 is a dwarf galaxy without a starburst phenomenon. Next, we used BPASS and CLOUDY to simulate the output spectrum of S3. We finally concluded that the pure photoionization model could not reproduce the spectrum of S3, and adding AGN to the model would lead to an excessively high He II intensity that does not match the observed situation. The stellar population + shock model can well reproduce the UV line ratios we observed in the spectrum. Despite questionable reliability, we think that the lower metallicity stellar population + shock model with shock contribution below 50% in incident radiation was the closest to the observation results of S3.

Keywords: high-redshift galaxies, UV spectra, metallicity, simulation

Contents

1	Introduction	1
2	Observations and data processing	9
2.1	VLT/MUSE spectroscopy	10
2.2	Spectral extraction	11
3	Spectral analysis	15
3.1	Detection of emission and absorption	15
3.2	S0	16
3.2.1	Redshift correction of S0	16
3.2.2	Emission and absorption lines of S0	17
3.2.3	Fe II* fine structure lines of S0	20
3.3	S2	23
3.3.1	Redshift correction of S2	23
3.3.2	Emission and absorption lines of S2	24
3.4	S3	25
3.4.1	Redshift correction of S3	25
3.4.2	Emission and absorption lines of S3	27
3.5	Foreground object blended with S3 spectrum	29
3.6	S4	30
3.6.1	Redshift correction of S4	31
3.6.2	Emission and absorption lines of S4	31
3.7	S5	32
4	Analysis of S3 properties	33
4.1	Spectral features of S3	33
4.1.1	Stellar winds features	33
4.1.2	Outflow features	35
4.1.3	Nebular emission lines	35
4.2	Estimates of the properties of S3	36
4.2.1	Estimation of metallicity	36

4.2.2	Star formation rate and stellar mass	38
4.2.3	BAGPIPES fitting	40
4.3	Simulation of stellar population	44
5	Simulation of S3	49
5.1	Model settings	49
5.1.1	Incident radiation fields	50
5.1.2	Geometry	50
5.1.3	Metallicity	50
5.2	Pure photoionization model of stellar population	51
5.2.1	General trend	51
5.2.2	Best fit model	54
5.3	Shocks	55
5.3.1	General trend	56
5.3.2	Diagnostics	61
5.3.3	Best fit model	64
5.4	AGNs	66
5.5	shock + AGN	68
6	Summary	71
7	Bibliography	73
A	Emission and absorption lines	79
A.1	S0	79
A.1.1	Emission	80
A.1.2	Absorption	81
A.2	S3	83
A.2.1	Emission	83
A.2.2	Absorption	84
A.3	Foreground object absorption	86

Introduction

In the past two decades, the universe at redshift $z > 1$ has been an essential topic in astronomy. Several studies have shown that this is a critical stage in the evolution of galaxies and that for most galaxies, their mass accumulates during this era. At the same time, both star formation and black hole accretion activity peaked. In related studies, the research and analysis of UV spectra of high-redshift galaxies play an important role. There have been many achievements in the research and analysis of the UV spectra of high-redshift galaxies. As far as the current consensus is concerned, the ultraviolet spectra of high-redshift galaxies are systematically bluer and harder than most local galaxies. They usually include many highly ionizing emission lines with relatively large equivalent widths, such as carbon (e.g., C III] 1906, 1909 Å; C IV 1548, 1550 Å), oxygen (O III] 1660, 1666 Å), and helium (He II 1640 Å). Rest frame UV spectra contain information about the galaxy's star formation activity, hot young star populations, and the physical, chemical, and dynamic state of the interstellar medium (ISM). These properties have been well studied in the local universe (Kinney *et al.* 1993; Heckman *et al.* 1998).

However, the study of UV spectroscopy also has its problems. First, ultraviolet photons are more challenging to detect than optical photons, often requiring space-based observatories. Furthermore, observations of the rest frame UV spectra of star-forming galaxies reveal complex and overlapping features, including stellar wind-related emissions (C IV 1550 Å, Si IV 1400 Å), fine-structure emission lines due to outflow, resonant transitions, and emission from transitions from non-stellar ionization sources (Mg II 2796 Å).

In the past decade, the rest frame UV spectra of a large number of high-redshift galaxies have been discovered through large deep optical spectroscopy surveys using ground-based 8-10 meter telescopes (Steidel *et al.* 2003; Shapley *et al.* 2003; Lilly *et al.* 2007; Cimatti *et al.* 2008). However, since they are usually too faint, it is not easy to obtain high signal-to-noise (S/N) observations, even with 8-10 m class telescopes. Before the launch of JWST, this difficulty was mainly

solved by constructing composite spectra of high redshift galaxies (Steidel *et al.* 2001; Shapley *et al.* 2003; Rigby *et al.* 2018) and analyzing certain objects magnified by gravitational lensing (Pettini, Ellison, *et al.* 2002; Pettini, Rix, *et al.* 2002; Quider *et al.* 2009; Vanzella *et al.* 2016). These studies generally think that these galaxies are generally very young ($\sim 10^8$ yr), metal-poor ($Z < 0.5Z_{\odot}$), low-mass galaxies with high specific SFR and strong outflow of ionized gas. These galaxies undergo little chemical evolution compared to local galaxies.

For galaxies with higher redshifts ($z > 6$), the consensus is that these low-mass galaxies contribute most of the star formation in the high-redshift universe and may be critical contributors to reionization (Wise *et al.* 2014; Stanway *et al.* 2016). However, because the research on such galaxies usually can only obtain the high S/N spectra of specific galaxies through the gravitational lensing effect before the launch of JWST, it is difficult to fully sample the diversity of high-redshift galaxy populations and strictly restrict their physical conditions and chemical composition. In particular, low-mass, low-metallicity sources have been poorly studied in detail, and their physical conditions, such as electron temperature, density, and gas-phase oxygen abundance, have been directly determined for only a few targets (Hainline *et al.* 2009; Bayliss *et al.* 2014; Lise *et al.* 2012). These reasons have led to many key problems in the study of galaxy formation and evolution that have become very difficult to solve.

An alternative approach is to look for relatively bright analogs of these galaxies in the lower-redshift universe. Erb *et al.* (2010) proposed that their properties can be studied by looking for similarly low-mass, low-metallicity, and bluer galaxies in the universe at the redshift of $z \sim 2$ or lower. They studied an unusually bright galaxy Q2343-BX418 at $z=2.3$. By using UV and optical line ratios combined with photoionization models, they found that the properties of this galaxy are significantly different from typical galaxies at $z \sim 2$ and local starburst galaxies. However, its properties are broadly similar to those of young, low-mass galaxies found at much higher redshift, so its detailed spectroscopic properties may reveal the likely physical conditions of these higher redshift objects. Olivier *et al.* (2022) studied two local galaxies with highly ionized nebular lines, revealing the hard ionizing radiation field that may originate from the starburst in the low metallicity environment. They suggest that the properties of these galaxies are similar to what we would

expect to find in the distant universe. Tang *et al.* (2021) observed the rest frame UV emission lines in $1.3 < z < 3.7$ galaxies with high specific star formation rate (sSFR) and found that only poor metal emitters with intense $H\beta + [O\ III] 5007\ \text{\AA}$ EWs $> 1500\ \text{\AA}$ had C III] emission strengths are comparable to that emission lines observed at $z > 6$.

Considering that the overall star formation of galaxies and the outflow and inflow of gas will affect the metallicity of galaxies, the study of element abundance in galaxies is very important for us to understand the evolution process of galaxies and the history of star formation. However, the abundance determination of high-redshift galaxies faces considerable obstacles. For most star-forming regions, oxygen abundance is estimated using empirical methods based on the relative strength of strong, readily observable optical lines. Although abundances derived in this way are considered to be subject to considerable uncertainty, they are still thought to allow a rough general estimate of the metallicity of galaxies. The most widely used empirical abundance calibrators are the $R23$ (Pagel *et al.* 1979) and $S23$ (Vilchez and Esteban 1996) parameter methods. The $R23$ parameter is defined as the sum of fluxes of [O II] 3727Å and [O III] 4959,5007Å lines relative to $H\beta$ flux ($R23 = \frac{[OII]_{3727\text{\AA}} + [OIII]_{4959,5007\text{\AA}}}{H\beta}$), but this method relies heavily on the quality of dereddening and has a larger dispersion than the observed results. The $S23$ parameter is defined as the sum of fluxes of [S II] 6717,6731 Å and [S III] 9069,9532 Å relative to $H\beta$ flux ($S23 = \frac{[SII]_{6717,6731\text{\AA}} + [SIII]_{9069,9532\text{\AA}}}{H\beta}$). Compared to the $R23$ parameter, it (and the similar parameter $S234 = \frac{[SII] + [SIII] + [SIV]}{H\beta}$) is more sensitive to the ionization parameter. However, the detection of sulfur lines in the near-infrared is limited to galaxies with redshifts less than 0.1 and cannot be applied to samples of high-redshift universes.

Storchi-Bergmann *et al.* (1994) also proposed $N2 = [N\ II] 6584\ \text{\AA}/H\alpha$ as an abundance estimator. Raimann *et al.* (2000) improved their calibration of the $N2$ vs. O/H relationship, and Denicoló *et al.* (2002) further developed this diagnostic. However although the [N II] and $H\alpha$ lines can be separated even in moderate resolution spectra, and the $N2$ line ratio does not depend on reddening correction or flux calibration, its usable redshift range can only reach the upper limit of $z=2.5$.

On the other hand, an obvious difficulty in applying optical line diagnostics to high-redshift galaxies is that the line flux decreases dramatically, given the much larger distance involved. The problem is compounded by the redshift of spectral lines into the near-infrared and even far-infrared wavelength region, where the sky background is orders of magnitude higher than optical. For ground-based telescopes, at a given redshift, only a portion of the strong line will fall within the atmospheric window and thus be observable from the ground. Even at particularly favorable redshifts (e.g., $z=2.3$), where most of the major optical emission lines are shifted to the center of the corresponding band, it is impossible to record all of these lines in a single exposure. However, observations made with different spectrometer settings can easily introduce additional errors in the relative flux calibration. For all these reasons, the accuracy of measuring the emission line ratio in high-redshift objects is severely limited.

In response to this situation, Byler *et al.* (2020) developed a series of diagnostics based on UV emission lines. Using a sample of galaxies for which both rest-frame UV and optical spectral data were observed, they compared the UV-derived metallicity with standard optically-derived metallicity. They found that the He2–O3C3 diagnostic ($\text{He II } 1640 \text{ \AA} / \text{C III] } 1906, 1909 \text{ \AA}$ vs. $[\text{O III] } 1666 \text{ \AA} / \text{C III] } 1906, 1909 \text{ \AA}$) is a reliable metal abundance tracer, especially at low metal abundance ($12 + \log (\text{O}/\text{H}) < 8$), where stellar contributions are minimal. The Si3–O3C3 diagnostic ($[\text{Si III] } 1883 \text{ \AA} / \text{C III] } 1906 \text{ \AA}$ vs. $[\text{O III] } 1666 \text{ \AA} / \text{C III] } 1906, 1909 \text{ \AA}$) is also a reliable metal abundance tracer, albeit with a larger scatter (0.2– 0.3 dex), which they think is driven by changes in the gas phase abundance. While the C4–O3C3 diagnostic ($\text{C IV } 1548, 1450 \text{ \AA} / [\text{O III] } 1666 \text{ \AA}$ vs. $[\text{O III] } 1666 \text{ \AA} / \text{C III] } 1906, 1909 \text{ \AA}$) correlates poorly with the metallicity inferred by optical methods. Byler *et al.* (2020) concluded that although the UV diagnostic method showed theoretical promise, in practice UV-derived abundances showed considerable scatter and did not always recover optical abundances. Whereas the work of Pérez-Montero and Amorín (2017) used a semi-empirical approach based on a photoionization model to derive oxygen (O/H) and carbon abundances (C/O) from the rest frame UV emission lines ($\text{C III] } 1906, 1909 \text{ \AA}$, $\text{C IV } 1558, 1550 \text{ \AA}$, $\text{O III] } 1660, 1666 \text{ \AA}$), resulting in is in perfect agreement with direct estimates based on electron temperatures in star-forming regions. They think this provides a potentially powerful tool to extrapolate the metallicity limit of galaxies to very high redshift. With the JWST put into use and the construction of 30-40m ground-based telescopes in

the future, we think that more usable samples may bring discoveries to the research of UV diagnostic methods.

Some other work has focused on using spectral information to determine the energy source driving ionizing emissions. The seminal paper by Baldwin *et al.* (1981) was the first to classify emitters by means of a diagnostic map (hereafter referred to as a BPT map) containing ratios of optical emission lines. The BPT diagram shows that AGN exhibits a higher line ratio than Star Formation (e.g., $[\text{O III}] 5007 \text{ \AA}/\text{H}\beta$ and $[\text{N II}] 6584 \text{ \AA}/\text{H}\alpha$).

This is thought to be due to the harder ionization spectral energy distribution (SED) of radiation emitted during gas accretion into a supermassive black hole (SMBH), higher ionization, and greater metallicity in the active galactic nuclei host. However, higher line ratios can also be obtained using shocks-dominant models with relatively high shock velocities. Shocks have many different origins, such as starburst galaxies, AGNs, galaxy mergers, and accretion disks. High-speed shocks generate a powerful ultraviolet radiation field that ionizes the gas and emits a spectrum of highly excited emission lines. Therefore, the optical line ratio diagnostic cannot provide a conclusive shock diagnostic. Therefore, in order to reproduce the model established by observing the line ratio, we should consider compound ionization sources, including stellar population, shocks, AGN, etc., which are more reliable than the results obtained by pure photoionization or pure shock models. The study of Allen *et al.* (1998) gave a distinction between the pure photoionization model and the shocks model of emitters based on the UV emission line ratio. They included pure precursors, pure shocks, and a mixture of precursors and shocks in their work. Jaskot and Ravindranath (2016) explored the diagnostic method to determine the contribution ratio of shocks to incident radiation fields. The classification of emitters has been used in many works involving simulation. Jaskot and Ravindranath (2016) introduced the shocks component in the photoionization model to reproduce the observed emission line ratio, Olivier *et al.* (2022) tried to add a blackbody of 80,000 K to pure stellar population photoionization in an attempt to reproduce the observed extremely high ionization emission lines.

In this project, we focus on a strong gravitational lensing system CASSOWARY 31 (CSWA 31). According to general relativity, gravitational lensing is the bending of light from a background light source as it passes through a gravita-

tional field. If the source, massive lens object, and observer lie in a straight line, the original light source will appear as a ring around the massive lens object (provided the lens has circular symmetry). If there is any misalignment, the observer will see an arc segment. Since the gravitational lensing does not change the surface brightness of the background object, and the magnification is achromatic which means that the luminosity at all wavelengths are magnified by the same factor, we can easily restore the luminosity of the objects before they are magnified by the lensing effect, so the gravitational lensing has become an important basis for astronomers to study distant and dim objects.

CSWA 31 is a unique lens system, and the brightest group of galaxies (BGG) at the center is a supermassive elliptical galaxy located at $z = 0.683$. It is surrounded by group members and several lensed arcs of 5 different lensed objects. Wang *et al.* (2022) modeled the inner dynamics and dark matter distribution of this system, but the spectra of its lensed objects have not been studied in detail. Here, we study the muse UV spectra of these lensed objects in detail, with a particular focus on S0 and S3 with good signal-to-noise ratios and the presence of a large number of emission and absorption features. We analyzed and fitted these emission and absorption profiles, measured their flux and equivalent widths (EWs), discussed the existence of outflow, and re-determined their redshifts based on the emission lines. We use BAGPIPES to fit the continuum and get their star formation rate (SFR), stellar mass, metallicity, ionization parameter, and other properties, then found that the fitting results are very close to the results given by a series of methods such as emission line EWs–metallicity relation and SFR–Stellar mass relation. For S3 with obvious stellar wind features, we used BPASS to fit its stellar wind emission features and found the stellar population spectrum closest to the observation. Then we used the stellar population as the incident radiation, used the radiative transfer model created by CLOUDY to simulate the output spectrum under different conditions, and added AGNs and shocks to it to explore the energy source that might drive the S3 emission.

This thesis is organized as follows. In Sect.2, we introduced observation and the extraction of observed spectra. In Sect.3, we remeasured the redshift, analyzed the properties of emission lines and absorption lines in the spectra, and fitted and analyzed their line profiles. We discuss the possible outflows in S0 and S3. In Sect.4, we estimated the properties of S3 (metallicity, SFR, stellar mass, etc.) based on the spectral features. We validated our estimated

results using BAGPIPES fitting. We used the BPASS simulation method to find the best-fit stellar population of S3. In Sect.5, we used the spectrum of the best fit stellar population as the incident radiation field, then used the radiative transfer model created by CLOUDY to simulate the observed spectrum of S3. In order to reproduce the line ratio in the observed spectrum, we added different proportions of AGN contribution and shock contribution to the incident radiation field, then set different element abundances to find the best simulation results. In Sect.6, we summarize our results and discuss the potential further studies. Throughout this work, we assume $H_0 = 70 \text{ km s}^{-1} \text{ Mpc}^{-1}$, $\Omega_m = 0.3$ and $\Omega_\Lambda = 0.7$.

Observations and data processing

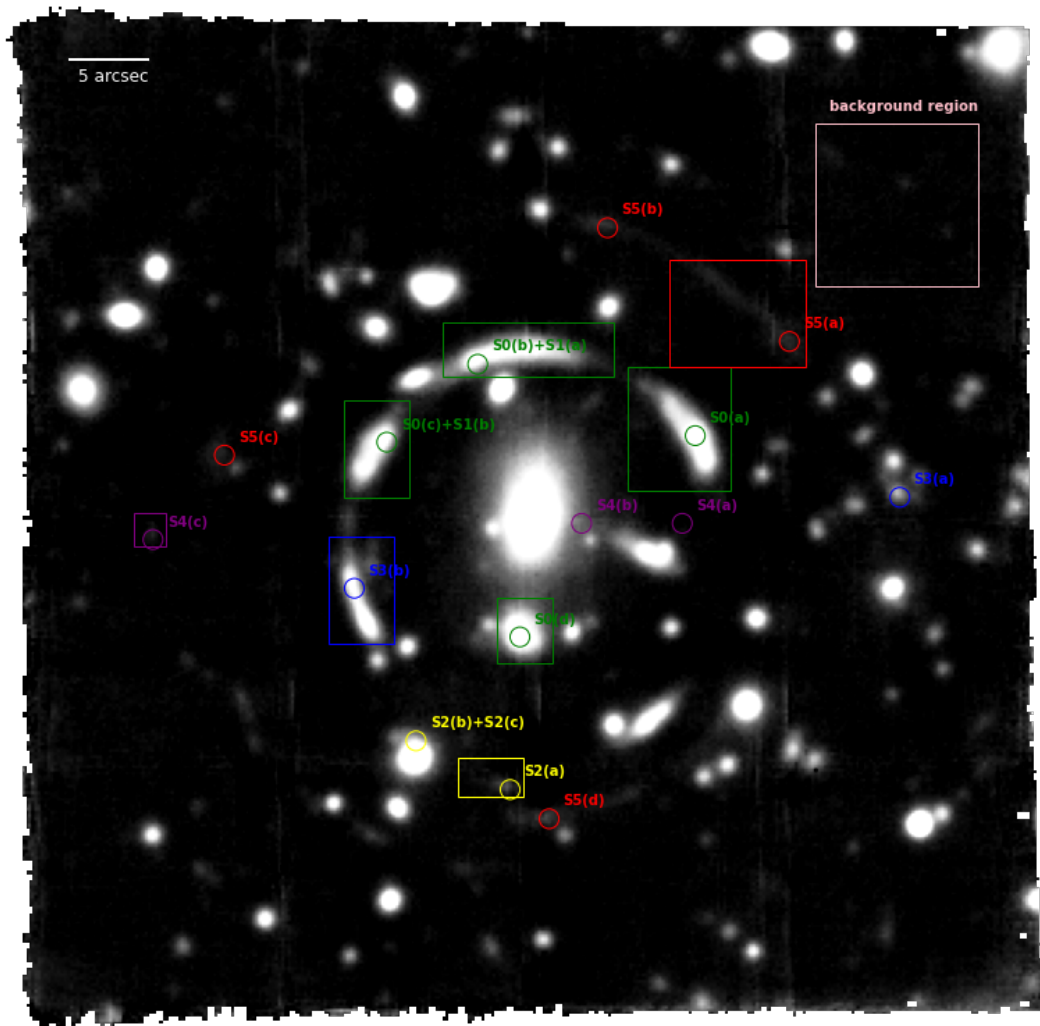


Figure 2.1.: The stacked image of the MUSE datacube of CSWA 31. We marked the positions of the different images with different colors, and the regions used to extract the spectra were marked with rectangles. The image sets S0 and S1 are bright knots from the same spiral galaxy.

The CSWA31 lens system was discovered in SDSS imaging as part of the Cambridge And Sloan Survey Of Wide ARcs in the skY (CASSOWARY, Belokurov *et al.* 2009), and several previous works modeled and analyzed this system (Brewer *et al.* 2011; Stark *et al.* 2013; Grillo *et al.* 2013; Wang *et al.* 2022). The main lens galaxy of CSWA 31 is an early-type galaxy located at $z = 0.683$, with a high stellar mass of about $3 \times 10^{12} M_{\odot}$, which be referred to as the brightest group galaxy (BGG). Surrounding the central BGG are giant lensed arcs of 5 main background objects, formed by a face-on spiral at $z = 1.487$ (Wang *et al.* 2022).

We show the stacked image of the MUSE datacube of CSWA 31 in Figure 2.1 and mark the positions of the images of the background galaxies. We also mark with rectangles the regions we selected when extracting the spectra of objects and the sky background from the MUSE datacube. In Table 2.1, we show the positions and redshifts of various parts of the CSWA31 system used by Wang *et al.* (2022) in their modeling work. In Table 2.2, we show the magnification factors of the two brightest objects S0 and S3 in their modeling work (This table is obtained from personal communication by Wang).

2.1 VLT/MUSE spectroscopy

This work uses MUSE data from program 0104.A-0830(A) (PI: Raoul Canameras). Observations were carried out in December 2019 and January 2020, with seeing $\leq 1''$ and airmass < 1.6 , with the MUSE wide-field mode corresponding to $1' \times 1'$ field-of-view and $0.2'' \text{ pix}^{-1}$ spatial sampling. The observations were divided into five individual OBs, applying a dithering pattern and 90° rotations between each OB, and obtained a total exposure time of 5 hours. Wang *et al.* (2022) used the MUSE pipeline to perform data reduction, including correction of raw exposures for the bias, flat fields, and illumination frames, wavelength correction, optimization of sky subtraction, etc.

Table 2.1.: Position and redshift of the BGG and multiple images used in the Wang *et al.* (2022)'s work

ID	RA	dec	z
BGG	9:21:25.738	18:10:17.70	0.6828
S0(a)	9:21:25.040	18:10:12.27	1.4869
S0(b)	9:21:25.858	18:10:07.24	1.4869
S0(c)	9:21:26.439	18:10:13.60	1.4869
S0(d)	9:21:25.781	18:10:24.64	1.4869
S1(a)	9:21:25.987	18:10:07.84	1.4869
S1(b)	9:21:26.376	18:10:12.58	1.4869
S2(a)	9:21:25.851	18:10:34.05	1.4874
S2(b)	9:21:26.252	18:10:31.13	1.4874
S2(c)	9:21:26.323	18:10:31.04	1.4874
S3(a)	9:21:24.159	18:10:16.03	2.763
S3(b)	9:21:26.517	18:10:21.73	2.763
S4(a)	9:21:25.105	18:10:17.76	3.4280
S4(b)	9:21:25.531	18:10:17.62	3.4280
S4(c)	9:21:27.395	18:10:18.65	3.4280
S5(a)	9:21:24.634	18:10:06.47	4.205
S5(b)	9:21:25.418	18:09:59.46	4.205
S5(c)	9:21:27.085	18:10:13.39	4.205
S5(d)	9:21:25.670	18:10:35.81	4.205

This redshift is inferred from emission lines, absorption lines or continuum breaks in the spatially averaged spectrum and spectra extracted along two perpendicular directions. They also fitted templates to sources with bright stellar continuum to help infer their redshift.

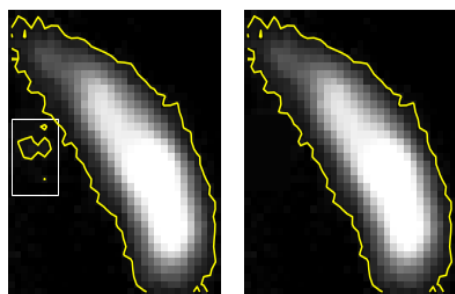
Table 2.2.: The magnification factor of S0 and S3 in different models given by Wang *et al.* (2022)

Model	S0(a)	S0(b)	S0(c)	S0(d)	S3(a)	S3(b)
Img-MP(L)	6.79	-5.00	4.74	-5.40	2.80	-103.21
Esr2-MP _{test} (L)	9.35	-6.87	7.21	-6.55	3.37	-86.87
Img-MP(L/D)	6.81	-6.80	4.82	-6.65	2.66	-119.23

2.2 Spectral extraction

In this section, we describe our procedure for extracting 1D spectra from the MUSE datacube. For each object, we select the brightest image to extract the spectrum (for S0 and S1, we extract the spectra of all their images due

to the need to confirm the fine structure emission lines in the subsequent chapters). For each target image, we first select the pixels within the bounding box region including it and then plot their 3σ contours relative to the sky background. The value of σ is determined by the 3-sigma-clip average value of the pixels in the sky area marked by the pink rectangle in Figure 2.1. For some sources, there are still some pixels above the threshold that are not related to the main image in the selected area (S0(a), S0(b)+S1(a), S2(a), S3(b), S5(a)). For these pixels, we mask them out using the average value of the sky background in the region. Then we extract the 1D spectra of these pixels above the threshold and use their sum as the object's spectrum. In Figures 2.2-2.9, we show the regions we used to extract the spectra. We plot their 3σ contours of them and show how we mask out the extra pixels.



(a) origin figure (b) masked image

Figure 2.2.: S0(a)

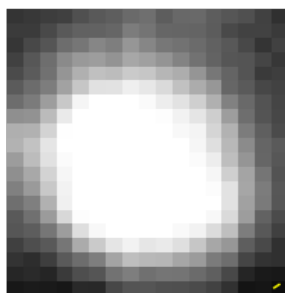
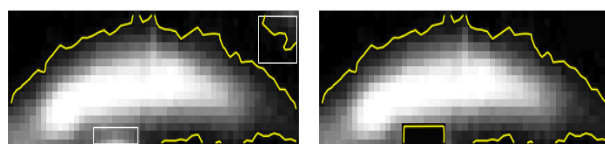


Figure 2.3.: S0(d)



(a) unprocessed image (b) masked image

Figure 2.4.: S0(b)+S1(a)

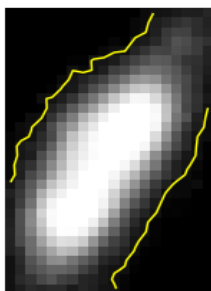
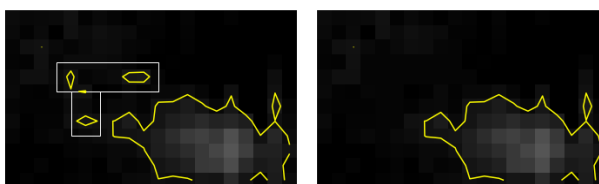


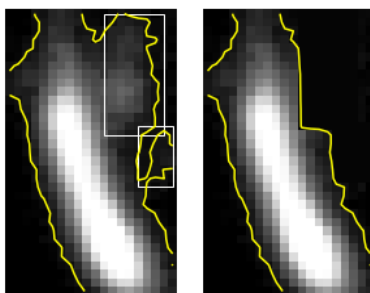
Figure 2.5.: S0(d)+S1(b)



(a) unprocessed image

(b) masked image

Figure 2.6.: S2(a)



(a) unprocessed image

(b) masked image

Figure 2.7.: S3(b)

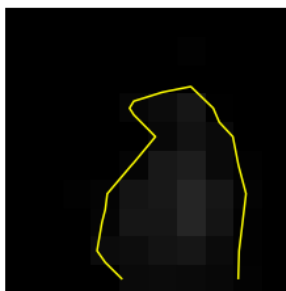
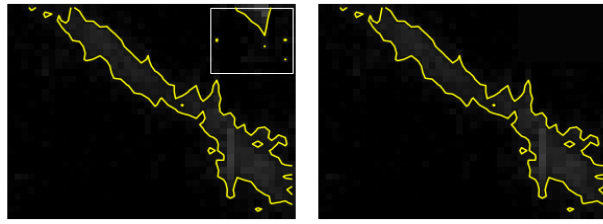


Figure 2.8.: S4(c)



(a) unprocessed image

(b) masked image

Figure 2.9.: S5(a)

Spectral analysis

3.1 Detection of emission and absorption

After we have extracted the spectrum from the 3D datacube, we first need to find out the emission and absorption features in the spectrum. For the emission line, the excess signal is considered statistically significant if it exceeds three times the statistical noise level of the total continuum flux contained in the $n_\lambda = \delta\lambda/\Delta\lambda (\approx 2 - 3)$ pixels spanned by the resolution element, where $\delta\lambda$ is the length of the resolution element which defines as the FWHM of the Line Spread Function(LSF), and $\Delta\lambda$ is defined as the wavelength step of a single pixel in the wavelength axis. The method can be written as follows:

$$S_l > 3\sqrt{n_\lambda}\sigma_S \quad (3.1)$$

S_l is the line flux of the emission, n_λ is the number of pixels taken into account, and σ_S is the uncertainty of the line flux.

For the absorption line, we have a similar method:

$$S_W > 3\sqrt{n_\lambda}\sigma_S \quad (3.2)$$

S_W is the depth of the absorption line. Since the absorption line of equivalent width W_λ removes a total of $\frac{W_\lambda S_c}{\Delta\lambda}$ photons from the raw continuum spectrum, when smeared over the resolution element $\delta\lambda$, it can be written as:

$$S_W \approx \frac{W_\lambda S_c}{\delta\lambda} \quad (3.3)$$

Following this approach, we iterate over the spectra of all five objects and list their emission and absorption features. All spectral analyses in this chapter have not been corrected for magnification.

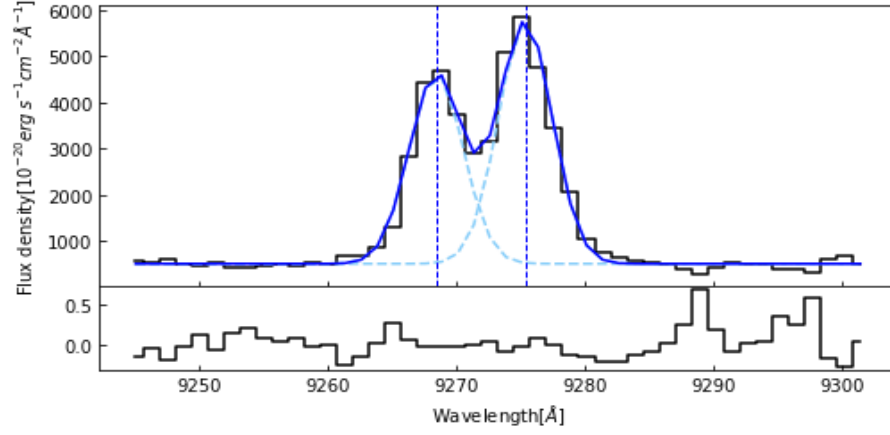


Figure 3.2.: [O II] 3727, 3729 doublet of S0(a)

Table 3.1.: S0(a) [O II] doublet fitting

Line	Amplitude ($10^{-20} \text{ erg s}^{-1} \text{ cm}^{-2} \text{ \AA}^{-1}$)	Central wavelength (\AA)	FWHM (\AA)
[O II] 3727.0920	4114.8304	9268.4469	4.7683
[O II] 3729.8750	5242.2710	9275.3676	4.7683

Using the redshift formula, we end up with a redshift $z_{S0} = 1.4868$ for S0.

3.2.2 Emission and absorption lines of S0

After determining the redshift, we analyze the observed absorption and emission lines in the rest frame. For absorption lines, we measured their rest-frame equivalent widths (EW_{rest}) and calculated their flux-weighted central velocities and corresponding velocity extensions. The calculation formula of flux-weighted central velocity is:

$$v_c = \frac{\sum f_\lambda v_\lambda}{\sum f_\lambda} \quad (3.5)$$

where v_λ is the shifted velocity relative to the rest frame wavelength at wavelength λ . The velocity extensions correspond to the ranges used to calculate the equivalent width. We list the information of the absorption lines in the S0(a) spectrum in Table 3.2 (Profiles for absorption lines and emission lines not given in the main text are shown in the appendix.). In order to determine

the uncertainty of EW_{rest} , we use a bootstrap Monte Carlo simulation in which the 1σ uncertainty was used to perturb the average profile and generate 1000 artificial spectra, and then we take the standard deviation of their equivalent widths as the uncertainty.

Table 3.2.: Absorption lines in S0

Ion	λ_{vac} (Å)	f	EW_{rest} (Å)	v_c ($km\ s^{-1}$)	Δv ($km\ s^{-1}$)
Fe II	2260.7805	0.00244	1.077 ± 0.056	-139	-438:229
Fe II	2344.2140	0.114	2.987 ± 0.054	-196	-612:224
Fe II	2374.4612	0.0313	2.171 ± 0.071	-132	-551:211
Fe II	2382.7650	0.32	2.810 ± 0.058	-220	-518:115
Fe II	2586.6500	0.0692	2.593 ± 0.039	-155	-566:192
Fe II	2600.1729	0.239	3.142 ± 0.045	-184	-499:139
Mg II	2796.3520	0.629	3.659 ± 0.071	-268	-636:118
Mg II	2803.5310	0.308	3.415 ± 0.036	-246	-596:157
Mg I	2852.9642	1.80	1.084 ± 0.034	-183	-550:137

f is the oscillator strength of the transition.

From Table 3.2, we can see that all the absorption lines observed from S0 are Fe lines and Mg lines. Due to the embarrassing combination of the redshift of S0 and the coverage of the MUSE spectrum, we can only get the spectrum with rest frame wavelengths from 1910 Å to 3760 Å, which prevents a large number of important ultraviolet emission and absorption lines (e.g., He II 1640, O III] 1660, 1666, Si IV 1393.7550, 1402.7700) from being observed, makes it difficult for us to further study S0 in detailed.

From the absorption line of S0, we can see that the value of the flux-weighted velocity center of the absorption line is relatively close, fluctuating between $-132.219\ km\ s^{-1}$ to $-268.356\ km\ s^{-1}$. At the same time, they have very similar velocity extensions. This may indicate that these absorption lines originate in the same part of the galaxy that has a velocity towards us of around $200\ km\ s^{-1}$ along the line of sight, or at least the parts that make these absorption lines have the same velocity.

Most of the absorption lines observed in S0 are saturated, while the unsaturated absorption lines can be used to infer the element abundance of the

medium. If we assume that the medium is optically thin, we can use the linear part of the curve of growth proposed by Spitzer (1978) to obtain the relationship between the column density and the equivalent width of the element:

$$N = 1.13 \times 10^{20} \left(\frac{W_\lambda}{\lambda^2 f} \right) (cm^{-2}) \quad (3.6)$$

The saturated absorption line can only give the lower limit of column density. Based on the unsaturated absorption lines observed in S0, we show the measured results in Table 3.3.

Table 3.3.: Column densities derived from the unsaturated absorption lines in S0

Transition	f	EW_{rest} (Å)	Column density (cm^{-2})
Mg I 2852.9642	1.80	1.084 ± 0.034	$8.361 \pm 0.262 \times 10^{12}$
Fe II 2260.7805	0.00244	1.077 ± 0.056	$9.759 \pm 0.507 \times 10^{15}$
Fe II 2344.2140	0.114	2.987 ± 0.054	$5.388 \pm 0.097 \times 10^{14}$

It is worth noting here that, in theory, Fe II 2260 and Fe II 2344 should derive the same column density, but their actual results differ by an order of magnitude. Since we did not find any absorption or emission lines from other objects in the spectrum of S0, we think it is less likely to be caused by blending with lines from other objects. We think that the reason for this may be that our spectrum contains both S0 and S1 components, as we have mentioned in the previous section, which are two different knots of the same spiral galaxy. Therefore, the absorption lines we observe are actually the result of the joint action of two different knots. In fact, there are subtle structures similar to double peaks in most of the absorption lines of S0(a) we observed. However, due to the limited spectral resolution of MUSE data, we cannot use the double Gaussian model fitting method to separate them. Therefore, we think that the absorption components from different knots are the main reason for the inaccurate estimation of the column density of S0(a). In the subsequent estimation of the column density of S3, we did not see this difference and found that the column densities obtained for all saturated absorption lines were lower than those obtained for the corresponding unsaturated absorption lines. This result may mean that this method is credible for S3, or we can also speculate that the absorption lines observed in S3 may come from a continuous bulk medium.

In Table 3.4, we show the emission lines observed in the spectrum of S0(a). We calculated their fluxes, rest-frame equivalent widths, flux-weighted velocity centers, and FWHMs of their Gaussian profiles in the velocity spectrum.

Table 3.4.: Emission lines in S0

Ion	λ_{vac} (Å)	Flux ($10^{-20} \text{ erg s}^{-1} \text{ cm}^{-2}$)	EW_{rest} (Å)	v_c (km s^{-1})	Δv_{FWHM} (km s^{-1})
[O II]	3727.0920, 3729.8750	40914.046 ± 326.365	76.189 ± 1.097	-	124
Fe I	2523.6080	1146.373 ± 178.891	1.828 ± 0.053	33	210
Fe II*	2612.6542	966.156 ± 258.136	1.390 ± 0.036	-35	189
Fe II*	2626.4511	1371.62 ± 245.229	2.052 ± 0.039	-47	243

Since the Oxygen II doublets are mixed with each other, we cannot determine the v_c of them.

Between these emission lines, the bright [O II] 3727, 3729 are very common in planetary nebulae and emission nebulae. The fine-structured emission lines of Fe II* provides evidence for the existence of outflow in S0 (Kornei *et al.* 2013).

3.2.3 Fe II* fine structure lines of S0

Fe II* is not very common for most UV spectra of high-redshift galaxies. We examined all four images of S0+S1 and confirmed the presence of Fe II*. We checked the IUE atlas of star-forming galaxies compiled by Kinney *et al.* (1993b) and found no Fe II* fine structure lines. Rubin *et al.* (2010) studied the fine-structure Fe II* emission at $z \approx 0.7$ in starburst galaxies and found this emission within 30 km s^{-1} of the systemic velocity. Coil *et al.* (2011) studied Fe II* emission lines at $0.2 < z < 0.8$ in a sample of 11 post-starburst and active galactic nucleus (AGN) primary galaxies, Erb *et al.* (2012) studied the fine-structure Fe II* emission from 96 star-forming galaxies at $1 < z < 2$, Kornei *et al.* (2013) reported 212 star-forming galaxies at $z \approx 1$ selected from the DEEP2 survey, they all got the same result that the velocity centers of Fe II* tend to be distributed around 0 km s^{-1} , or in other words, keep consistent with the system velocity. These conclusions match perfectly with the results we showed in Table 3.4.

Regarding the origin of Fe II* emission, Prochaska *et al.* (2011) showed that the resulting emission profile in the presence of gas flow can still be centered on the system velocity. Therefore, the absence of a net kinematic shift does not necessarily imply that the associated gas is at rest relative to the galaxy's stars. Rubin *et al.* (2010) found that the profile of the Fe II* emission line is significantly different from both absorption lines tracing galactic winds and nebular lines associated with H II regions, also suggesting that the fine structure emission lines may have different origins from the H II region and the galactic wind. In fact, we also found that in the spectrum of S0, the Fe II* fine structure emission profile is significantly different from the average profile of the absorption line (shown in Figure 3.3), but very similar to the Fe I emission line, which may imply that they share the same origin. Erb *et al.* (2012) also found Fe II* fine structure lines and Fe II emission sharing similar profiles in their samples. Kornei *et al.* (2013) concludes that based on their samples, the velocity centroids of Fe II* are consistent with the system velocity, suggesting that these measurements are consistent with Fe II ions tracing the gas flow or stationary H II regions. Erb *et al.* (2012) used the photoionization model to simulate the observed results and found that they could not reproduce the observed [O II]/Fe II* ratio in their $1 < z < 2$ star-forming galaxy samples. Therefore, they think that these fine structure lines come from resonant scattering in the outflow. Rubin *et al.* (2010) also think that photon scattering in a large-scale galactic outflow is the most likely mechanism for generating fine-structured emission lines.

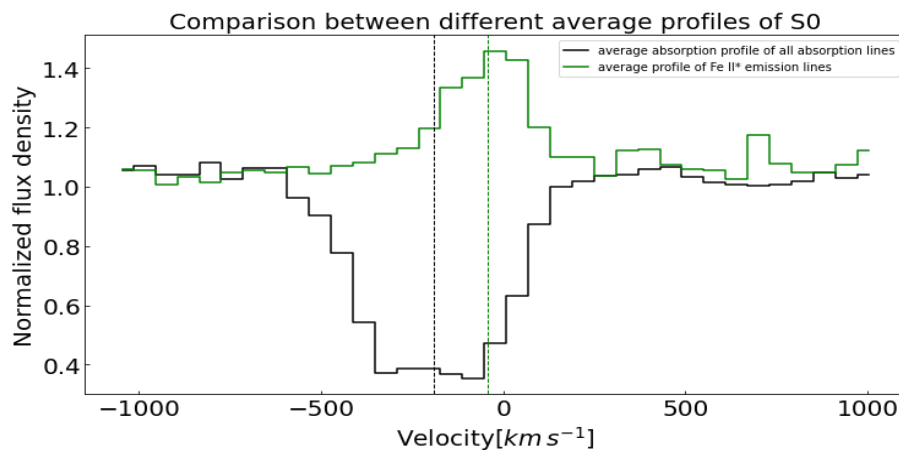


Figure 3.3.: The average profile of all absorption lines compared to the average profile of Fe II* fine structure emission lines. It can be seen that the average absorption profile has a non-obvious double-peak structure, which may imply different knots in the same galaxy.

Kornei *et al.* (2013) draw two important conclusions: First, Fe II* emitters show stronger Fe II resonance absorption lines and weaker Mg II resonance absorption lines compared to Fe II* non-emitters, and the weaker Mg II absorption seen in the Fe II* emitter is mainly caused by Mg II emission filling. Second, Fe II* emitters show more blueshifted Mg II resonance absorption lines than Fe II* non-emitters. However, the conclusion of Erb *et al.* (2012) is the opposite. They think that with the increase of Fe II absorption, the Fe II* emission shows a decreasing trend. Their explanation is that the system with stronger Fe II absorption may be dusty, thus showing only weak Fe II* emission. Furthermore, Erb *et al.* (2012) also argue that the ratio of the equivalent widths of emission and absorption we observe is related to the inclination of the galaxy because an anisotropic (i.e., biconical) outflow will give different observation results depending on the viewing angle: A biconical wind viewed from the side will show more emission, but a face-on view will give more absorption. In addition, Kornei *et al.* (2013) think that systems at higher redshifts with lower dust levels, lower star formation rates, and larger [O II] equivalent widths show stronger Fe II* emission.

For our data, we do observe blue-shifted Mg II and Fe II absorption lines in the spectrum, but since this is only an isolated case, we have no way to further verify the above discussion.

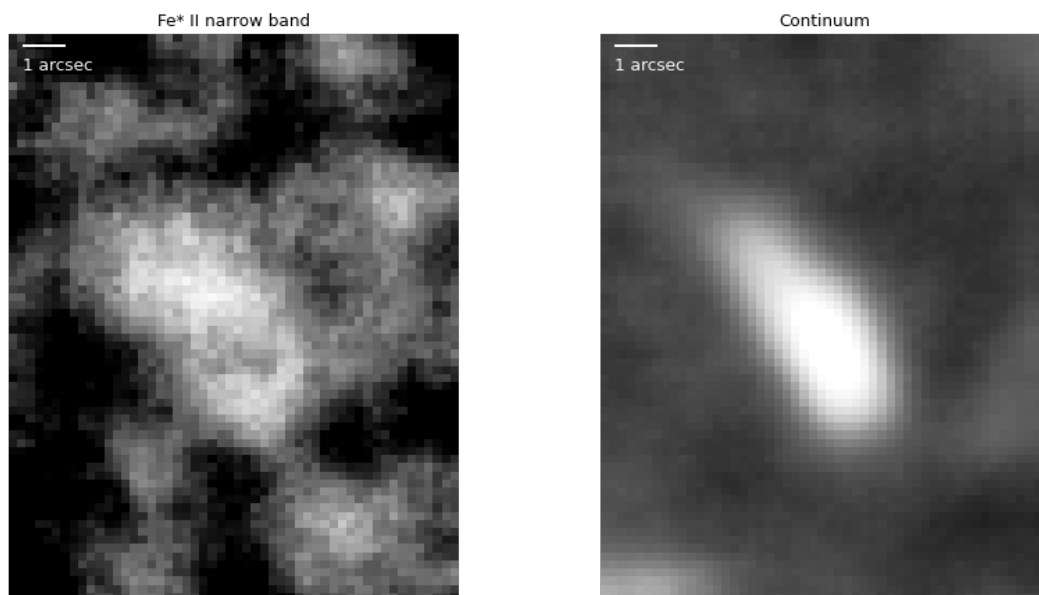


Figure 3.4.: Comparison of Fe II* narrow band image and continuum band image of S0(a).

In Figure 3.4, we compared the Fe II* narrow-band image with the continuum image to show the spatially extended structure of S3 in the Fe II* narrow-band image and then confirmed the existence of outflow.

We also quantitatively measure the difference in FWHM of S0(a) between the narrow-band image and the continuum-band image. We list the results in Table 3.5. Obviously, the narrow band image has a larger FWHM, whether measured along the x-direction or the y-direction.

Table 3.5.: FWHM of S0(a) in different band

axis	narrow band	continuum band
x-axis FWHM(arcsec)	2.842	1.995
y-axis FWHM(arcsec)	6.063	4.754

3.3 S2

In Figure 3.5, we show the continuum spectrum of S2(a). Unfortunately, since S2 is very dim, we get a very noisy spectrum, the [O II] 3727, 3729 doublet is the only spectral feature we can identify.

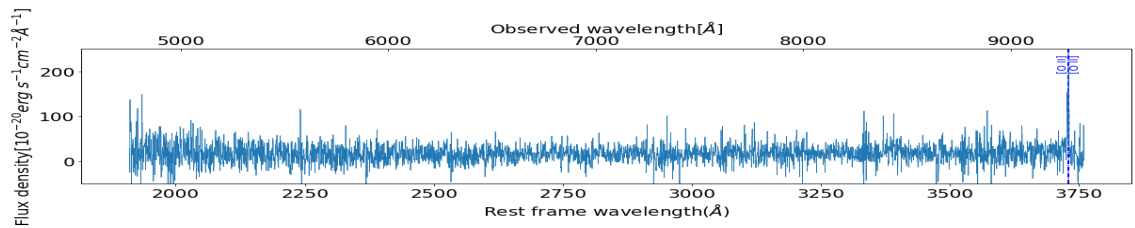


Figure 3.5.: S2(a) continuum spectrum

3.3.1 Redshift correction of S2

We use the [O II] 3727, 3729 doublet to re-measure the redshift of S2. As we did in S0, we use a double Gaussian model to fit its profile, and then in Figure 3.6 and Table 3.6.

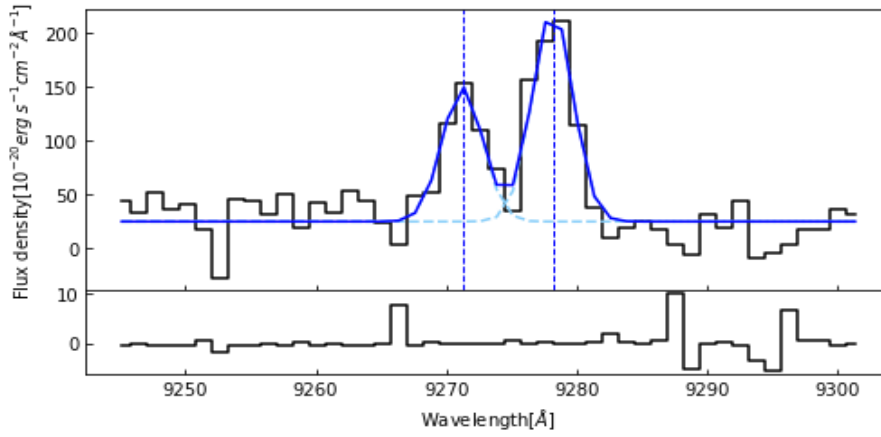


Figure 3.6.: [O II] 3727,3729 doublet of S2(a)

Table 3.6.: S2(a) [O II] doublet fitting

Line	Amplitude ($10^{-20} \text{erg s}^{-1} \text{cm}^{-2} \text{Å}^{-1}$)	Central wavelength (Å)	FWHM (Å)
[O II] 3727.0920	125.2637	9271.2470	3.4318
[O II] 3729.8750	198.0219	9278.1697	3.4318

Using the redshift formula, we end up with a redshift $z_{S2} = 1.4875$ for S2.

3.3.2 Emission and absorption lines of S2

We show the properties of the oxygen doublet emission in the rest frame in Table 3.7 of this section.

Table 3.7.: Emission lines in S2

Ion	λ_{vac} (Å)	Flux ($10^{-20} \text{erg s}^{-1} \text{cm}^{-2}$)	EW_{rest} (Å)	v_c (km s^{-1})	Δv_{FWHM} (km s^{-1})
[O II]	3727.0920, 3729.8750	972.002 ± 69.360	43.462 ± 2.788	-	63

3.4 S3

The rest-frame spectral coverage of S3 is from 1261 Å to 2483 Å, and the spectrum in this range can cover rich ultraviolet emission and absorption features. In Figure 3.7, we show the continuum spectrum of S3(b).

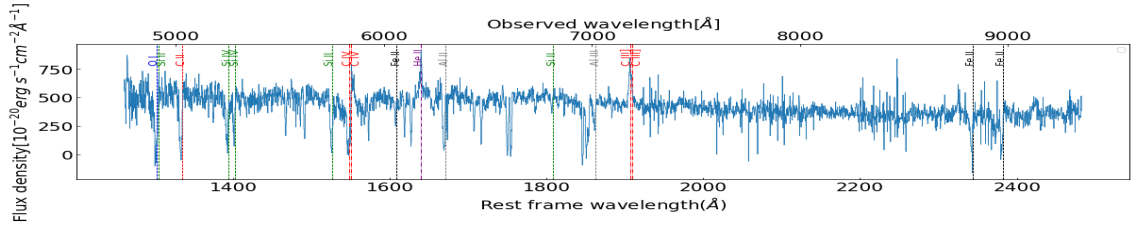


Figure 3.7.: S3(b) continuum spectrum

It is worth noting that the spectrum of S3(b) blends with the spectrum of S0 and the absorption line of a foreground object at $z = 1.357$. Therefore some of the unmarked absorption features do not belong to S3.

We see a large number of emission and absorption features in the spectrum of S3. We will discuss the sources of these features in detail in Sec 4.

3.4.1 Redshift correction of S3

Since the spectrum of S3 cannot cover the wavelengths of [O II] doublet and Lyman α emission, we need to find other emission lines available in the spectrum to measure the redshift. The C III] doublets of S3 are heavily blended with each other, so they cannot be used to measure redshift, while the C IV emission is a P-Cygni profile. Therefore, we can only use the remaining He II 1640 emission line to measure the redshift of S3.

We fit the rest frame profile of He II 1640 and calculate the redshift according to the fitted observed wavelength. We show our fitting results in Figure 3.8 and Table 3.8.

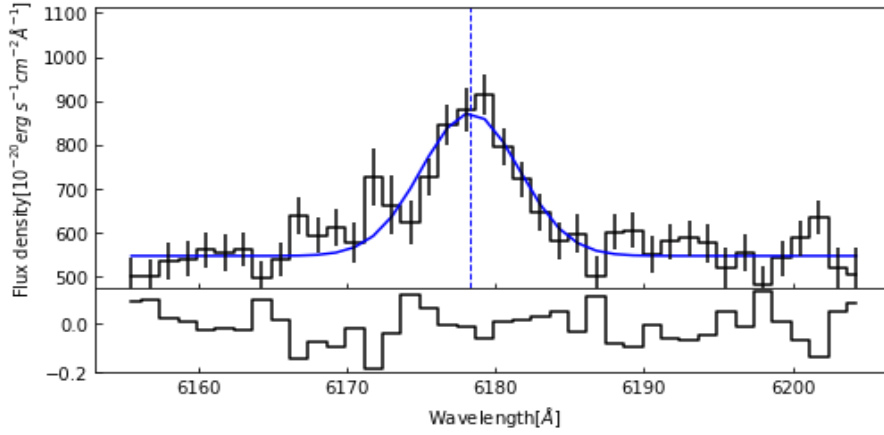


Figure 3.8.: He II 1640 doublet of S3(b)

Table 3.8.: S2(a) [O II] doublet fitting

Line	Amplitude ($10^{-20} \text{erg s}^{-1} \text{cm}^{-2} \text{Å}^{-1}$)	Central wavelength (Å)	FWHM (Å)
He II 1640.00	325.6264	6178.3138	7.7270

Using the redshift formula, we finally got a redshift $z_{S3} = 2.7673$ for S3.

Table 3.9.: Absorption lines in S3

Ion	λ_{vac} (Å)	f	EW_{rest} (Å)	v_c (km s^{-1})	Δv (km s^{-1})
Si IV	1393.7550	0.536	1.892 ± 0.063	-312	-810:190
Si IV	1402.7700	0.262	1.440 ± 0.056	-329	-815:249
Si II	1526.7066	0.127	2.794 ± 0.043	-236	-777:266
Si II	1808.0130	0.00208	0.424 ± 0.022	-253	-578:82
C II	1334.5323	0.129	3.484 ± 0.056	-300	-886:307
Al II	1670.7874	0.000463	2.668 ± 0.047	-364	-955:57
Al III	1862.7895	0.2780	1.211 ± 0.030	-333	-723:78
Fe II	1608.4511	0.0581	0.772 ± 0.035	-256	-632:49
O I, Si II	1302.1685, 1304.3702	0.052, 0.00867	3.554 ± 0.069	-	-
C IV	1548.1950, 1550.7700	0.191, 0.0953	3.810 ± 0.050	-	-

Of course, considering that He II 1640.00 has multiple origins, including stellar wind, AGN, and nebular lines, the redshift we obtained based on this method may not be accurate. The best way to measure redshift is using photospheric

lines (such as C III 1176, O IV 1343, S III 1417, S V 1500, and C III 2297), but they are usually too faint in the spectra of individual galaxies to be observed. It is only possible to see them through a composite spectrum.

3.4.2 Emission and absorption lines of S3

After measuring the redshift of S3, we list the properties of all absorption lines in the S3 spectrum in Table 3.9.

Fe II 2344 and Fe II 2382 absorption lines are very close to the region with very high uncertainty caused by the sky lines. So although they have very significant absorption features, we could not measure their properties precisely.

C IV 1548, 1550 lines are in the form of P-Cygni profile. They are blended with each other and also blended with the Fe II 2344 absorption line from S0.

O I 1302 and Si II 1304 are also blended with each other in a P-Cygni profile.

From Table 3.9, we can see that, like S0, the absorption lines of S3 present very similar velocity centroids and velocity profiles. We will analyze their profiles later.

As we did in Sect 3.2, we can now derive the column density of the corresponding element from the unsaturated absorption lines. We show our results in Table 3.10.

Table 3.10.: Column densities derived from the unsaturated absorption lines in S3

transition	f	EW_{rest} (\AA)	column density (cm^{-2})
Si II 1808.0130	0.00208	0.424 ± 0.022	$7.047 \pm 0.366 \times 10^{15}$
Al III 1862.7895	0.2780	1.211 ± 0.030	$1.419 \pm 0.035 \times 10^{14}$
Fe II 1608.4511	0.0581	0.772 ± 0.035	$5.804 \pm 0.263 \times 10^{14}$

Then we give the emission lines detected in the S3 spectrum in Table 3.11.

Table 3.11.: Emission lines in S3

Ion	λ_{vac} (\AA)	Flux ($10^{-20} \text{ erg s}^{-1} \text{ cm}^{-2}$)	EW_{rest} (\AA)	v_c (km s^{-1})	Δv_{FWHM} (km s^{-1})
He II	1640.0000	1933.177 ± 159.566	3.702 ± 0.036	20	362
C III]	1906.6800, 1908.7300	4050.012 ± 153.669	8.858 ± 0.102	-	395
C IV	1548.2000, 1550.7700	3364.46 ± 219.873	8.013 ± 0.438	-	-

Berg *et al.* (2018) have pointed out that the average low- and high-ionization line profiles can inform gas properties. In Figure 3.9, we show the average velocity profiles from the low-ionization, high-ionization, and combined absorption features for comparison. We also show the He II 1640 emission profile for comparison. Among them, the average high-ionization absorption profile consists of two Si IV absorption lines with an atomic ionization energy of 45.14181 eV. Low-ionization absorption includes Si II, C II, Al II, Al III, and Fe II. Note that the Fe II absorption here does not include the portion contaminated by the sky at the red end of the spectrum. Among them, Al III has the largest atomic ionization energy, 28.44765 eV.

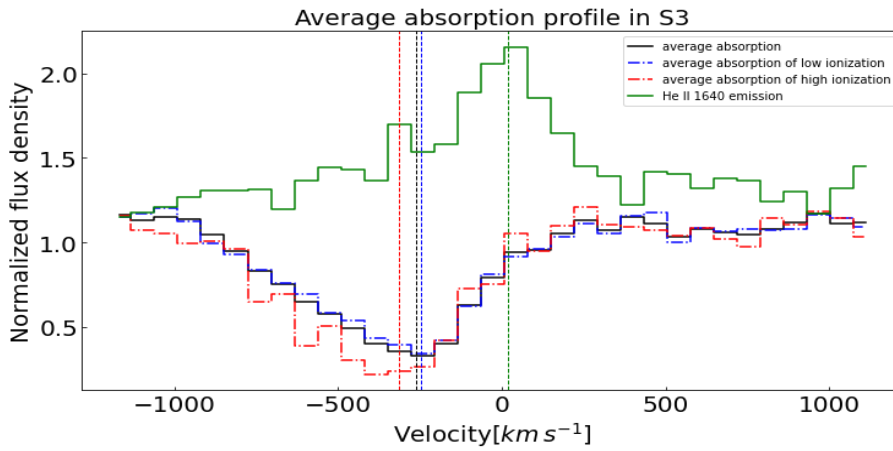


Figure 3.9.: Average absorption profiles

We got the flux-weighted velocity center of the average low-ionization profile, average high-ionization profile, and average profile of all absorptions as $-246.704 \text{ km s}^{-1}$, $-316.206 \text{ km s}^{-1}$, and $-263.318 \text{ km s}^{-1}$, respectively. Obviously, this is far from the velocity centroid (20.158 km s^{-1}) of the He II 1640 emission (In fact, theoretically, since we use He II 1640 to measure the redshift, the velocity center of He II 1640 should be 0. However, obviously, there are

some small differences in the results given by flux-weighted velocity center and Gaussian fitting). Their corresponding velocity FWHM are respectively $425.364 \text{ km s}^{-1}$, $497.318 \text{ km s}^{-1}$, and $436.137 \text{ km s}^{-1}$, which also have no obvious difference. From the profiles in the figure, the difference between low ionization and high ionization is not obvious. Although the velocity centroid of the high-ionization line is slightly larger, it has a very similar shape to the low-ionization profile. We do not wish to explain the kinematics due to line saturation and low resolution, but the existing results are quite different from the almost symmetrical narrow absorption around the system velocity in the absence of gas outflow. Therefore, it is also possible that there is an outflow in S3, but we have not seen the corresponding resonant emission line (of course, this may also be because our spectrum cannot cover the wavelengths of the corresponding fine-structured emission lines). At the same time, the difference between absorption and emission may imply their different origins. Of course, since the redshift of S3 has not been reliably measured, these considerations cannot be 100% certain.

3.5 Foreground object blended with S3 spectrum

We mentioned above that the spectrum of S3 is blended with an object located at a redshift $z \approx 1.357$. In Figure 3.10, we show the rest frame absorption lines from this foreground object in the S3 spectrum.

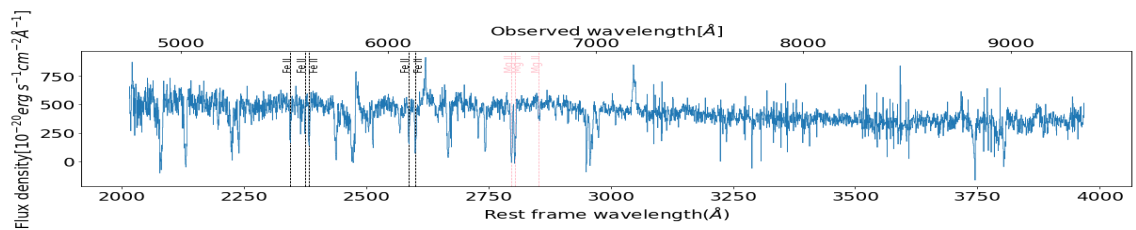


Figure 3.10.: Foreground continuum spectrum

We list these observed absorption lines in Table 3.12. Since we have not observed the emission line of this foreground object, we can only measure that its redshift is around 1.357 through the double peak of the Mg II absorption line.

Table 3.12.: Absorption lines in the foreground object

Ion	λ_{vac} (\AA)	f	EW_{rest} (\AA)	v_c ($km\ s^{-1}$)	Δv ($km\ s^{-1}$)
Mg II	2796.3520	0.629	3.774 ± 0.039	112	-187:495
Mg II	2803.5310	0.308	3.528 ± 0.038	94	-217:407
Mg I	2852.9642	1.80	0.909 ± 0.028	91	-168:334
Fe II	2344.2140	0.114	1.749 ± 0.057	118	-133:477
Fe II	2374.4612	0.0313	0.871 ± 0.064	70	-200:336
Fe II	2382.7650	0.320	2.402 ± 0.058	123	-176:491
Fe II	2586.6493	0.0692	1.770 ± 0.046	124	-122:493
Fe II	2600.1729	0.239	2.526 ± 0.044	100	-151:460

From the table, we can see that the velocity centroid of the absorption line generally has a redshift of about $100\ km\ s^{-1}$, and we also show the column densities derived from these absorption lines in Tabel 3.13.

Table 3.13.: Column densities derived from the unsaturated absorption lines in foreground object

transition	f	EW_{rest} (\AA)	column density (cm^{-2})
Fe II 2374.4612	0.0313	0.871 ± 0.064	$5.577 \pm 0.410 \times 10^{14}$
Mg I 2852.9642	1.80	0.909 ± 0.028	$7.011 \pm 0.216 \times 10^{12}$

3.6 S4

Like the S2, the S4 is likewise a very dim image. The only identifiable emission feature in S4(c) is Lyman α emission. We show the continuum of S4(c) in Figure 3.11.

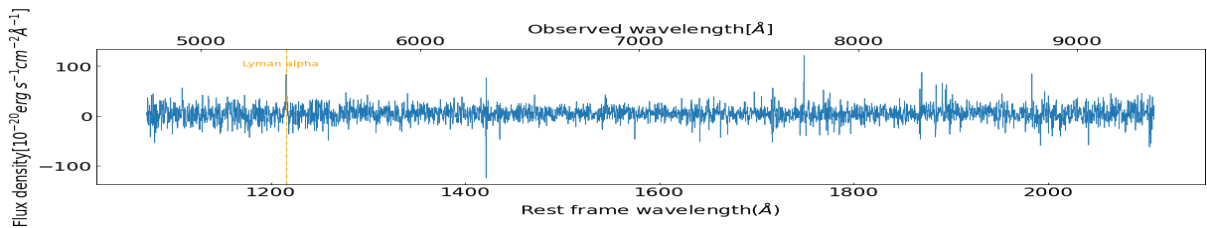


Figure 3.11.: S4(c) continuum spectrum

3.6.1 Redshift correction of S4

By fitting the Lyman α profile with Gaussian as we showed in Figure 3.12 and Table 3.14, we recalculated the redshift of S4 and got the result $z_{S4} = 3.4331$.

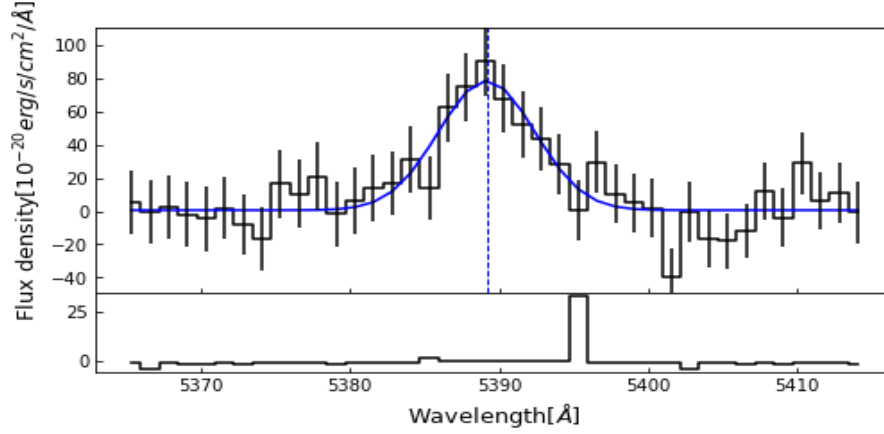


Figure 3.12.: Lyman α emission line of S4(c)

Table 3.14.: S4(c) Lyman α fitting

Line	Amplitude ($10^{-20} \text{ erg s}^{-1} \text{ cm}^{-2} \text{ \AA}^{-1}$)	Central wavelength (\AA)	FWHM (\AA)
Lyman α	77.9762	5389.1679	7.5992

In fact, this is not a common case. In most cases, the shape of the Lyman α line profile is closer to the asymmetric Gaussian, with a blue cutoff and a red wing (Kerutt *et al.* 2022), and only some faint Lyman α lines can be described by the Gaussian profile.

3.6.2 Emission and absorption lines of S4

In Table 3.15, we show the properties of Lyman α emission in S4, but unfortunately, since this is the only feature available in the spectrum, we were unable to do further analysis on the properties of the S4.

Table 3.15.: Emission line in S4

Ion	λ_{vac} (\AA)	Flux ($10^{-20} \text{erg s}^{-1} \text{cm}^{-2}$)	EW_{rest} (\AA)	v_c (km s^{-1})	Δv_{FWHM} (km s^{-1})
Lyman α	1215.67	513.632 ± 70.014	1047.922 ± 2.931	22	411

3.7 S5

We show the continuum spectrum of S5 (a) in Figure 3.13, but because the spectrum is too dim and noisy, we cannot find any obvious emission or absorption features, so we cannot further analyze this object.

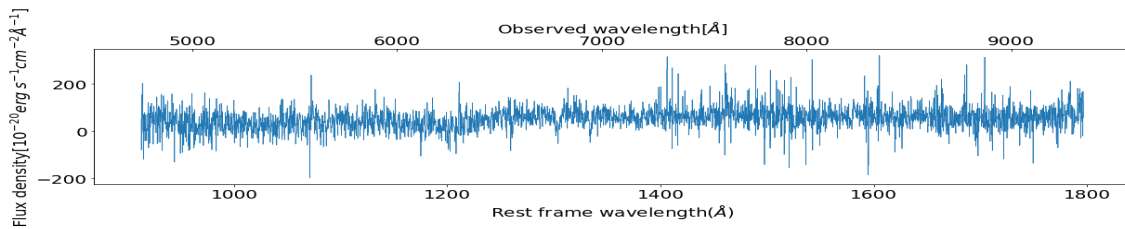


Figure 3.13.: S5(a) continuum spectrum

Analysis of S3 properties

4.1 Spectral features of S3

In order to check the specificity of S3, we used the composite spectrum consisting of about 1000 $z \approx 2$ galaxies obtained by Erb *et al.* (2010) to compare with the normalized spectrum of S3. The normalized spectrum of S3 and the composite spectrum are showed it in Figure 4.1.

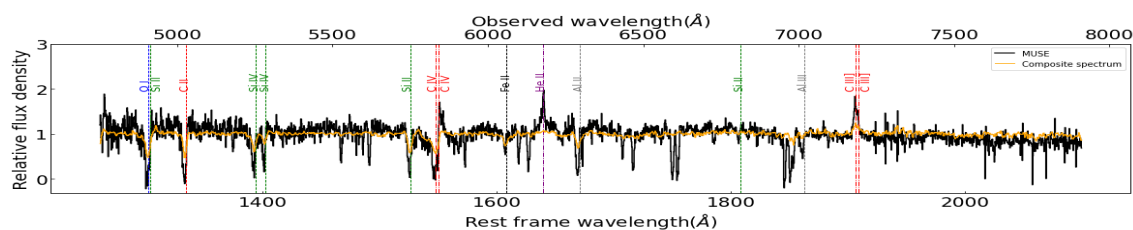


Figure 4.1.: S3(b) spectrum and the composite spectrum of 1000 galaxies at $z \approx 2$

In comparison with the composite spectrum, we can see that most features of the S3 spectrum are consistent with star-forming galaxies in the universe of $z \approx 2$. One of the most notable differences is the strong He II 1640 emission in S3, which can not be observed in the composite spectrum. Next, we specifically discuss the sources of these features in the S3 spectrum.

4.1.1 Stellar winds features

Generally speaking, the features related to stars are mainly divided into two categories, stellar photospheric features, and stellar winds features.

Stellar photospheric features mainly include C III 1176, O IV 1343, S III 1417, S V 1500, and C III 2297 as we mentioned above, that can be used to measure the redshift accurately, and also include a large number of weak absorption features between 1400 and 1500. These features mainly come from the O stars

and B stars in the galaxy. These features are often too faint to be discerned in the spectra of individual galaxies.

Another type of features comes from the stellar wind with a speed of 2000–3000 $km\ s^{-1}$ caused by the radiation pressure of the most massive hot stars (Leitherer *et al.* 1995). Features from weaker stellar winds will show broad blue-shifted absorption, while for strong stellar winds with high density, the P-Cygni profiles will be produced. Typical stellar wind features include N V 1238, 1242, Si IV 1393, 1402, C IV 1548, 1550, and He II 1640, while the latter three are available for S3's spectrum. Si IV features from stellar winds become apparent only in blue giant and supergiant stars, while C IV features caused by stellar winds usually exhibit blue-shifted broad absorption and red-shifted emission, mainly related to main-sequence, giant, and supergiant O stars. Leitherer *et al.* (1995) derive that the red-shifted emission implies the existence of stars with a mass of $30 M_{\odot}$ or more in the galaxy. The broad stellar He II features are mainly produced in the fast, dense stellar winds of Wolf-Rayet (W-R) stars, the evolved descendants of massive O stars. W-R stars usually also have remarkably broad emission lines from highly ionized nitrogen or carbon. At the same time, their stellar winds are also considered to be one of the main sources of carbon in the universe.

There are many difficulties in the research of stellar wind features. Si IV and C IV features in the spectra are usually a combination of stellar wind and photosphere absorption and also contain a strong narrow interstellar absorption component. He II features may also include contributions from AGNs or nebular recombination lines due to the formation of massive stars. Considering the diversity of sources of nebular lines (stellar wind, H II region *et al.*), an emission line may be the result of contributions from multiple origins, and it is also difficult for us to distinguish their origins through the broadening of emission lines.

For the possible AGN contribution of He II, Shapley *et al.* (2003) proposed a diagnostic method based on line ratio. They found that the narrow-line AGN spectrum has line intensity ratios of $C\ IV/Ly\alpha \approx 0.25$ and $C\ III]/Ly\alpha \approx 0.125$. In contrast, the non-AGN spectrum has intensity ratios of $C\ IV/Ly\alpha \leq 0.02$ and $C\ III]/Ly\alpha = 0.05$. In addition, the ratio of $C\ III]/C\ IV$ in the non-AGN spectrum is significantly higher than in the AGN spectrum, indicating a softer photoionizing radiation field. Unfortunately, for our example, Lyman α has a

wavelength outside the coverage wavelength of MUSE, so we can not apply this diagnostic method.

4.1.2 Outflow features

Shapley *et al.* (2003) point out that the fairly common observed velocity shift between emission lines and interstellar absorption lines marks a large-scale outflow of interstellar matter, exactly the same as what we observed in S0 and S3. They mention those low-ionization interstellar lines that can be used to detect neutral outflow gas: Si II 1260, O I+Si II 1303, C II 1334, Si II 1526, Fe II 1608, and Al II 1670. Except for Si II 1260, which is not covered by the wavelength coverage of our spectrum, all other absorption lines are observed in S3. Highly ionized metal features such as Si IV 1393, 1402, C IV 1548, 1550, and N V 1238, 1242 can be used for probing the ionized phase of the outflow. These features predominantly trace gas at $T_e \approx 10^4$ K, which has been ionized by the radiation field from massive stars and collisional processes associated with the outflow. The features of Si IV 1393, 1402 and C IV 1548, 1550 were found in the spectrum of S3.

Shapley *et al.* (2003) also performed a comparison between Si IV doublets and low-electron lines on their samples of Lyman Break Galaxies (LBGs). Like our results, they also found that the blueshift (180 km s^{-1}) of the Si IV doublet is very close to the average blueshift (150 km s^{-1}) of the strong low-ionization interstellar line, only slightly larger. Pettini, Rix, *et al.* (2002) found in a high-resolution spectral analysis of the gravitational lensing system cB58 that one difference is that the high-ionization lines show smoother absorption curves, while the low-ionization lines break down into many discrete components. The resolution of the MUSE spectrum is clearly not sufficient to verify this. However, the average blue shift and velocity FWHM of the profiles are the same as the high-resolution results of cB58, showing a high degree of overall consistency.

4.1.3 Nebular emission lines

C III] 1907, 1909 emission was found in the spectrum of S3. It belongs to the semi-forbidden transition excited by collisions and is thought to arise from

regions of the nebula photoionized by radiation from massive stars and other sources that are still unclear. Another common set of semi-forbidden emission lines is O III] 1661, 1666, but it is not detected in the spectrum of S3. The large-scale outflow of gas cannot absorb semi-forbidden line photons, and the velocity center of C III] 1907, 1909 is relatively consistent with the system velocity, so it cannot come from the outflow. In addition, C IV and He II emissions are also possible to include nebula contributions.

4.2 Estimates of the properties of S3

Based on our observed spectral features, we make a preliminary assessment of the properties of S3 in this section.

4.2.1 Estimation of metallicity

Heckman *et al.* (1998) studied the vacuum ultraviolet spectrum of a sample of 45 starburst and related galaxies observed with the IUE satellite. They gave the relationship between the oxygen metallicity of starburst galaxies and the equivalent width of specific features. The relationship of stellar winds features Si IV 1400 and C IV 1550 vs. metallicity, and interstellar gas features Si II 1260, O I 1302 plus Si II 1304, and C II 1335 vs. metallicity are given separately. Since the C IV absorption part in the S3 spectrum is mixed with the Fe II 2344 absorption of S0, and the spectral resolution of MUSE cannot distinguish the components of O I 1302 and Si II 1304 well, here we make a very rough estimate of the metallicity of galaxies using the stellar winds feature Si II 1394, 1402 and the interstellar gas feature C II 1334, respectively. We show our results in Figure 4.2.

Through the relationship in the figure, we can deduce that the metallicity estimated by stellar winds features is $12 + \log(O/H)_{winds} \approx 8.05$, and the metallicity estimated by interstellar gas features is $12 + \log(O/H)_{gas} \approx 8.41$. If we take solar metallicity as $12 + \log(O/H)_{\odot} = 8.69$, then their metallicity can be expressed as $Z_{winds} = 0.22Z_{\odot}$ and $Z_{gas} = 0.52Z_{\odot}$.

There are significant differences in the results obtained by the two methods. At first, we thought that the results obtained using interstellar gas features should be more credible, considering there may be contributions from the nebula in stellar winds features. However, in the follow-up verification, we found that the results derived using Si IV are more likely to be closer to the real value. On the one hand, considering the monotonically increasing relationship between the equivalent width of features and metallicity, blending with nebula absorption will only make the estimated metallicity larger, but the actual situation is that it is smaller than Z_{gas} . On the other hand, considering that the nebular absorption line has a significant blue shift due to the existence of the outflow, the outflow is likely to have some influence that is not yet known to us on the estimation results. The other possibility is that since these relations are derived entirely based on starburst galaxies, they may not apply to all types of galaxies.

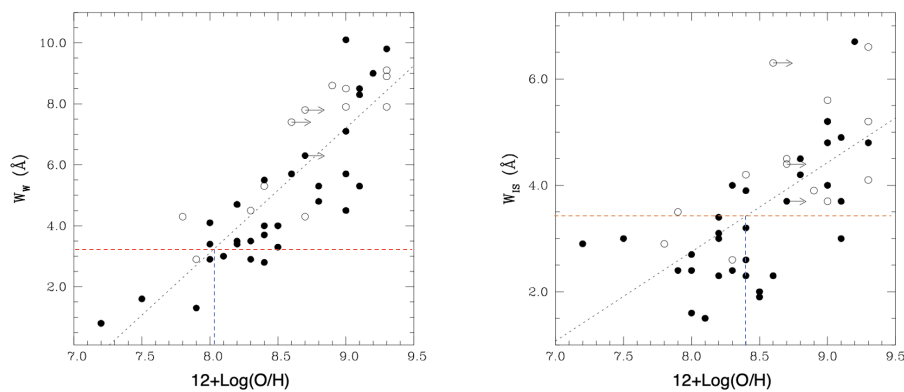


Figure 4.2.: Diagnostic diagram from Heckman *et al.* (1998). We mark the equivalent width of the corresponding emission with a red horizontal dashed line and mark the derived metallicity with a blue vertical dashed line. The left picture shows the relationship between stellar features and metallicity, and the right picture shows the relationship between interstellar gas features and metallicity. The filled circles are the starbursts with the best IUE spectrum ($S/N > 15$), the open circles are the starbursts with moderately good IUE spectrum ($S/N = 10 - 15$), and the dashed diagonal line is a least-squares fit to the data points.

According to Heckman *et al.* (1998), this Z dependence is due to the fact that the stellar wind can contribute significantly to these lines, and the strength of the stellar wind is related to the rate of stellar mass loss, which in turn are a function of the metallicity (Maeder and Conti, 1994). This theory may offer

another possible explanation for the failure of the interstellar gas method: These interstellar gas features are not so tightly related to the stellar winds.

4.2.2 Star formation rate and stellar mass

There have been many studies to date on methods for measuring the star formation rates (SFRs) of galaxies. Research on the calibration of SFR indicators spans the entire electromagnetic spectrum, from X-rays, ultraviolet (UV), optical, and infrared (IR), all the way to radio, and both continuum and line emissions are used at the same time.

Estimates of the star formation rate independent of the influence of a galaxy's dust content are generally based on its radio continuum emission. After eliminating the contamination of radio signals by AGNs, the total star formation rate in galaxies can be estimated from the radio luminosity through radio-FIR correlation (Condon, 1992).

Obviously, the radio spectrum of S3 is not available. We therefore need methods for estimating the SFR of galaxies using UV spectra. For S3, the most serious difficulty is that we know almost nothing about the details of the dust extinction of S3 itself, so we cannot get the UV spectrum of S3 after removing the influence of dust. One way to get some rough information about the dust extinction of galaxies is, if we assume that the UV emission of a galaxy is dominated by a young stellar population, then the shape of its UV continuum can be regarded as the power law of the wavelength:

$$F_{\lambda} \propto \lambda^{\beta} \quad (4.1)$$

F_{λ} is the observed flux density ($\text{erg s}^{-1} \text{cm}^{-2} \text{\AA}^{-1}$), and β is the continuum slope, which is strongly correlated with the nebular extinction measured in the optical using the Balmer decrement, and by far the most commonly used dust obscuration indicator.

The value of β varies from galaxy to galaxy. It mainly depends on the age of the galaxy and whether there is dust. In general, the youngest galaxies (a few million years old) have a β value of about -2.5. As galaxies get older, their spectra get redder, so the β becomes larger, and at the same time, the

reddening caused by dust also makes β larger. Usually, β is parameterized as the ratio of the infrared to UV luminosity, L_{IR}/L_{UV} , but for S3, we roughly estimate its β value to be 0 by fitting the UV continuum.

Meurer *et al.* (1999) found an empirical relation between the ultraviolet spectral slope and dust extinction at 1600 Å, which provide us with a method to get dust extinction information from β :

$$A_{1600\text{\AA}} = 4.43 + 1.99\beta \quad (4.2)$$

We substitute $\beta \approx 0$ to get the dust extinction $A_{1600} \approx 4.43$.

Once we have the value of dust extinction, we can use the relation from Kennicutt Jr (1998) scaled to a Kroupa IMF to derive the SFR:

$$SFR_{UV}(M_{\odot} \text{ yr}^{-1}) = 0.9 \times 10^{-28} \times L_{1500\text{\AA}}(\text{erg s}^{-1} \text{ Hz}^{-1}) \quad (4.3)$$

The luminosity at 1500 Å is corrected by $A_{1600\text{\AA}}$ and calculated as the average flux in the wavelength windows of 1350 and 1650 Å. It is worth noting that our spectrum has been magnified by gravitational lensing, so we need to correct the magnification factor before using luminosity to estimate SFR. In Table 4.1, we showed the SFR calculated according to the luminosity corrected by magnification factors of different lensing models applied by Wang *et al.* (2022).

After obtaining the SFR, we hope to further estimate the stellar mass of the galaxy. Pannella *et al.* (2009) gave a formula to write SFR as cosmic time t and stellar mass M_* :

$$\langle SFR \rangle = 270 \times (M_*/10^{11}M_{\odot}) \times (t/3.4 \times 10^9 \text{ yr})^{-2.5} \quad (4.4)$$

We take cosmic time $t = 2.305$ Gyr at $z = 2.7673$, and the SFRs corresponding to the three models have been calculated so that the stellar mass can be calculated. We present the results according to 3 different magnification factors in Table 4.1 too. After the SFR and stellar mass are known, the specific star formation rate (sSFR) of S3 can also be calculated.

It is worth noting that Pannella *et al.* (2009) emphasize that this relation is best valid for the galaxies with $M_* \approx 3 \times 10^{10}M_{\odot}$ and $z < 2.4$ ($t > 2.7$

Gyr). Considering that the redshift of S3 is $z = 2.7673$, the results obtained by this method may not reflect the real situation of S3 well. On the other hand, this relation is the average of a large number of samples in the universe, and we lack information about the dispersion of the relation. Therefore, we tend to think that the application of this relationship on a specific galaxy cannot guarantee an accurate estimation of the stellar mass of S3.

Table 4.1.: S3 properties of different magnification models

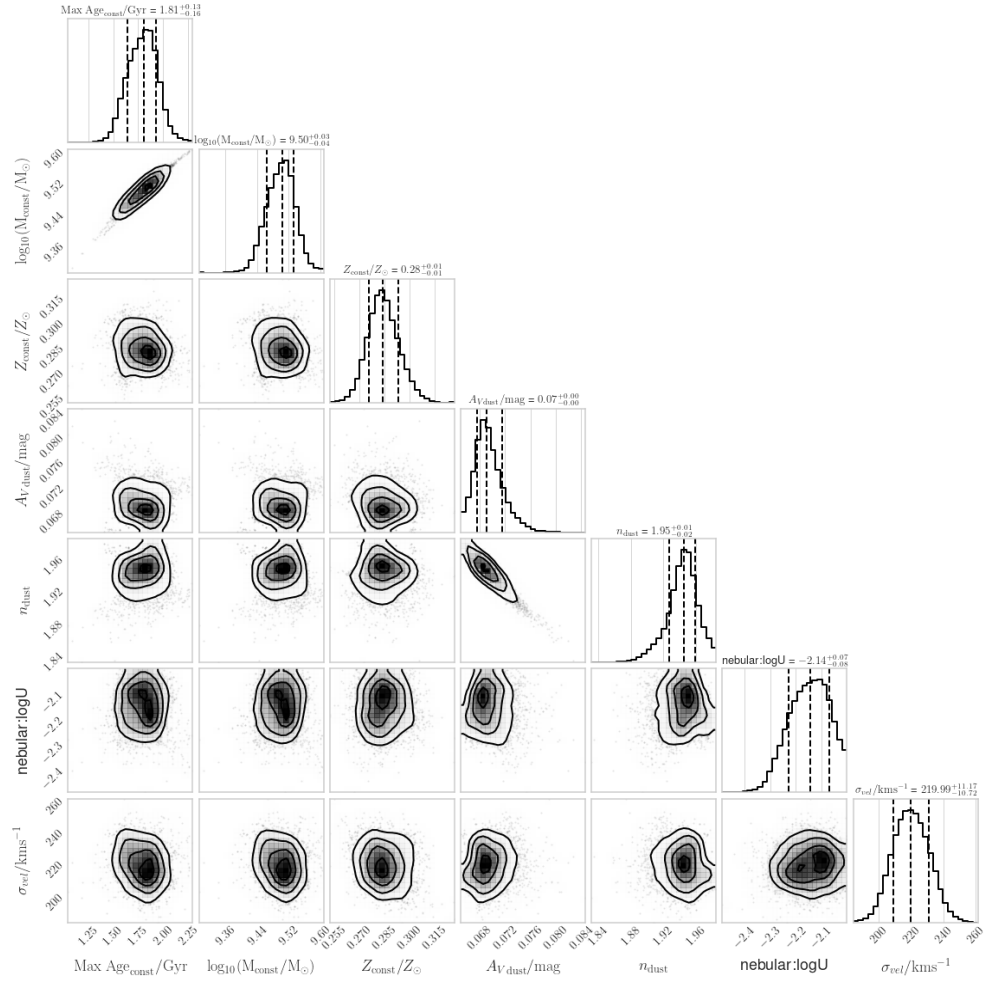
Model	Magnification factor	$L_{1500\text{\AA}}$ ($10^{28} \text{ erg s}^{-1}$)	M_* ($10^8 M_\odot$)	SFR ($M_\odot \text{ yr}^{-1}$)	$\log(\text{sSFR})$ (yr^{-1})
Img-MP(L)	-103.21	4.067	5.130	3.661	-8.147
Esr2-MP _{test} (L)	-86.87	4.832	6.095	4.349	-8.147
Img-MP(L/D)	-119.23	3.521	4.442	3.169	-8.147

From Table 4.1, we can see that if our rough estimate is not much different from the real result, then S3 is a metallicity-poor dwarf galaxy with a low star formation rate. This does not seem to fit with our general impression of massive star formation in the early Universe at $z = 2-3$.

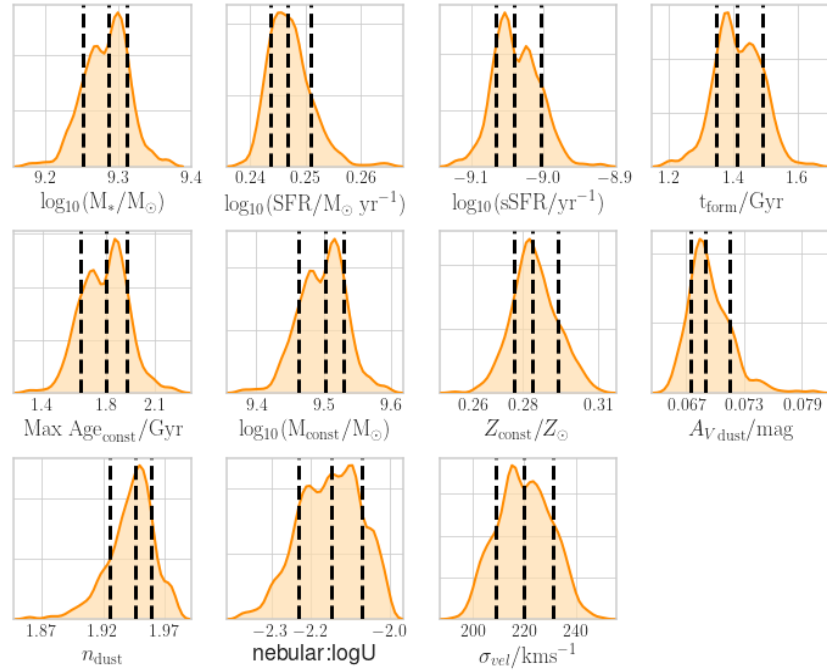
4.2.3 BAGPIPES fitting

In order to verify whether our estimation results are reasonable, we used Bayesian Analysis of Galaxies for Physical Inference and Parameter Estimation (BAGPIPES) to fit the magnification-corrected continuum UV spectrum of S3. BAGPIPES is a Python code package for fitting and modeling galaxy spectra. It can perform a series of functions, such as creating spectrum models, fitting observed spectra, and deriving galaxy properties. In order to obtain the properties of galaxies through the spectral fitting, we need to use the observed spectrum as input, specify the attenuation curve and star-formation history model for the fitting model, and then specify the range of parameters we want to fit (such as stellar mass, star formation rate, ionization parameter, etc.).

For our model, we chose a constant star formation history and CF00 attenuation curve, and left other parameters free. We showed the results of the three models in Table 4.2.

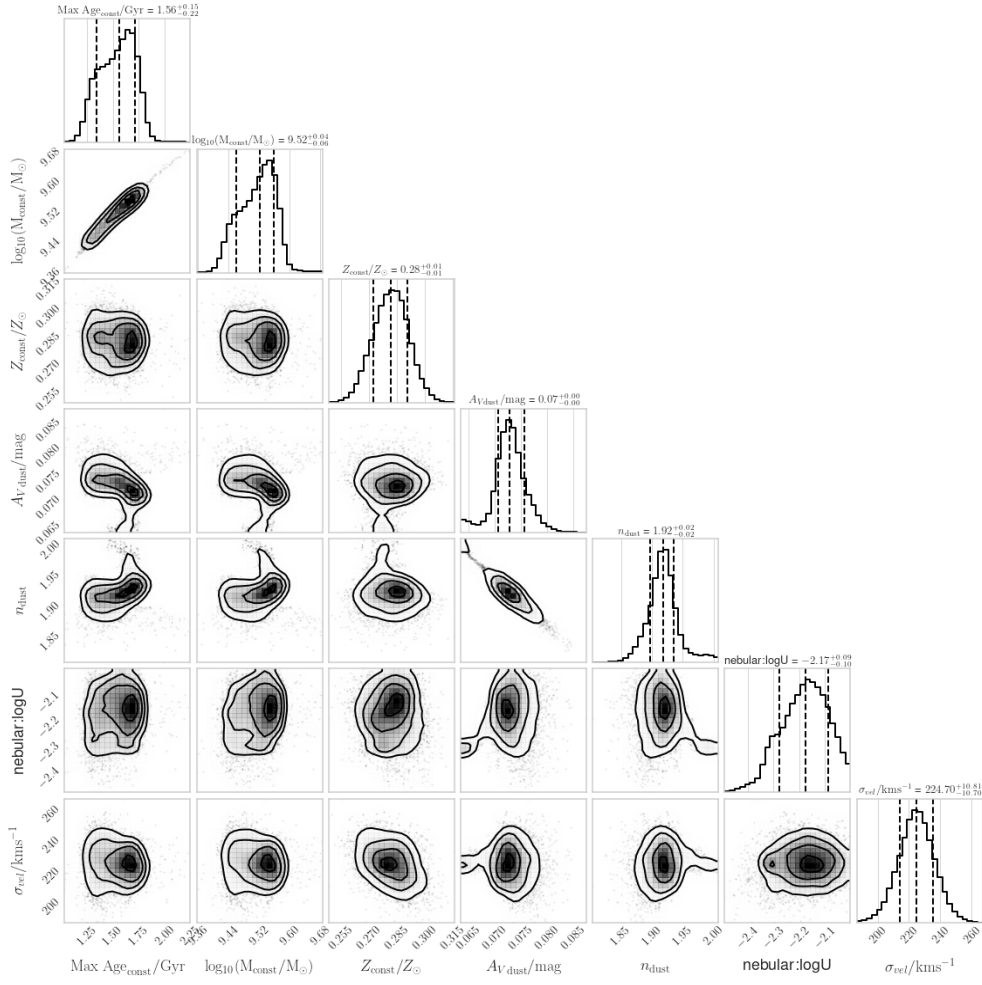


(a) corner plot

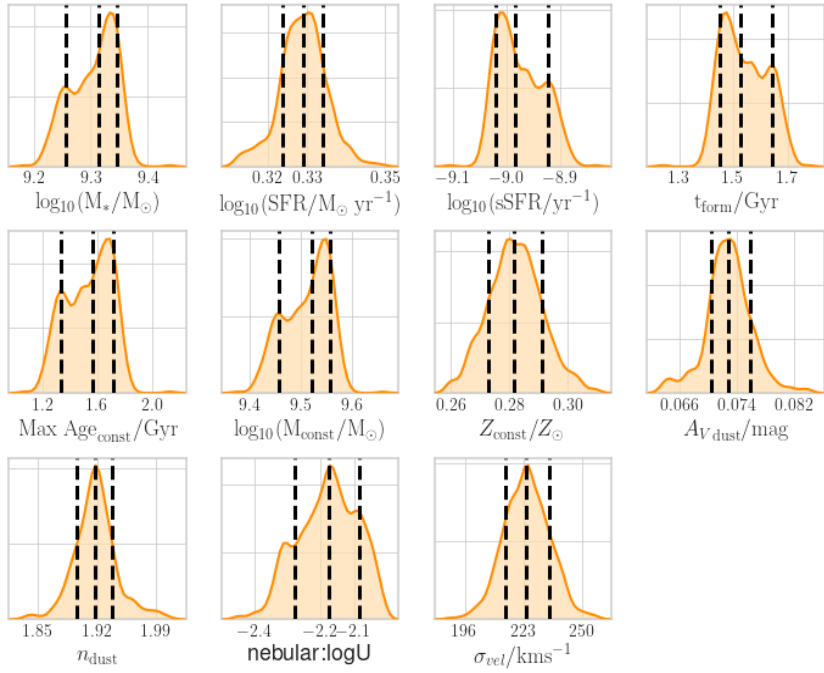


(b) 1-D posterior plot

Figure 4.3.: Diagnostic polts of Img-MP(L)

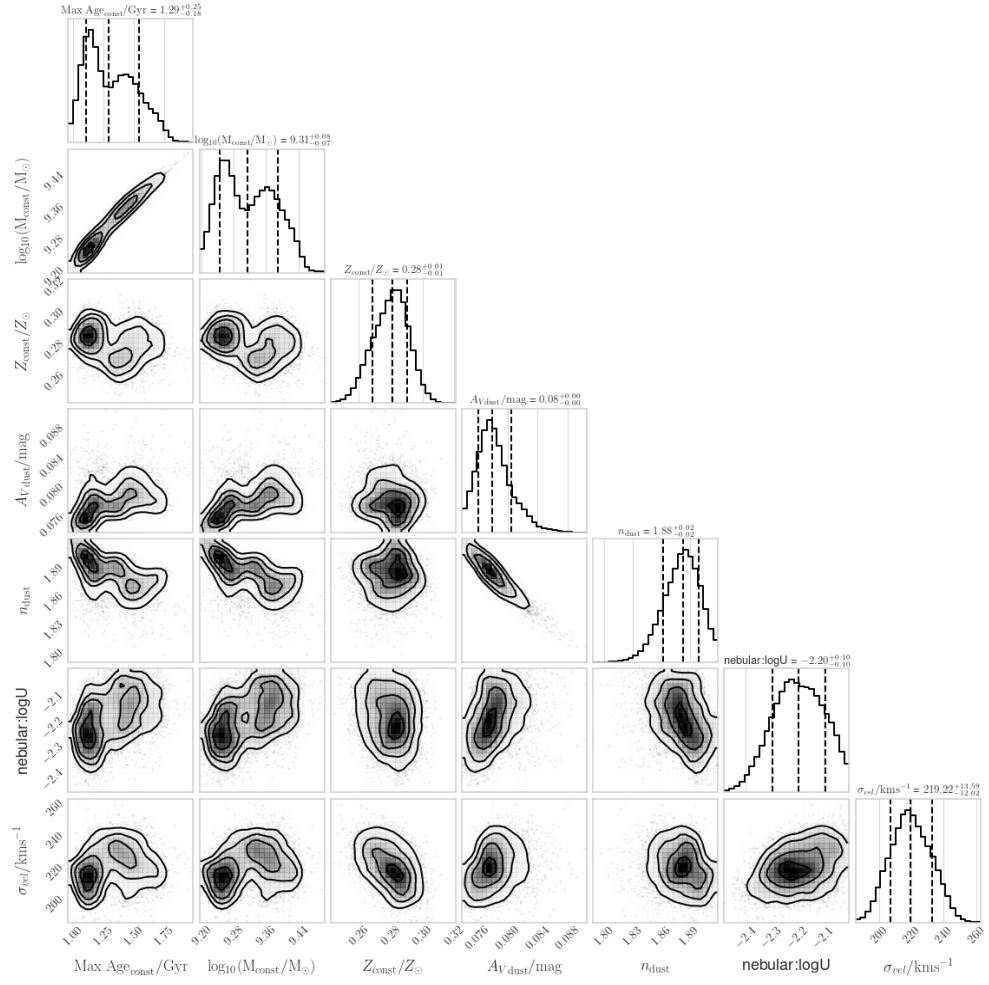


(a) corner plot

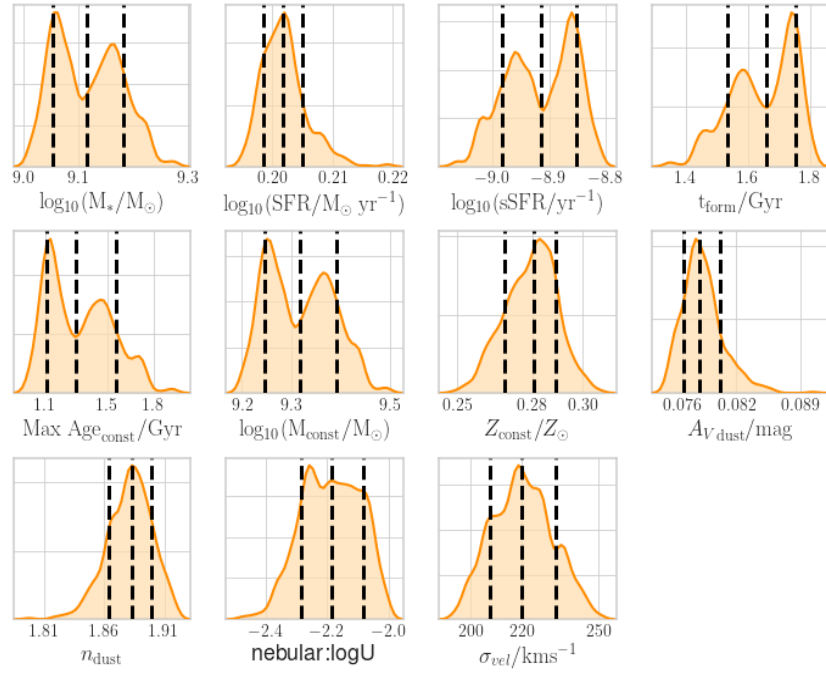


(b) 1-D posterior plot

Figure 4.4.: Dignostic polts of Esr2-MP_{test}(L)



(a) corner plot



(b) 1-D posterior plot

Figure 4.5.: Dignostic polts of Img-MP(L/D)

Table 4.2.: BAGPIPES fitting of S3

Model	Magnification factor	Z_* (Z_\odot)	$\log(U)$	A_{Vdust} (mag)	M_* ($10^8 M_\odot$)	SFR ($M_\odot yr^{-1}$)	$\log(sSFR)$ (yr^{-1})
Img-MP(L)	-103.21	0.28	-2.14	0.07	19.50	1.76	-9.05
Esr2-MP _{test} (L)	-86.87	0.28	-2.17	0.07	20.42	2.13	-8.99
Img-MP(L/D)	-119.23	0.28	-2.20	0.08	12.88	1.59	-8.91

Z_* represents the stellar metallicity, and U is the ionization parameter.

In Table 4.2, we see that the metallicity value given by BAGPIPES is very close to the value $0.22 Z_\odot$ we estimated based on stellar wind features. The stellar mass given by BAGPIPES is about three times of our estimated result, and the star formation rate is about half of the result given by equation 4.3, so it gives a smaller sSFR. Considering that our estimation method is very crude, we are more inclined to think that the stellar mass given by equation 4.4 is too low and trust the results given by BAGPIPES. We think that the main reason for this difference may be that our estimation of the spectral slope is very rough, and the method of inferring the stellar mass is a statistical result based on a large number of samples which is mainly applicable to the galaxies with $z < 2.4$. In Figure 4.3 to Figure 4.5, we show the BAGPIPES diagnostic maps of the three models. According to the SFR - stellar mass relation given by Huang *et al.* (2023), the star formation rate of main sequence galaxies in this range should be around $1.7 - 5 M_\odot yr^{-1}$. Obviously, this is relatively close to the result we obtained through equation 4.3 and fitting, so we think S3 is a dwarf galaxy without the starburst phenomenon, which means that its star formation rate is not significantly higher than the long-term average star formation rate for a galaxy of this mass. As a result, we think there is no vigorous star formation activity in this galaxy, although S3 is in the stage of massive star formation in the universe.

4.3 Simulation of stellar population

In this section, we try to study the stellar population in S3.

In the spectrum of S3, we observed obvious stellar wind features. Among them, we cannot determine the composition of Si 1393, 1402 from nebular absorption lines, and He II 1640 may also have many different sources. In contrast, the P-Cygni profile of C IV 1548,1550 has the most prominent stellar wind features. Although narrow absorption from nebular lines is also possible in the C IV feature, the P-Cygni profile allows us to roughly distinguish the absorption from the nebula from the emission from the stellar winds. Therefore, we used the simulated spectra generated by the Binary Population and Spectral Synthesis code (BPASS) (Eldridge *et al.*, 2017) v2.1 to fit the observed C IV P-Cygni profile to search for the stellar population most likely to be the source of incident radiations of S3, both the observed and simulated spectra are normalized by their own continuum.

The idea behind the establishment of the BPASS model is that the individual stellar models are combined together to make a synthetic stellar population in the population synthesis. In the spectral energy distribution (SED) as the simulation output, the stellar ages, metallicity, and the initial mass function(IMF) are the main three parameters.

The output age of BPASS varies from $\log(\text{Age}/\text{yrs}) = 6.0$ to 11.0 (1 Myr to 100 Gyr), and there are 14 different choices for the metallicity: $Z = 10^{-5}, 10^{-4}, 0.001, 0.002, 0.003, 0.004, 0.005, 0.006, 0.008, 0.010, 0.014, 0.020 (Z_{\odot}), 0.030, 0.040$. As for the initial mass function, we have 7 different options. The fiducial models are based on the IMF of Kroupa *et al.* (1993), with a power law slope from 0.1 to $0.5 M_{\odot}$ of -1.30 which increases to -2.35 above this. The power law slope extends to a maximum initial stellar mass of $100 M_{\odot}$ or $300 M_{\odot}$. In addition to these standard models, there are also models with two different upper IMF slopes of -2.00 and -2.70 , as well as varying the upper maximum initial stellar mass to $100 M_{\odot}$ or $300 M_{\odot}$. The final alternative has a slope of -2.35 from 0.1 to $100 M_{\odot}$. For each model, there are both single star and binary options, where the binary model takes the extra mass loss or gain via binary interactions into account.

We use reduced chi-square fitting to measure the quality of spectral fitting. The reduced chi-square χ_{red}^2 could be calculated as:

$$\chi_{red}^2 = \frac{\chi^2}{\nu} = \frac{\sum_i \frac{(O_i - C_i)^2}{\sigma_i^2}}{\nu} \quad (4.5)$$

O_i is the observations, C_i is the simulated data, σ_i^2 refers to the variance of the data, and ν is the degree of freedom which equals to 1 for our case of fitting the spectrum.

In Figure 4.6, we show the best-fit result of the C IV P-Cygni profile of S3.

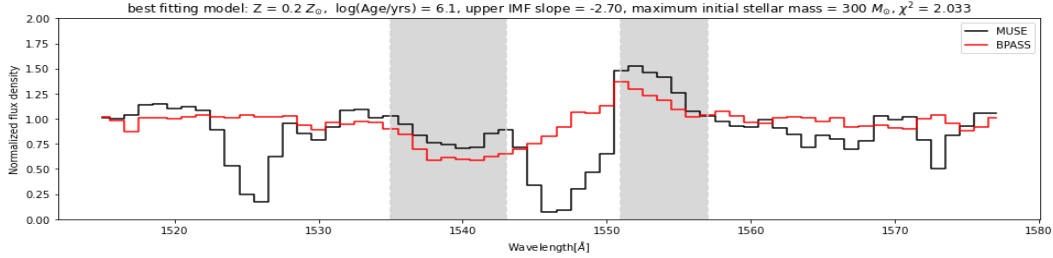


Figure 4.6.: The best-fit result of the C IV P-Cygni profile of S3. The spectrum in the gray area is the part used for χ^2 fitting. We ignore the absorption part in the middle because it may contain a narrow absorption from the nebula, and at the same time, we know it blends with Fe II 2344.

From the fitting result, we can see that the best-fit model has a $\chi^2 = 2.033$. This is a very young single-star population with a metallicity of $0.2 Z_{\odot}$, which is very close to the results given by stellar wind features ($0.22 Z_{\odot}$) and BAGPIPES ($0.28 Z_{\odot}$).

Table 4.3.: Top 10 best fit models of stellar population

upper IMF slope	maximum initial stellar mass (M_{\odot})	Z (Z_{\odot})	log(Age/yr)	χ^2
-2.70	300	0.2	6.1	2.033
-2.00	100	0.2	6.2	2.035
-2.00	100	0.3	6.1	2.059
-2.35	300	0.3	6.0	2.069
-2.35(all)	100	0.2	6.2	2.097
-2.35	100	0.2	6.2	2.097
-2.35	100	0.3	6.1	2.142
-2.35(all)	100	0.3	6.1	2.142
-2.70	300	0.3	6.0	2.160
-2.35	100	0.2	6.2	2.163

In Table 4.3, we show the top 10 best-fit models. It can be seen that they all have very similar ages and metallicity, and the main difference is reflected in the IMF parameters ("all" represents the case of IMF slope of -2.35 from 0.1 to

100 M_{\odot}). These results further illustrate that the stellar population in S3 is young and metal-poor.

Of course, it is worth noting that this is only the simplest estimate of the stellar population based on BPASS. Here we do not consider the effects of continuous star formation and the mixing of single stars and binaries, so this is still a relatively rough estimate.

Simulation of S3

In the previous section, we discussed the properties of S3, but the type and properties of the incident radiation field of S3 are still unknown to us.

In this section, we use the CLOUDY photoionization model (Ferland *et al.* 2017) to simulate the conditions of AGN and stellar population as the source of the incident radiation field. CLOUDY is a code for the numerical simulation of spectra. It simultaneously and self-consistently computes ionization, chemistry, radiation transport, and dynamics based on atomic and molecular processes. The result is a prediction of the material's conditions and observed spectrum. At the same time, we also use the MAPPINGS III library (Allen *et al.* 2008) to introduce the impact of shocks.

To measure the quality of the simulation results, we took two different approaches to assess how well the simulations matched the observed data. For those models where the continuum spectrum can be obtained directly, we first perform a reduced chi-square fit on the entire continuum spectrum. Then, we check whether our model can reproduce the three sets of line ratios (C IV/He II, C III]/He II, C IV/C III]) we observed in S3 to the greatest extent. To do this, we create a three-dimensional phase space with three line ratios as the coordinate axis and take the simulation result with the shortest distance to the position of S3 in the phase space as the best fit. For those models with shocks added, since the MAPPINGS III Library does not provide continuum spectra, we can only evaluate the quality of the model through line ratios.

5.1 Model settings

In this section, we describe the basic settings of the CLOUDY model, including the basic properties of the incident radiation field, the geometry settings of the gas, and the metallicity settings.

5.1.1 Incident radiation fields

Here, we choose the spectrum of the best-fit stellar population given by the BPASS simulation as the default incident radiation and its intensity is specified by the ionization parameter $\log(U) = -2.14$ given by BAGPIPES.

5.1.2 Geometry

We use the default open geometry of CLOUDY, which means all radiation that escapes from the illuminated face of the cloud, towards the source of continuous radiation, then escapes from the system without further interaction with gas. According to the CLOUDY tutorial, the open geometry is common in the broad-line region of active nuclei or a blister H II region which means the exciting star is very close to the edge of the neutral cloud. Another option is closed geometry. In this case, the central object is small relative to the nebula, then all diffuse fields which escape from the illuminated face of the cloud in the direction towards the central object will go on to strike the far side of the nebula. The closed geometry is thought to be closer to the case of planetary nebulae and H II regions. In fact, I also tried closed geometry, but the overall shape of the output spectrum in this case is very different from the observations. Therefore, we still use the open geometry model as the basis in the following discussion.

The inner radius of the cloud should be given by the Strömgren radius. For example, the Strömgren radius of a typical O6 star is about 74 parsec. Considering that the best-fit stellar population given by the BPASS we selected is quite young, this is a very reasonable guess. Actually, since the inner radius of the cloud is only used to calculate the number of photons impinging on the inner surface of the cloud, and the intensity of the incident field here is given by the intensity command ionization parameter U , in fact, we do not need to specify the inner radius of the model.

5.1.3 Metallicity

Following Jaskot and Ravindranath (2016), we set multiple possibilities for metallicity in the nebula. Considering that the gas phase metallicity is usually

larger than the stellar population metallicity, here we set 9 different metallicity options: $0.25 Z_{\odot}$, $0.3 Z_{\odot}$, $0.4 Z_{\odot}$, $0.5 Z_{\odot}$, $0.6 Z_{\odot}$, $0.7 Z_{\odot}$, $0.8 Z_{\odot}$, $0.9 Z_{\odot}$, $1.0 Z_{\odot}$. Considering that C/O and N/O ratios vary among galaxies, we do the same as Jaskot and Ravindranath (2016), considering models with a range of C/O and N/O ratios. We scale the default C/O and N/O ratios from the CLOUDY ISM abundance set by factors of 0.05, 0.15, 0.25, 0.45, 0.65, 0.85, and 1. We used the default ISM dust settings provided by CLOUDY, and the hydrogen densities of the models have 5 different options: 1 cm^{-3} , 10 cm^{-3} , 100 cm^{-3} , 1000 cm^{-3} , and 10000 cm^{-3} .

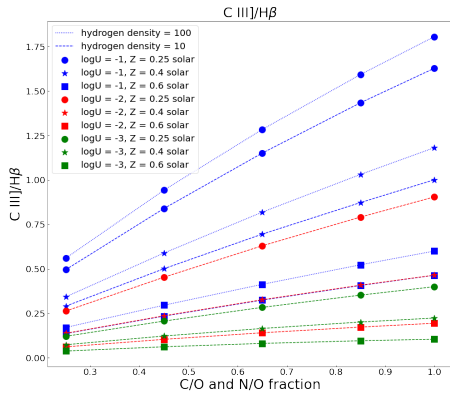
5.2 Pure photoionization model of stellar population

We first tried a model that included only the stellar population in the incident radiation.

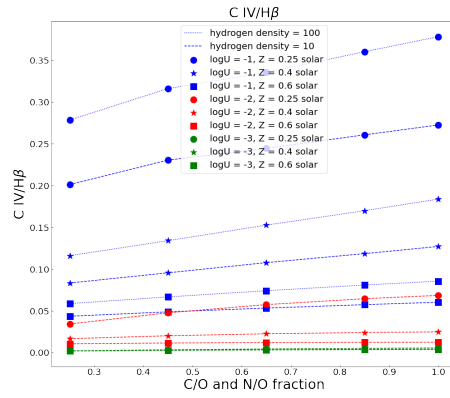
5.2.1 General trend

Before discussing the model that best fits the observed data, we investigate the general effect of different model parameters on line ratio. We show the general trend in Figure 5.1.

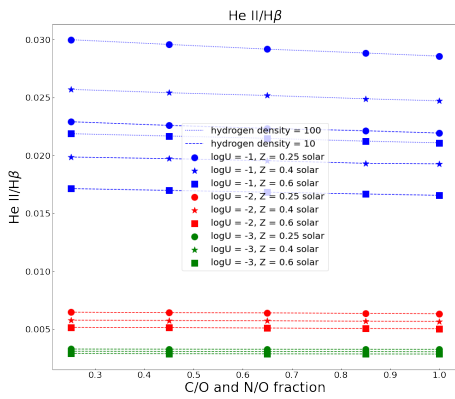
In Figure 5.1 (a), (b), and (c), we found that larger ionization parameters lead to stronger relative $H\beta$ intensity. The intensity of C III] and C IV increases monotonously with the increase of the C/O ratio. It is easy to understand because it means that more elements are ionized and generate emissions. Higher hydrogen density also results in stronger intensity. We think this is because 90% of the heating of nebula gas comes from photoionization photons generated by hydrogen photoionization, so higher hydrogen density means higher temperature.



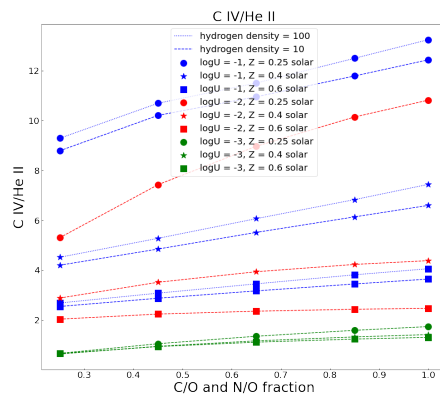
(a)



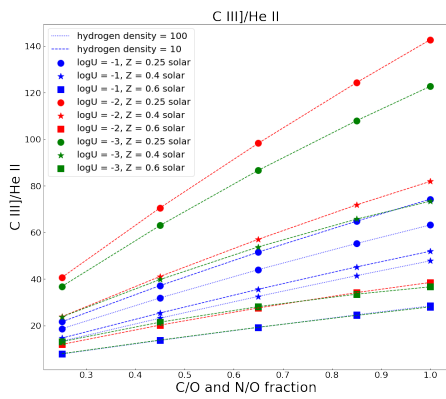
(b)



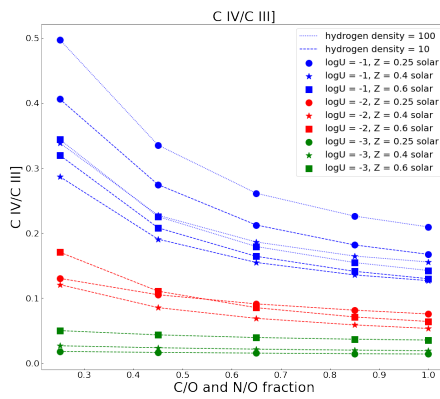
(c)



(d)



(e)



(f)

Figure 5.1.: General trend of pure photoionization model of the stellar population

Another interesting trend is that in Figure 5.1 (a), (b), and (c), the increase in metallicity often leads to a decrease in the value of line ratios. We think this is due to the fact that metals are the main coolants in the nebula, so higher metallicity means lower temperatures. For recombination lines, the emission coefficient $j_{nn'}$ is related to the effective recombination coefficient $\alpha_{nn'}^{eff}$ (nn' means the transition from level n to level n'):

$$j_{nn'} = \frac{h\nu_{nn'}}{4\pi} n_e n_p \alpha_{nn'}^{eff} \quad (5.1)$$

Since the cross section of elastic scattering between electrons is very large compared to other cross sections, this will set the energy distribution of electrons to a Maxwell-Boltzmann distribution, so the recombination coefficient is related to temperature. It varies approximately as $T^{\frac{1}{2}}$. At the same time, for C III], due to the temperature dependence of collisional rates, C III] lines also exhibit high sensitivity to metallicity.

In Figure 5.1 (d) and (e), we present the trends of C IV/He II and C III]/He II, respectively. Obviously, they increase monotonically with the C/O ratio since there is more carbon to be ionized, while He II is hardly affected. Both the increased hydrogen density and the decreased metallicity will lead to the increase of C IV/He II. Since these two effects will lead to an increase in temperature, we think that C IV is more sensitive to temperature than He II. C III] /He II ratio also increases with the decrease of metallicity but decreases with the increase of hydrogen density. We think this is because C III] is more sensitive to temperature than He II, but the increased hydrogen density will reduce the transition probability of C III].

In Figure 5.1 (f), we found that C IV/ C III] ratio shows different dependence on metallicity at different ionization parameters. At low ionization parameters, the low metallicity case has a smaller line ratio. However, as the ionization parameter increases, the line ratio of low metallicity becomes larger than that of the medium and high metallicity cases. We think that this may be due to the fact that in the case of low ionization parameters, the collision excitation is more affected by temperature changes, and the number of ions that can generate C IV is insufficient. The trend about hydrogen density shows once again that the transition probability of C III] will decrease due to the increase of hydrogen density, thereby reducing C III] emission. And C IV/C III] ratio decreases with the increase of the C/O ratio, which proves that in our model,

compared with C IV, increasing the content of carbon element will increase C III] emission more significantly.

5.2.2 Best fit model

In Figure 5.2, we show the best-fit spectrum obtained using the reduced chi-square fit. Note that we remove features generated by the spectrum from foreground objects and S0 during the fitting.

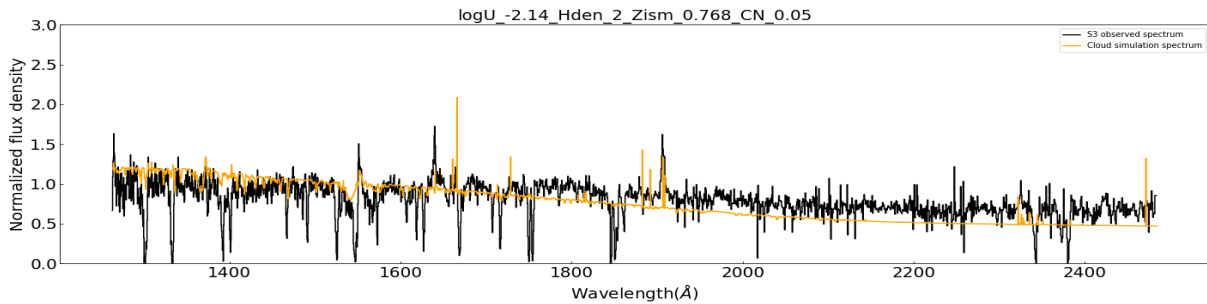


Figure 5.2.: The spectrum of the best model obtained using the reduced chi-square fit method. For this model, $\chi_{red}^2 = 6.519$, hydrogen density $n_H = 100 \text{ cm}^{-3}$, metallicity $= 0.5 Z_{\odot}$, and the scale factor of C/O and N/O ratio $= 0.05$

Obviously, the output spectrum obtained by simulation is far from the observation result, and the simulation result has an obvious slope. We thought at first that this might be due to the low amount of dust in the simulation, but when we added twice the amount of dust to the simulation, the situation did not improve. In order to match the slope of the simulated continuum with the observed results, we first considered the case where the reddening of the spectrum is entirely caused by dust extinction. The specific method is to regenerate the simulated spectrum without dust settings and directly use the extinction function given by Calzetti *et al.* (2000) to correct the simulated spectrum. We eventually found that in order for the slope of the simulated spectrum to match the observed one, the value of A_V needs to be set to around 0.6 mag, which is much larger than the estimated value of 0.07-0.08 given by BAGPIPES. At the same time, line ratio fitting also failed to give reasonable fitting results. From this, we conclude that the pure stellar population photoionization model cannot simulate the output spectrum of S3 well.

5.3 Shocks

Since pure stellar population photoionization cannot reproduce our observations, we consider introducing contributions from other sources into the incident radiation of the model. We first consider the impact of shocks. There are many possibilities for the origin of shocks, such as the expansion of the H II region, cloud-cloud collisions, stellar winds, supernova explosions, etc. These effects compress, heat, and accelerate interstellar gas and generate shocks.

Shocks play an important role in the dynamics and evolution of the interstellar medium. The specific structure of shocks has been extensively studied, including detailed modeling of fluid dynamics, heating, cooling, and chemistry. According to the model of interstellar shocks given by Shull and McKee (1979), the structure of a radiating shock may be divided into several regions: (1) a radiative precursor which may preionize the gas; (2) a relatively thin adiabatic layer (the “shock front”) in which the directed flow ahead of the shock is converted into random thermal motions; and (3) a much broader cooling region in which collisional excitation and ionization cause the temperature to drop.

Shull and McKee (1979) also discuss the impact of shocks on emission spectra. The radiative precursor is of fundamental importance in interstellar shocks, as it determines the ionization state of the gas entering the shock front, which in turn determines the cooling rate and emission spectrum behind the precursor. In their model, the H Balmer lines and some He II emission lines are mainly produced by recombination, with some contamination by collision excitation. Therefore, their intensity is sensitive to the preionization state of H and He as well as to the peak ionization produced by collisional ionization in the postshock gas, while the metal lines are almost entirely excited by electron collisions behind the shocks. These lines produced by collision excitation are very sensitive to the velocity of shocks. The intensity of collision excitation lines increases rapidly with shock velocity.

In this section, we use the MAPPINGS III library (Allen *et al.*, 2008) of fast radiative shock models to study the impact of the shock contribution on the photoionization model. The library consists of grids of models with shock velocities in the range $v_s = 100 - 1000 \text{ km s}^{-1}$ and magnetic parameters $B/n^{1/2}$

of 10^{-4} to $10 \mu\text{G cm}^{3/2}$ for five different atomic abundance sets and a preshock density of 1.0 cm^{-3} . In addition, solar metallicity model grids have been calculated for densities of 0.01, 0.1, 10, 100, and 1000 cm^{-3} with the same range in v_s and $B/n^{1/2}$. Each model includes components of both the radiative shock and its photoionized precursor, ionized by the extreme ultraviolet (EUV) and soft X-ray radiation generated in the radiative gas.

Since the MAPPING III Library (Allen *et al.*, 2008) only gives the intensity of the corresponding emission line, and CLOUDY itself does not support shocks as the source of the incident radiation field, the simulated continuum spectrum is not available. So we will use line ratios to measure how reasonable the simulation is.

In order to add together the contributions of photoionization and shocks, we followed the method of Jaskot and Ravindranath (2016), for each shock model, they scale the shock emission and add it to the predicted emission of the photoionization model using the following equations:

$$f_{shock} = \frac{H\alpha_{shock} \times s}{H\alpha_{shock} \times s + H\alpha_{photo}} \quad (5.2)$$

$$I_{total} = I_{shock} \times s + I_{photo} \quad (5.3)$$

where f_{shock} is the partial shock contribution, s is the scaling factor applied to the shock emission, and the subscripts "photo" and "shock" denote photoionization and shock emission, respectively. $H\alpha_{shock}$ stands for the intensity of the $H\alpha$ emission line, which has the same unit as I ($\text{erg s}^{-1} \text{ cm}^{-2} \text{ sr}^{-1}$).

5.3.1 General trend

As we did in the Pure photoionization model of the stellar population, we first investigate the general trend of the effect of shocks on line ratios. In Figure 5.3 and Figure 5.4, We show these general trends in the relationship between the parameters of the shock model and the line ratios given by the MAPPING III Library (Allen *et al.*, 2008).

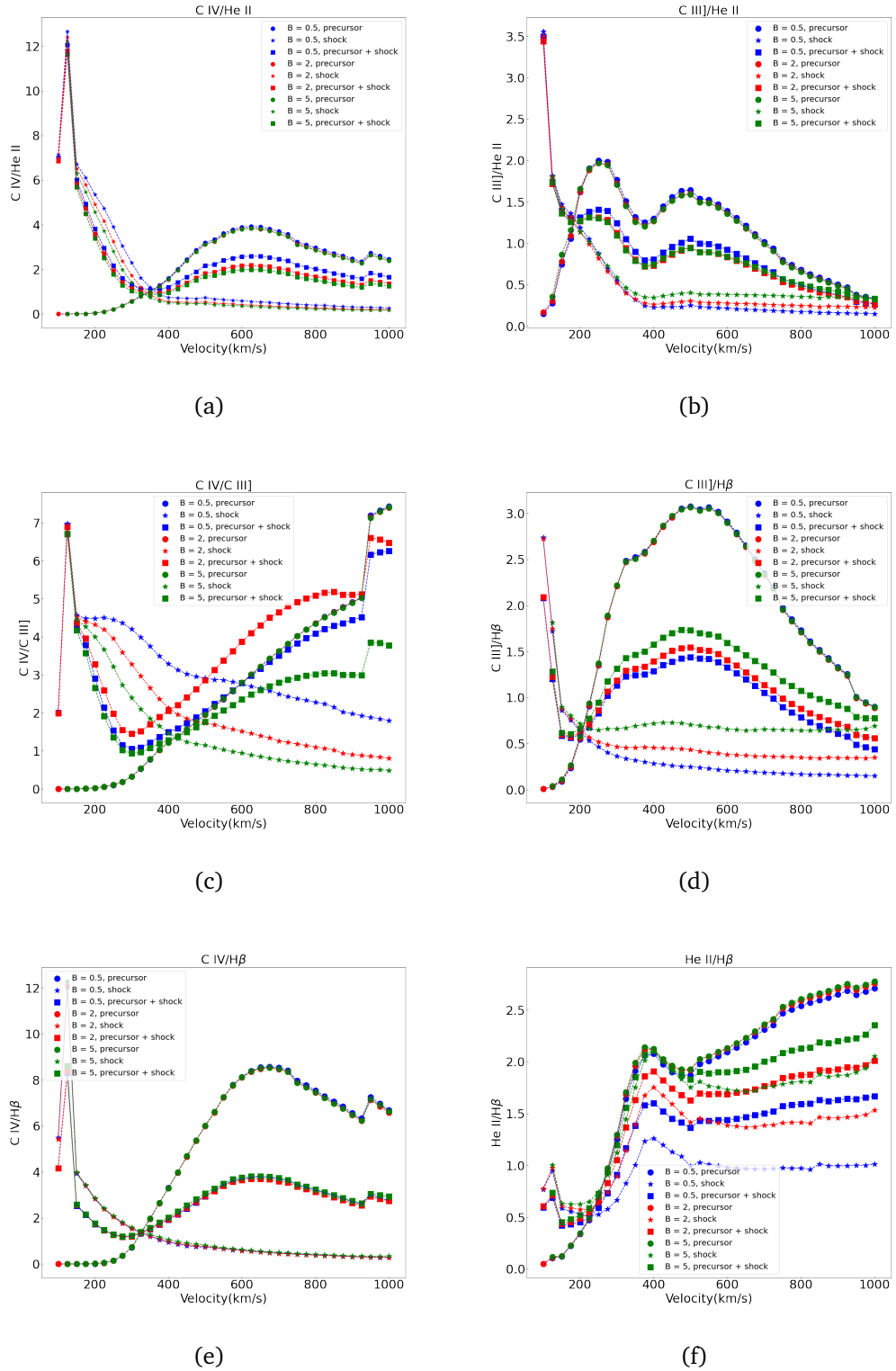


Figure 5.3.: The relationship between the line ratios and velocity of shock, magnetic field strength, and model type

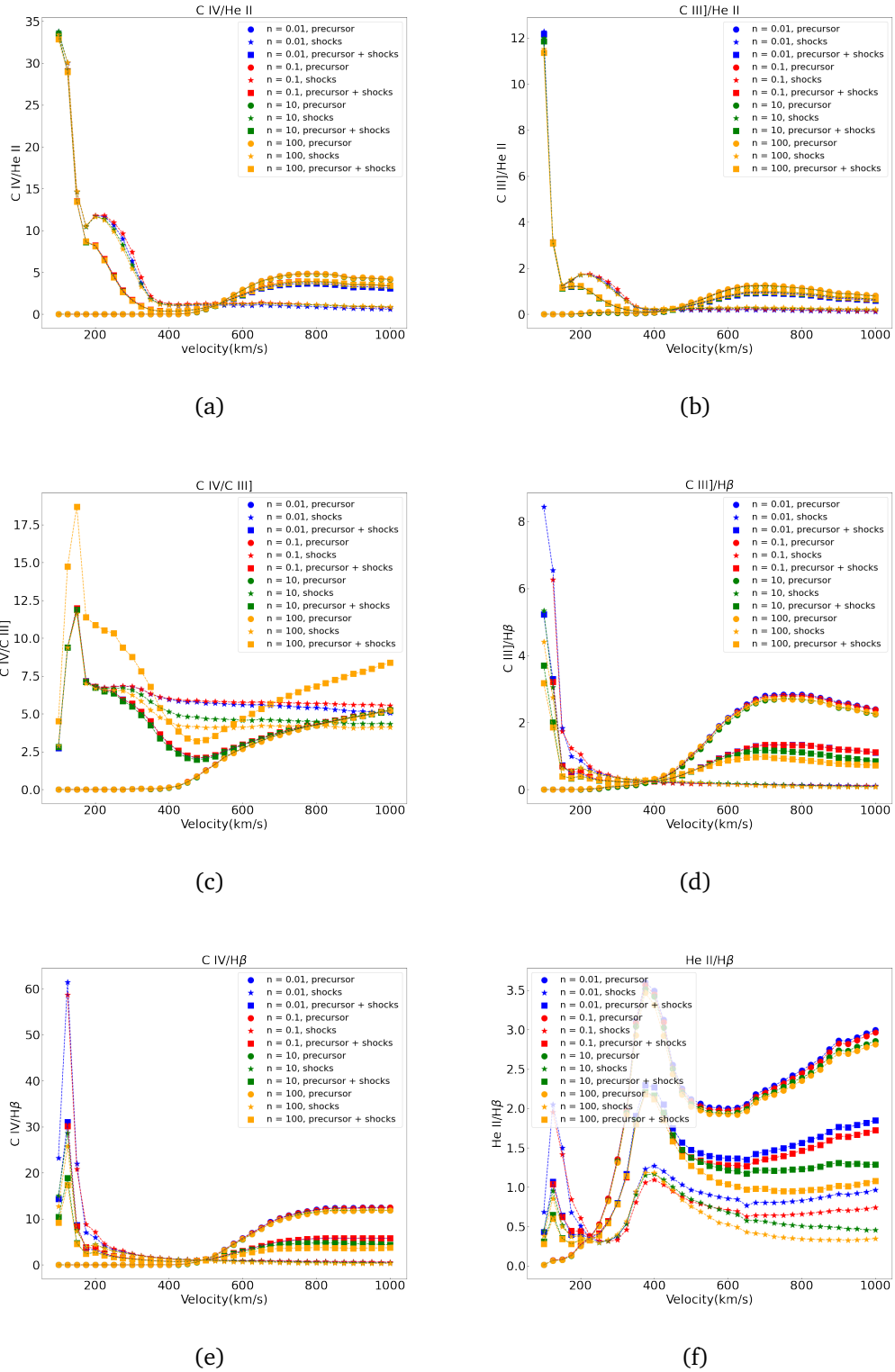


Figure 5.4.: The relationship between the line ratios and velocity of shock, hydrogen density, and model type

In these two figures, we show the relationship between the three line ratios we want to study, the parameters of shocks, and the relationship between the intensity of the three main emission lines relative to $H\beta$ and the parameters of shocks. These parameters include hydrogen density, magnetic parameter, shock velocity, and model type (shock, precursor, precursor + shock). Although we can see from the figure that different parameters will have complex effects on line ratios, we only need to pay attention to one point. That is, both figures clearly show us that as long as the shock model is of the same type, the difference between the magnetic parameter and the hydrogen density will not have a significant impact on the three main line ratios, and the line ratios given by the same type of shock model will only be significantly affected by shock velocity. It is reflected in Figure 5.3 (a), (b), (c) and Figure 5.4 (a), (b), and (c). The lines with the same marker symbol but different colors have the same trend, and they are very close to each other or even overlap. Only a few special cases of C IV/C III] have relatively significant differences.

This conclusion is important for our subsequent evaluation of the simulations since we cannot always guarantee that the best-fit shock model agrees with the relevant properties of the surrounding medium.

In Figure 5.5, we also show the relationship between the line ratios and the metallicity of the shock+ precursor model. In fact, in the subsequent fitting, we will find that all reasonable models are shock+ precursor models. We therefore omit the other two types here.

We found that for C IV/He II and C III]/He II, when the shock velocity $v_s > 200-300 \text{ km s}^{-1}$, the results given by the three different metallicities are not significantly different. For C IV/C III], the LMC metallicity case and the SMC metallicity case are still very similar in most speed ranges. Only the double solar metallicity case has a relatively obvious difference. In fact, since the library only gives the emission of SMC and LMC in the case of $n_H = 1 \text{ cm}^{-3}$, and the solar metallicity data does not include the case of $n_H = 1 \text{ cm}^{-3}$, so we cannot add the solar metallicity case into comparison. Considering that the line ratios of the LMC metallicity case and the SMC metallicity case are very close in most cases, we tend to think that the line ratios of the solar metallicity case will not have much difference compared with LMC and SMC case.

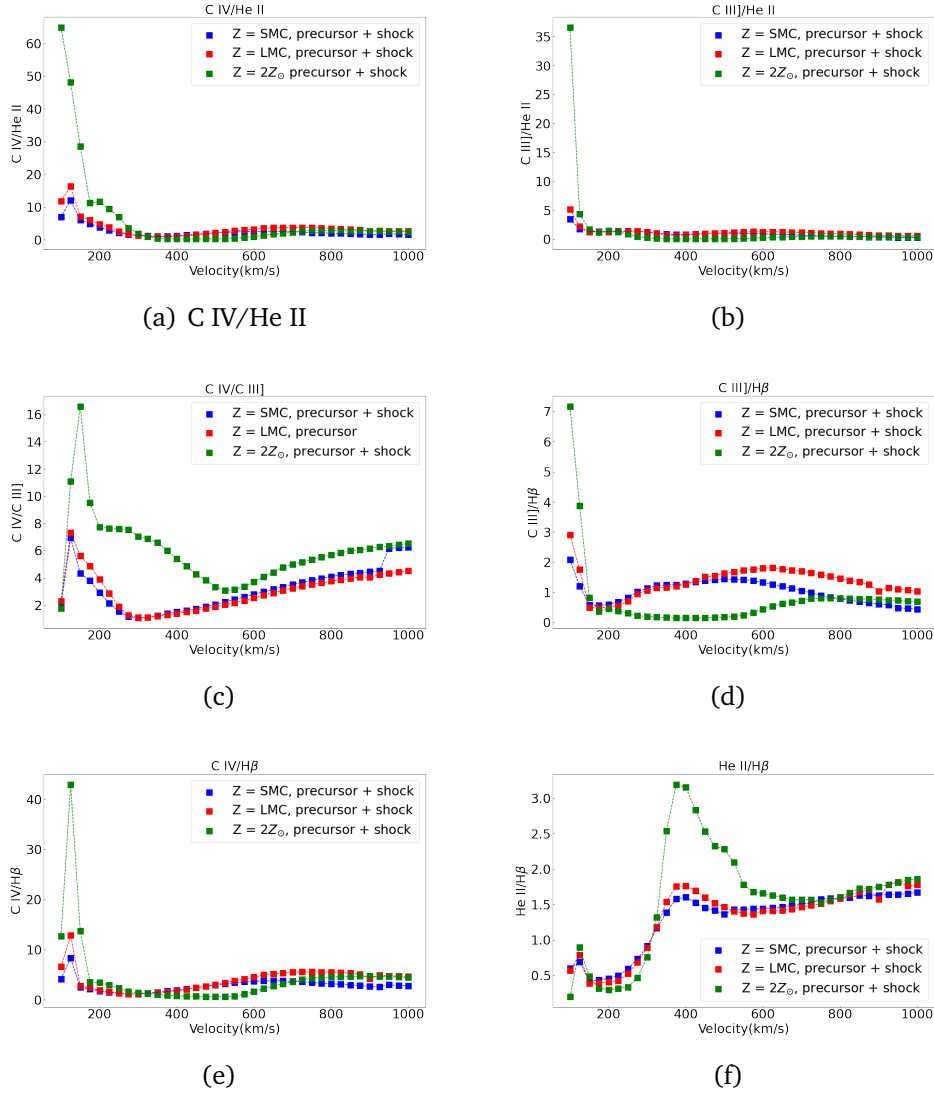


Figure 5.5.: The relationship between the line ratios and the metallicity of shocks

In Figure 5.6, we show line ratios as a function of the percentage contribution of shocks in the incident radiation field. Here we choose the precursor + shocks model with the SMC metallicity, hydrogen density $n = 1 \text{ cm}^{-3}$, and $B = 0.50 \mu G$ and add it to the stellar population photoionization model with the same hydrogen density and similar metallicity ($0.4 Z_{\odot}$).

From the figure, we can see that as the percentage of shocks increases, the three main emission line intensities relative to $H\beta$ in S3 increase monotonically. $C \text{ IV}/\text{He II}$ and $C \text{ IV}/C \text{ III]}$ also increase with the percentage of shocks, but their slopes decrease with the increase of the percentage. Only $C \text{ III]}/\text{He II}$ was negatively correlated with the percentage of shocks.

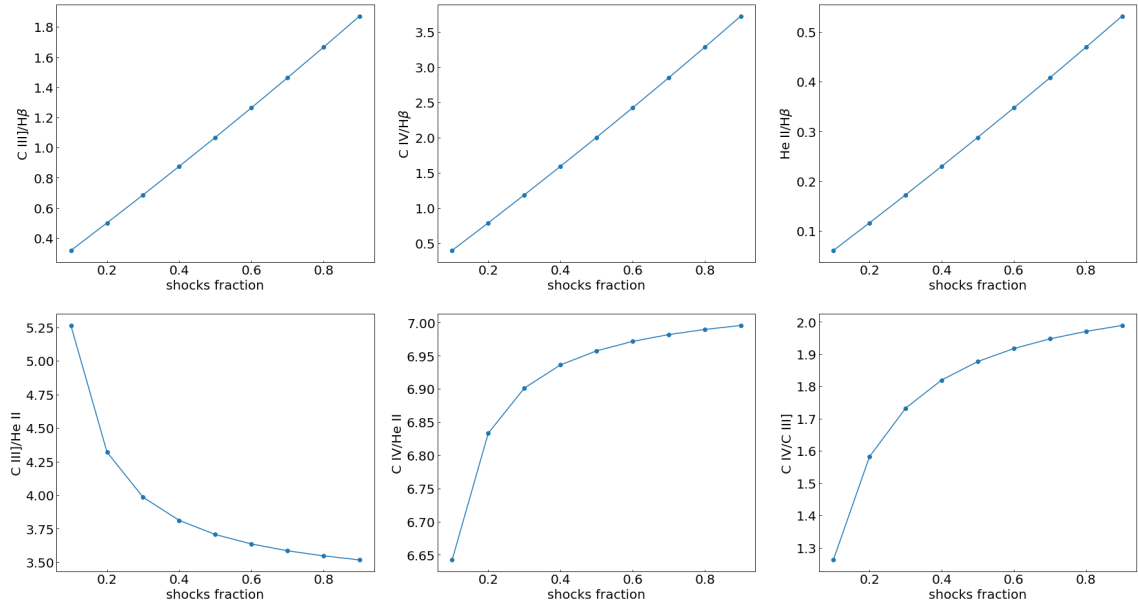


Figure 5.6.: Line ratios as a function of percentage contribution of shocks

5.3.2 Diagnostics

Some research has been done on determining the specific percentage that shocks contribute to the incident radiation field. Jaskot and Ravindranath (2016) give a diagnostic based on C IV]/He II and C III]/He II line ratios. We show this diagnostic method in Figure 5.7.

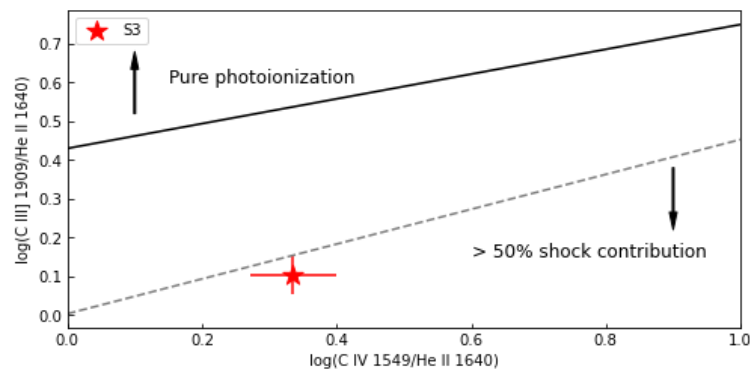


Figure 5.7.: The diagnostic developed by Jaskot and Ravindranath (2016)

If we set $x = \log(\text{C IV } 1549/\text{He II } 1640)$ and $y = \log(\text{C III] } 1909/\text{He II } 1640)$, the equation of the solid line can be written as:

$$y = 0.43 + 0.32x \quad (5.4)$$

The equation of the dashed line can be written as:

$$y = 0.003 + 0.45x \quad (5.5)$$

If this diagnostic is available, it can be seen from the figure that the contribution from shocks in S3 should be around 50%. However, Jaskot and Ravindranath (2016) warn that this diagnostic only covers a single metallicity ($Z \approx 0.003$) and density ($n = 1 \text{ cm}^{-3}$). For higher densities or metallicities other than $Z = 0.003$, the diagnostic may not be reliable.

Some earlier diagnostic methods focused on determining the properties of shocks or the properties of photoionization sources through line ratios. Allen *et al.* (1998) draw UV diagnostic diagrams about pure photoionization and shocks, where the part of shocks comes from the DS96 shock model. We show the diagnostic diagrams of Allen *et al.* (1998) in Figure 5.8 - 5.10.

In these diagnostic diagrams, the blue grid on the left is the diagnostic of the pure photoionization model. The grids give $\alpha = -1$ and the $\alpha = -1.4$ power-law photoionization U sequences where α is the power law of the continuous spectrum, respectively. They are plotted for $n = 100 \text{ cm}^{-3}$ and $n = 1000 \text{ cm}^{-3}$ with grid lines of constant U every 0.25 dex.

The diagnostic grids on the right show the diagnostic of pure shock (the green one) and shock+precursor (the black one). The shock-only grid is plotted in grey and labeled with magnetic parameter $B/\sqrt{n} = 0, 1, 2, 4 \mu\text{G cm}^{3/2}$, and shock velocity $V_{shock} = 150, 200, 300, 500 \text{ km s}^{-1}$. The shock+precursor grids are labelled with $V_{shock} = 200, 300, 500 \text{ km s}^{-1}$, and magnetic parameters where possible. The open circles and solid triangles are observation data of high-redshift galaxies with $z > 1.7$, and the open triangles are some nearby AGNs.

From the six diagnostic diagrams, we can see that S3 falls on neither the grids of the pure photoionization model nor the grids of the shock + precursor. For the pure photoionization model grid, the closest grid point is approximately the position with $n = 1000 \text{ cm}^{-3}$, $\alpha = -1$, $\log U \approx -2.2$ in three diagnostic diagrams. For shocks, S3 is closer to the precursor + shock grids. From these six diagnostic diagrams, neither the pure photoionization model nor the pure shock+precursor model can describe S3 well. This result may prove from

another aspect that the observed spectrum of S3 is the result of the joint influence of photoionization and shock. At the same time, we notice that S3 does fall among the location of other high- z galaxies.

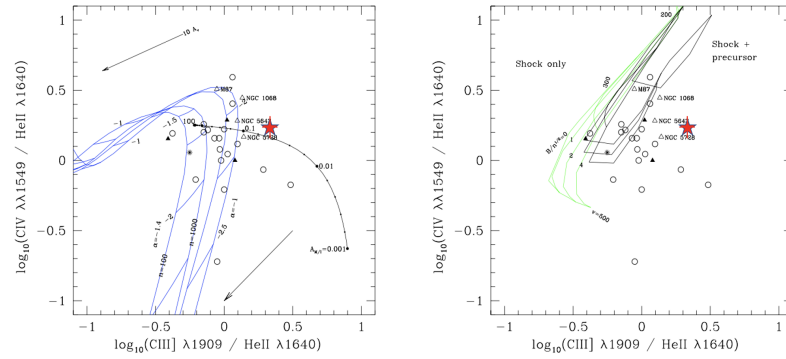


Figure 5.8.: The diagnostic developed by Allen *et al.* (1998), the red star marks the position of S3

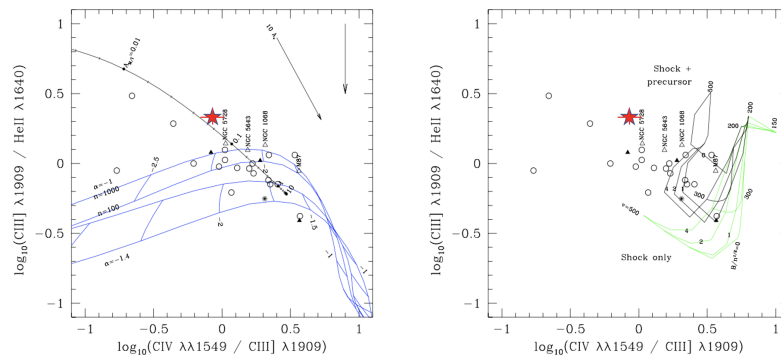


Figure 5.9.: The diagnostic developed by Allen *et al.* (1998), the red star marks the position of S3

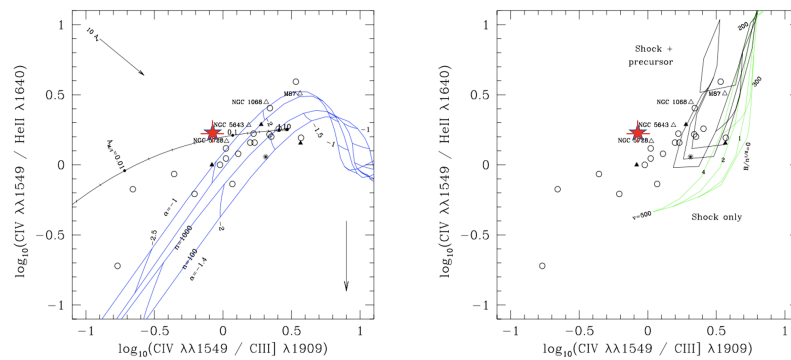


Figure 5.10.: The diagnostic developed by Allen *et al.* (1998), the red star marks the position of S3

5.3.3 Best fit model

Table 5.1.: Line ratio fitting of the stellar population + shock

f_{shock}	best-fit cloud setting	best-fit shock	d_{phase}
0.1	$\log(n_H)=4_{-0.3}Z_{\odot}CN=0.25$	sp_SMC_log(n_H)=0_3.23_800	0.003
0.2	$\log(n_H)=1_{-0.3}Z_{\odot}CN=1$	sp_SMC_log(n_H)=0_1_950	0.002
0.3	$\log(n_H)=2_{-0.3}Z_{\odot}CN=0.65$	sp_ Z_{\odot} _log(n_H)=3_0.01_300	0.001
0.4	$\log(n_H)=2_{-0.3}Z_{\odot}CN=0.65$	sp_ Z_{\odot} _log(n_H)=3_1000_575	0.009
0.5	$\log(n_H)=3_{-0.3}Z_{\odot}CN=0.85$	sp_ Z_{\odot} _log(n_H)=3_1000_575	0.003
0.6	$\log(n_H)=4_{-0.25}Z_{\odot}CN=1$	sp_ Z_{\odot} _log(n_H)=3_1000_575	0.020
0.7	$\log(n_H)=4_{-0.25}Z_{\odot}CN=1$	sp_SMC_log(n_H)=0_10_250	0.012
0.8	$\log(n_H)=4_{-0.25}Z_{\odot}CN=1$	sp_ Z_{\odot} _log(n_H)=3_1000_575	0.254
0.9	$\log(n_H)=2_{-Z_{\odot}}CN=0.05$	s_ Z_{\odot} _log(n_H)=-1_10_1000	0.294

In this section, according to the method given by equation (5.1) and equation (5.2), we set the percentage of shocks contribution in incident radiation from 10% to 90%, with a step size of 10%. As mentioned before, we use three line ratios to construct the 3D phase space and use the phase distance between simulated and observed data to measure the quality of the model. Here the phase distance d_{phase} can be expressed as:

$$d_{phase} = \sqrt{\left(\frac{CIV}{HeII}_{sim} - \frac{CIV}{HeII}_{obs}\right)^2 + \left(\frac{CIII}{HeII}_{sim} - \frac{CIII}{HeII}_{obs}\right)^2 + \left(\frac{CIV}{CIII}_{sim} - \frac{CIV}{CIII}_{obs}\right)^2} \quad (5.6)$$

The subscript "sim" stands for simulation, and "obs" stands for observation.

We show the fitting results in Table 5.1, and in Table 5.2, we show the values of the best-fit line ratios.

The cloud setting item in Table 5.1 gives the log value of the hydrogen density corresponding to the model, the metallicity, and the scale factor of C/O and N/O. The best-fit shock item gives the type of the shock model (pure shock: s, pure precursor: p, shock+precursor: sp), metallicity (SMC, LMC, Z_{\odot}), the log value of the hydrogen density, the magnetic field strength B (in the unit of μG) and the velocity of the shocks (in the unit of km s^{-1}) in turn. d_{phase} is the distance to the position of S3 in the 3D phase space.

Table 5.2.: Best-fit line ratios of the stellar population + shock

f_{shock}	C IV/He II	C III]/He II	C IV/C III]
S3	1.740	2.095	0.831
0.1	1.739	2.097	0.829
0.2	1.740	2.097	0.830
0.3	1.740	2.095	0.831
0.4	1.737	2.087	0.832
0.5	1.738	2.094	0.830
0.6	1.747	2.113	0.827
0.7	1.732	2.086	0.831
0.8	1.727	1.861	0.928
0.9	1.496	2.175	0.688

Through Table 5.1 and Table 5.2, we found that, except for the cases of $f_{shock} = 0.8$ and 0.9 , where the line ratios are significantly different from the observed results, the other cases have given simulation results that can well reproduce the S3 line ratios. However, the metallicity and hydrogen density of all these shock models cannot be exactly matched with the corresponding cloud models. All reasonable results give low cloud metallicities of 0.25 or 0.3 and precursor+shock models. The hydrogen density and metallicity of the cloud and shock of the $f_{shock} = 0.2$ case are the closest. At the same time, the shock model $sp_Z_{\odot}_log(n_H)=3_1000_575$ appears three times in the case of $f_{shock} = 0.4 - 0.6$. All three cases give relatively high hydrogen densities, but the metallicities of clouds and shocks cannot match. In fact, even when we expanded the selection to the top 10 best combinations for each case, we still failed to find a combination that both metallicity and hydrogen density fit perfectly. However, considering that we have previously found that hydrogen density, magnetic factor, and metallicity have only a very limited impact on the line ratios of the same type of model, it is debatable to exclude possible fitting results only on the grounds of mismatched hydrogen density or metallicity.

We finally concluded that adding the contribution of shocks to the incident radiation fields can indeed produce line ratios that are very close to the observed data. However, it is very difficult to find the most reasonable model. From the perspective of the best match of cloud and shock model parameters, the $f_{shock} = 0.2$ case is the most likely. However, cases with $f_{shock} = 0.4 - 0.6$ are also very likely if combined with the diagnostics we used earlier (albeit imprecise) and the number of occurrences of the same shock model.

However, limited by the limited model provided by the MAPPING III Library (Allen *et al.*, 2008), the accuracy of the simulation and the lack of continuum spectrum, and considering that the influence of different parameters on the line ratios is indeed limited, it is indeed difficult for us to give an optimal simulation, at the same time, we are not sure whether the co-action of shock with stellar population photoionization would allow the continuum of the simulated spectra to match the observations.

5.4 AGNs

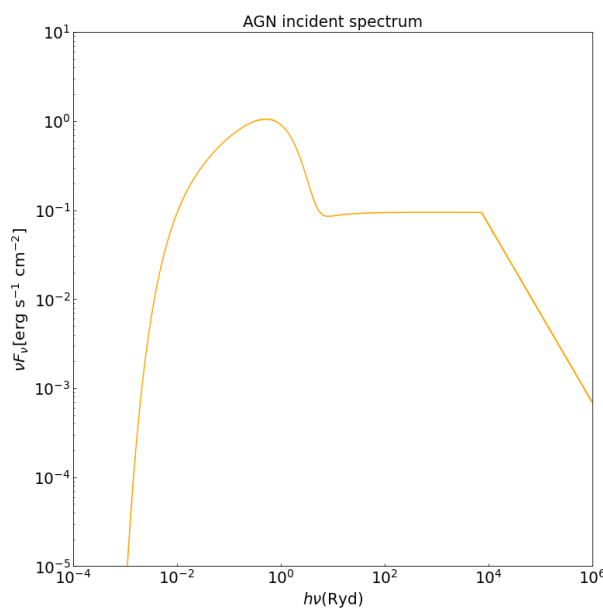


Figure 5.11.: AGN incident spectrum

We also considered the possibility of AGN contributing to incident radiation field.

In fact, we did not find any features that can absolutely confirm the existence of AGN from the spectrum. For example, He II 1640, which may have the AGN contribution, may also have contributions from other sources. As a result, we cannot obtain any information related to the properties of AGN that may exist. Therefore we used the default AGN incident spectrum settings provided in CLOUDY, That is, $T = 1.5 \times 10^5$ K, the X-ray to UV ratio $\alpha_{ox} = -1.4$, which is thought to be the typical value of AGN (Zamorani *et al.* 1981), the low-energy slope of the Big Bump continuum is $\alpha_{UV} = -0.5$, and the default value of the

slope of the X-ray component is $\alpha_x = -1$. In Figure 5.11, we show the incident spectrum of AGN.

As we did in the previous section, we first try a photoionization model of the stellar population + AGN combination. We adopted the same cloud parameter interval settings as pure photoionization for the stellar population. According to the method of equations (5.1) and (5.2), we set the contribution of AGN in the incident radiation field from 10% to 90% and set the step size to 10%. Since CLOUDY supports setting AGN as an incident radiation field, the corresponding continuum spectrum is available. Therefore, we still use reduced chi-square fit and line ratios fitting to evaluate our simulation quality, respectively.

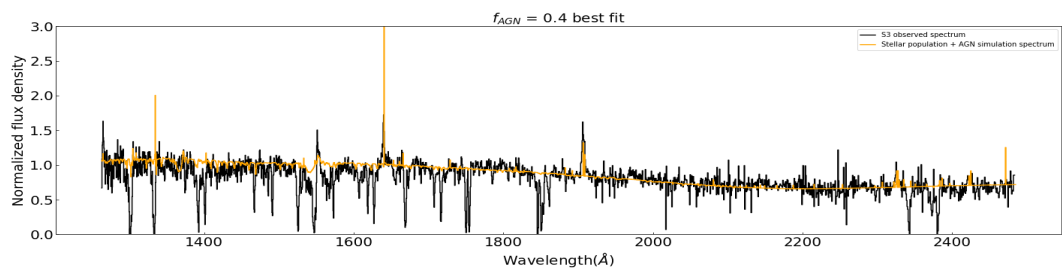
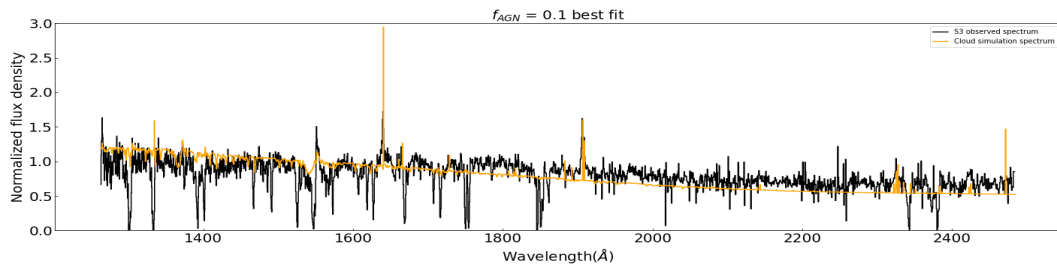
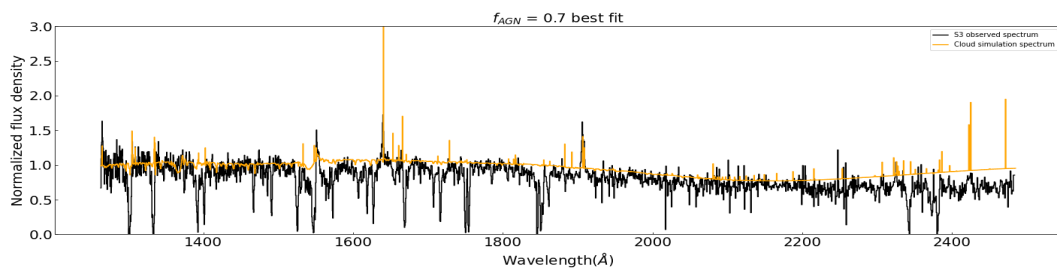


Figure 5.12.: AGN simulation spectrum



(a) $f_{AGN} = 0.1$ case



(b) $f_{AGN} = 0.7$ case

Figure 5.13.: AGN simulation spectrum for comparison

The best fitting result appears in the case of $f_{AGN} = 0.4$. We got a model with hydrogen density $n_H = 10 \text{ cm}^{-3}$, metallicity $Z = Z_\odot$ and C/O, N/O scale factor = 0.15. The reduced chi square is $\chi_{red}^2 = 3.332$. In Figure 5.12, we show the simulation spectrum compared with the observation data.

In Figure 5.12, We found that the pure photoionization spectrum of the stellar population can be flattened by adding AGN. As f_{AGN} increase, we find an obvious trend. That is, the larger the contribution of AGN in the incident radiation, the redder the spectrum. I think this is due to the fact that CLOUDY's default AGN setup is closer to the case of the Seyfert 2 galaxies, whose continuum tends to be redder. We show the best fit cases of $f_{AGN} = 0.1$ and $f_{AGN} = 0.7$ in Figure 5.13 for comparison. For the two cases of $f_{AGN} = 0.1$ and 0.7 , their χ^2 are 5.144 and 5.306, respectively.

Although AGN contribution can flatten the spectrum, such simulations also have serious problems. The most obvious problem is that the emission intensity of the He II emission line caused by AGN is larger than the observation results. Even though our model does not include athermal broadening, even in the case of $f_{AGN}=0.1$, the intensity of He II 1640 is still around 1.4 times larger than the observed value. At the same time, the performance given by line ratio fitting is also very bad. Therefore, we think the stellar population + AGN photoionization model cannot reproduce the observations well.

5.5 shock + AGN

Table 5.3.: Line ratio fitting of the stellar population + AGN + shock

f_{shock}	best-fit cloud setting	best-fit shock	d_{phase}
0.1	$\log(n_H)=3_{-0.5}Z_\odot_{-CN}=0.65$	$s_{Z_\odot}\log(n_H)=3_{-1000}_{-225}$	0.001
0.2	$\log(n_H)=4_{-0.4}Z_\odot_{-CN}=1$	$sp_{Z_\odot}\log(n_H)=-2_{-0.2}_{-975}$	0.001
0.3	$\log(n_H)=4_{-0.3}Z_\odot_{-CN}=1$	$sp_{Z_\odot}\log(n_H)=1_{-40}_{-1000}$	0.005
0.4	$\log(n_H)=2_{-0.3}Z_\odot_{-CN}=0.85$	$sp_{Z_\odot}\log(n_H)=3_{-1000}_{-300}$	0.004
0.5	$\log(n_H)=4_{-0.3}Z_\odot_{-CN}=1$	$sp_{Z_\odot}\log(n_H)=-1_{-10}_{-275}$	0.007
0.6	$\log(n_H)=3_{-0.25}Z_\odot_{-CN}=0.65$	$sp_{Z_\odot}\log(n_H)=0_{-10^{-4}}_{-275}$	0.013
0.7	$\log(n_H)=4_{-0.25}Z_\odot_{-CN}=1$	$sp_{SMC}\log(n_H)=0_{-4}_{-250}$	0.063
0.8	$\log(n_H)=4_{-0.25}Z_\odot_{-CN}=1$	$sp_{SMC}\log(n_H)=0_{-10^{-4}}_{-575}$	0.216
0.9	$\log(n_H)=1_{-Z_\odot}_{-CN}=0.05$	$s_{Z_\odot}\log(n_H)=1_{-100}_{-1000}$	0.293

Table 5.4.: Best-fit line ratios of stellar population + AGN + shock

f_{shock}	C IV/He II	C III]/He II	C IV/C III]
S3	1.740	2.095	0.831
0.1	1.742	2.095	0.831
0.2	1.741	2.094	0.831
0.3	1.736	2.092	0.830
0.4	1.737	2.093	0.830
0.5	1.746	2.092	0.835
0.6	1.732	2.102	0.824
0.7	1.746	2.038	0.857
0.8	1.927	2.064	0.934
0.9	1.531	2.239	0.684

We also used the line ratio fitting method to combine the photoionization model of stellar population + AGN with different percentages of shock contribution. For the contribution of AGN, we used the best-fit case of $f_{shock} = 0.4$, and the rest of the steps were the same as we did when dealing with the combination of shocks and stellar population photoionization models. In Table 5.3 and Table 5.4, we show the best-fit results we obtained.

As in the case of stellar population + shock simulations, we found that $f_{shock} = 0.1 - 0.6$ cases can provide a fairly good approximation. And the lower the contribution of shock, the closer the prediction given by the best-fit model will be. However, metallicity and hydrogen density are still not well matched.

In fact, from another point of view, the contribution of AGN has already caused too strong He II emission, and we have found in Figure 5.6 that adding shock to the photoionization model will only further increase the He II emission. So although we can get very close line ratios, this model is still unlikely to be the real situation in S3. This result also shows that only relying on line ratios to measure the quality of the model may not be reliable enough.

Summary

In this section, we give a brief summary of our project. In this project, we first extract the UV spectrum of 5 different lensed objects in CSWA31 from the MUSE datacube. Using the observable emission lines, we remeasure their redshifts, then summarize the properties of their absorption and emission lines. Through the unsaturated absorption lines, we measure the column densities of some elements of them. Among them, S0 and S3 have the highest signal-to-noise ratio. Both their absorption lines show a pronounced blue shift relative to the redshifts given by emission lines, implying the presence of outflows in both galaxies. Fe II* fine-structured emission lines were found in S0, and they are very likely to originate from resonant scattering in the outflow. We confirmed the spatial extension of the narrow-band image of these emission lines, which is another evidence for the existence of the outflow.

Next, we focus on S3 with the most abundant absorption and emission features. We found He II 1640, C III] 1906, 1909 and C IV 1548, 1550 emissions in the UV spectrum of S3. They all have many different possible origins, such as stellar winds or nebulae. We used methods such as emission line ratios and UV spectrum indices to roughly estimate the stellar mass, metallicity, and star formation rate of S3 and verified the results using BAGPIPES. We finally got that the stellar mass of S3 is around 10^9 , the value of the metallicity of stellar population is about 0.2 - 0.3 Z_{\odot} , and the star formation rate is between 1.5 - 4.5 $M_{\odot} \text{ yr}^{-1}$. The ionization parameter is about $\log(U) = -2.14$, and the value of $\log(\text{sSFR})$ is between -8 and -9. According to these properties, we think S3 is a dwarf galaxy without any starburst phenomenon. We use BPASS to fit the C IV 1548, 1550 profile to find the most likely stellar population model of S3 via reduced chi-square fitting. The best-fit model corresponds to a young stellar population model with $Z = 0.2Z_{\odot}$ and $\log(\text{Age}/\text{yrs}) = 6.1$.

Next, based on the best-fit stellar population model given by BPASS, we use CLOUDY to simulate the spectrum of S3. For the models available for the continuum spectrum in the simulation results, we use reduced chi-square

fitting for the continuum spectrum and the line ratios fitting to measure the quality of the model. For the model settings, we set 9 different metallicity options ($0.25 Z_{\odot}$, $0.3 Z_{\odot}$, $0.4 Z_{\odot}$, $0.5 Z_{\odot}$, $0.6 Z_{\odot}$, $0.7 Z_{\odot}$, $0.8 Z_{\odot}$, $0.9 Z_{\odot}$, $1.0 Z_{\odot}$) and scale the default C/O and N/O ratios from the CLOUDY ISM abundance set by factors of 0.05, 0.15, 0.25, 0.45, 0.65, 0.85, and 1. We use the default ISM dust settings provided by CLOUDY, and the hydrogen density of the model has 5 different options: 1 cm^{-3} , 10 cm^{-3} , 100 cm^{-3} , 1000 cm^{-3} , and 10000 cm^{-3} . We use the open geometry, which means all radiation that escapes from the illuminated face of the cloud, towards the source of continuous radiation, then escapes from the system without further interaction with gas.

Through simulation, we found that the pure stellar population photoionization model cannot reproduce the spectrum and line ratios, and the appearance of the AGN component will make the He II emission too strong.

The stellar population + shock model with lower gas metallicity is the most likely option, the existing diagnostic based on line ratios also supports this possibility, but we cannot be 100% sure due to the absence of simulated continuum spectra.

There is also much room for further improvement in this research. First, due to the absence of the rest-frame optical band spectra, we cannot directly infer the properties of these galaxies, such as metallicity, hydrogen density, and electron temperature. The absence of O III] 1661, 1666 also made the efforts to use UV diagnostic fail. Second, our model is still very simple, and the simulation of the stellar population does not include the consideration of the continuous star formation. Meanwhile, the athermal broadening is not included in the CLOUDY model. More importantly, the spectrum of a galaxy is often the result of multiple different stellar populations and their nearby interstellar medium, which cannot be well described by our model. In future work, if the high signal-to-noise ratio spectrum in the optical band of the system can be well observed, then we can study the properties of these galaxies more deeply and precisely. At the same time, we also think the possibility of introducing deep learning methods into simulations to find the best-fit parameters of the model. If the 3-D phase space distance or reduced chi-square can be used as the criterion for the feedback mechanism, then we may be able to let the computer automatically find the best fitting parameters of the model.

- Allen, Mark G, Michael A Dopita, and Zlatan I Tsvetanov (1998). „Ultraviolet diagnostics for the emission-line gas in active galaxies“. In: *The Astrophysical Journal* 493.2, p. 571.
- Allen, Mark G, Brent A Groves, Michael A Dopita, Ralph S Sutherland, and Lisa J Kewley (2008). „The MAPPINGS III library of fast radiative shock models“. In: *The Astrophysical Journal Supplement Series* 178.1, p. 20.
- Baldwin, Jack A, Mark M Phillips, and Roberto Terlevich (1981). „Classification parameters for the emission-line spectra of extragalactic objects.“ In: *Publications of the Astronomical Society of the Pacific* 93.551, p. 5.
- Bayliss, Matthew B, Jane R Rigby, Keren Sharon, Eva Wuyts, Michael Florian, Michael D Gladders, Traci Johnson, and Masamune Oguri (2014). „The physical conditions, metallicity and metal abundance ratios in a highly magnified galaxy at $z = 3.6252$ “. In: *The Astrophysical Journal* 790.2, p. 144.
- Belokurov, V, NW Evans, PC Hewett, A Moiseev, RG McMahon, SF Sanchez, and LJ King (2009). „Two new large-separation gravitational lenses from SDSS“. In: *Monthly Notices of the Royal Astronomical Society* 392.1, pp. 104–112.
- Berg, Danielle A, Dawn K Erb, Matthew W Auger, Max Pettini, and Gabriel B Brammer (2018). „A window on the earliest star formation: extreme photoionization conditions of a high-ionization, low-metallicity lensed galaxy at $z \sim 2$ “. In: *The Astrophysical Journal* 859.2, p. 164.
- Brewer, Brendon J, Geraint F Lewis, Vasily Belokurov, Michael J Irwin, Terry J Bridges, and N Wyn Evans (2011). „Modelling of the complex CAS-SOWARY/SLUGS gravitational lenses“. In: *Monthly Notices of the Royal Astronomical Society* 412.4, pp. 2521–2529.
- Byler, Nell, Lisa J Kewley, Jane R Rigby, Ayan Acharyya, Danielle A Berg, Matthew Bayliss, and Keren Sharon (2020). „A comparison of UV and optical metallicities in star-forming galaxies“. In: *The Astrophysical Journal* 893.1, p. 1.

- Calzetti, Daniela, Lee Armus, Ralph C Bohlin, Anne L Kinney, Jan Koornneef, and Thaisa Storchi-Bergmann (2000). „The dust content and opacity of actively star-forming galaxies“. In: *The Astrophysical Journal* 533.2, p. 682.
- Cimatti, A., P. Cassata, L. Pozzetti, *et al.* (Apr. 2008). „GMSS ultradeep spectroscopy of galaxies at $z \sim 2$. II. Superdense passive galaxies: how did they form and evolve?“ In: 482.1, pp. 21–42. arXiv: 0801.1184 [astro-ph].
- Coil, Alison L, Benjamin J Weiner, Daniel E Holz, Michael C Cooper, Renbin Yan, and James Aird (2011). „Outflowing Galactic Winds in Post-starburst and Active Galactic Nucleus Host Galaxies at $0.2 < z < 0.8$ “. In: *The Astrophysical Journal* 743.1, p. 46.
- Condon, JJ (1992). „Radio emission from normal galaxies“. In: *Annual review of astronomy and astrophysics* 30.1, pp. 575–611.
- Denicoló, Glenda, Roberto Terlevich, and Elena Terlevich (2002). „New light on the search for low-metallicity galaxies—I. The N2 calibrator“. In: *Monthly Notices of the Royal Astronomical Society* 330.1, pp. 69–74.
- Eldridge, JJ, ER Stanway, LLAS Xiao, LAS McClelland, G Taylor, M Ng, SML Greis, and JC Bray (2017). „Binary population and spectral synthesis version 2.1: construction, observational verification, and new results“. In: *Publications of the Astronomical Society of Australia* 34, e058.
- Erb, Dawn K, Max Pettini, Alice E Shapley, Charles C Steidel, David R Law, and Naveen A Reddy (2010). „Physical conditions in a young, unreddened, low-metallicity galaxy at high redshift“. In: *The Astrophysical Journal* 719.2, p. 1168.
- Erb, Dawn K, Anna M Quider, Alaina L Henry, and Crystal L Martin (2012). „Galactic outflows in absorption and emission: Near-ultraviolet spectroscopy of galaxies at $1 < z < 2$ “. In: *The Astrophysical Journal* 759.1, p. 26.
- Ferland, GJ, M Chatzikos, F Guzmán, ML Lykins, PAM Van Hoof, RJR Williams, NP Abel, NR Badnell, FP Keenan, RL Porter, *et al.* (2017). „The 2017 release of Cloudy“. In: *Revista mexicana de astronomia y astrofisica* 53.2.
- Grillo, Claudio, L Christensen, A Gallazzi, and Jesper Rasmussen (2013). „Measuring the total and baryonic mass profiles of the very massive CASSOWARY 31 strong lens. A fossil system at $z = 0.7$?“ In: *Monthly Notices of the Royal Astronomical Society* 433.3, pp. 2604–2612.
- Hainline, Kevin N, Alice E Shapley, Katherine A Kornei, Max Pettini, Elizabeth Buckley-Geer, Sahar S Allam, and Douglas L Tucker (2009). „Rest-Frame optical spectra of three strongly lensed galaxies at $z \sim 2$ “. In: *The Astrophysical Journal* 701.1, p. 52.

- Heckman, Timothy M., Carmelle Robert, Claus Leitherer, Donald R. Garnett, and Fabienne van der Rydt (Aug. 1998). „The Ultraviolet Spectroscopic Properties of Local Starbursts: Implications at High Redshift“. In: 503.2, pp. 646–661. arXiv: astro-ph/9803185 [astro-ph].
- Huang, Rongjun, Andrew J Battisti, Kathryn Grasha, Elisabete da Cunha, Claudia del P Lagos, Sarah K Leslie, and Emily Wisnioski (2023). „Exploring the intrinsic scatter of the star-forming galaxy main sequence at redshift 0.5 to 3.0“. In: *Monthly Notices of the Royal Astronomical Society* 520.1, pp. 446–460.
- Jaskot, AE and Swara Ravindranath (2016). „Photoionization models for the semi-forbidden C III] 1909 emission in star-forming galaxies“. In: *The Astrophysical Journal* 833.2, p. 136.
- Kennicutt Jr, Robert C (1998). „Star formation in galaxies along the Hubble sequence“. In: *Annual Review of Astronomy and Astrophysics* 36.1, pp. 189–231.
- Kerutt, J, L Wisotzki, A Verhamme, KB Schmidt, F Leclercq, EC Herenz, T Urrutia, T Garel, T Hashimoto, M Maseda, *et al.* (2022). „Equivalent widths of Lyman α emitters in MUSE-Wide and MUSE-Deep“. In: *Astronomy & Astrophysics* 659, A183.
- Kinney, A. L., R. C. Bohlin, D. Calzetti, N. Panagia, and Rosemary F. G. Wyse (May 1993a). „An Atlas of Ultraviolet Spectra of Star-forming Galaxies“. In: 86, p. 5.
- Kinney, AL, RC Bohlin, D Calzetti, N Panagia, and Rosemary FG Wyse (1993b). „An atlas of ultraviolet spectra of star-forming galaxies“. In: *Astrophysical Journal Supplement Series (ISSN 0067-0049)*, vol. 86, no. 1, p. 5-93. 86, pp. 5–93.
- Kornei, Katherine A, Alice E Shapley, Crystal L Martin, Alison L Coil, Jennifer M Lotz, and Benjamin J Weiner (2013). „Fine-structure Fe II* emission and resonant Mg II emission in $z \sim 1$ star-forming galaxies“. In: *The Astrophysical Journal* 774.1, p. 50.
- Kroupa, Pavel, Christopher A Tout, and Gerard Gilmore (1993). „The distribution of low-mass stars in the Galactic disc“. In: *Monthly Notices of the Royal Astronomical Society* 262.3, pp. 545–587.
- Leitherer, Claus, Carmelle Robert, and Timothy M Heckman (1995). „Atlas of Synthetic Ultraviolet Spectra of Massive Star Populations“. In: *The Astrophysical Journal Supplement Series* 99, p. 173.

- Lilly, S. J., O. Le Fèvre, A. Renzini, *et al.* (Sept. 2007). „zCOSMOS: A Large VLT/VIMOS Redshift Survey Covering $0 < z < 3$ in the COSMOS Field“. In: *The Astrophysical Journal Supplement Series* 172.1, p. 70.
- Lise, Christensen, Peter Laursen, Johan Richard, Jens Hjorth, Bo Milvang-Jensen, Miroslava Dessauges-Zavadsky, Marceau Limousin, Claudio Grillo, and Harald Ebeling (2012). „Gravitationally lensed galaxies at $2 < z < 3.5$: direct abundance measurements of Ly α emitters“. In: *Monthly Notices of the Royal Astronomical Society* 427.3, pp. 1973–1982.
- Maeder, André and Peter S Conti (1994). „Massive star populations in nearby galaxies“. In: *Annual Review of Astronomy and Astrophysics* 32.1, pp. 227–275.
- Meurer, Gerhardt R, Timothy M Heckman, and Daniela Calzetti (1999). „Dust absorption and the ultraviolet luminosity density at $z \approx 3$ as calibrated by local starburst galaxies“. In: *The Astrophysical Journal* 521.1, p. 64.
- Olivier, Grace M, Danielle A Berg, John Chisholm, Dawn K Erb, Richard W Pogge, and Evan D Skillman (2022). „Characterizing Extreme Emission Line Galaxies. II. A Self-consistent Model of Their Ionizing Spectrum“. In: *The Astrophysical Journal* 938.1, p. 16.
- Pagel, BEJ, MG Edmunds, DE Blackwell, MS Chun, and GI Smith (1979). „On the composition of H II regions in southern galaxies–I. NGC 300 and 1365“. In: *Monthly Notices of the Royal Astronomical Society* 189.1, pp. 95–113.
- Pannella, Maurilio, CL Carilli, Emanuele Daddi, HJ McCracken, FN Owen, A Renzini, V Strazzullo, F Civano, AM Koekemoer, E Schinnerer, *et al.* (2009). „Star formation and dust obscuration at $z \approx 2$: galaxies at the dawn of downsizing“. In: *The Astrophysical Journal* 698.2, p. L116.
- Pérez-Montero, Enrique and Ricardo Amorín (2017). „Using photoionization models to derive carbon and oxygen gas-phase abundances in the rest UV“. In: *Monthly Notices of the Royal Astronomical Society* 467.2, pp. 1287–1293.
- Pettini, M., S. L. Ellison, J. Bergeron, and P. Petitjean (Aug. 2002). „The abundances of nitrogen and oxygen in damped Lyman alpha systems“. In: 391, pp. 21–34. arXiv: astro-ph/0205472 [astro-ph].
- Pettini, Max, Samantha A. Rix, Charles C. Steidel, Kurt L. Adelberger, Matthew P. Hunt, and Alice E. Shapley (Apr. 2002). „New Observations of the Interstellar Medium in the Lyman Break Galaxy MS 1512-cB58“. In: *The Astrophysical Journal* 569.2, p. 742.
- Prochaska, J Xavier, Daniel Kasen, and Kate Rubin (2011). „Simple models of metal-line absorption and emission from cool gas outflows“. In: *The Astrophysical Journal* 734.1, p. 24.

- Quider, Anna M, Max Pettini, Alice E Shapley, and Charles C Steidel (2009). „The ultraviolet spectrum of the gravitationally lensed galaxy ‘the Cosmic Horseshoe’: a close-up of a star-forming galaxy at $z \sim 2$ “. In: *Monthly Notices of the Royal Astronomical Society* 398.3, pp. 1263–1278.
- Raimann, D, Thaisa Storchi-Bergmann, E Bica, Jorge Melnick, and H Schmitt (2000). „Gas properties of H ii and starburst galaxies: relation with the stellar population“. In: *Monthly Notices of the Royal Astronomical Society* 316.3, pp. 559–568.
- Rigby, J. R., M. B. Bayliss, J. Chisholm, *et al.* (Jan. 2018). „The Magellan Evolution of Galaxies Spectroscopic and Ultraviolet Reference Atlas (MegaSaura). II. Stacked Spectra“. In: *The Astrophysical Journal* 853.1, p. 87.
- Rubin, Kate HR, J Xavier Prochaska, David C Koo, Andrew C Phillips, and Benjamin J Weiner (2010). „GALAXIES PROBING GALAXIES: COOL HALO GAS FROM A $z = 0.47$ POST-STARBURST GALAXY“. In: *The Astrophysical Journal* 712.1, p. 574.
- Schlafly, Edward F and Douglas P Finkbeiner (2011). „Measuring reddening with Sloan Digital Sky Survey stellar spectra and recalibrating SFD“. In: *The Astrophysical Journal* 737.2, p. 103.
- Shapley, Alice E., Charles C. Steidel, Max Pettini, and Kurt L. Adelberger (May 2003). „Rest-Frame Ultraviolet Spectra of $z \sim 3$ Lyman Break Galaxies*“. In: *The Astrophysical Journal* 588.1, p. 65.
- Shull, J Michael and Christopher F McKee (1979). „Theoretical models of interstellar shocks. I-Radiative transfer and UV precursors“. In: *The Astrophysical Journal* 227, pp. 131–149.
- Spitzer, Lyman (1978). „Review of publications: Physical processes in the interstellar medium“. In: *Journal of the Royal Astronomical Society of Canada, Vol. 72, p. 349* 72, p. 349.
- Stanway, Elizabeth R, JJ Eldridge, and George D Becker (2016). „Stellar population effects on the inferred photon density at reionization“. In: *Monthly Notices of the Royal Astronomical Society* 456.1, pp. 485–499.
- Stark, Daniel P, Matthew Auger, Vasily Belokurov, Tucker Jones, Brant Robertson, Richard S Ellis, David J Sand, Alexei Moiseev, Will Eagle, and Thomas Myers (2013). „The CASSOWARY spectroscopy survey: a new sample of gravitationally lensed galaxies in SDSS“. In: *Monthly Notices of the Royal Astronomical Society* 436.2, pp. 1040–1056.
- Steidel, Charles C., Kurt L. Adelberger, Alice E. Shapley, Max Pettini, Mark Dickinson, and Mauro Giavalisco (Aug. 2003). „Lyman Break Galaxies at

- Redshift $z \sim 3$: Survey Description and Full Data Set“. In: *The Astrophysical Journal* 592.2, p. 728.
- Steidel, Charles C., Max Pettini, and Kurt L. Adelberger (Jan. 2001). „Lyman-Continuum Emission from Galaxies at $z \approx 3.4$ “. In: *The Astrophysical Journal* 546.2, p. 665.
- Storchi-Bergmann, Thaisa, Daniela Calzetti, and Anne Louise Kinney (1994). „Ultraviolet to near-infrared spectral distributions of star-forming galaxies: Metallicity and age effects“. In: *The astrophysical journal. Chicago. Vol. 429, no. 2, pt. 1 (July 1994)*, p. 572-581.
- Tang, Mengtao, Daniel P Stark, Jacopo Chevallard, Stéphane Charlot, Ryan Endsley, and Enrico Congiu (2021). „Rest-frame UV spectroscopy of extreme [O iii] emitters at $1.3 < z < 3.7$: Toward a high-redshift UV reference sample for JWST“. In: *Monthly Notices of the Royal Astronomical Society* 501.3, pp. 3238–3257.
- Vanzella, Eros, S De Barros, Guido Cupani, W Karman, M Gronke, I Balestra, D Coe, Marco Mignoli, M Brusa, F Calura, *et al.* (2016). „High-resolution spectroscopy of a young, low-metallicity optically thin $L = 0.02 L^*$ star-forming galaxy at $z = 3.12$ “. In: *The Astrophysical Journal Letters* 821.2, p. L27.
- Vilchez, JM and C Esteban (1996). „The chemical composition of H II regions in the outer Galaxy“. In: *Monthly Notices of the Royal Astronomical Society* 280.3, pp. 720–734.
- Wang, H, R Cañameras, GB Caminha, SH Suyu, A Yıldırım, G Chirivì, L Christensen, C Grillo, and S Schuldt (2022). „Constraining the multi-scale dark-matter distribution in CASSOWARY 31 with strong gravitational lensing and stellar dynamics“. In: *Astronomy & Astrophysics* 668, A162.
- Wise, John H, Vasiliy G Demchenko, Martin T Halicek, Michael L Norman, Matthew J Turk, Tom Abel, and Britton D Smith (2014). „The birth of a galaxy–III. Propelling reionization with the faintest galaxies“. In: *Monthly Notices of the Royal Astronomical Society* 442.3, pp. 2560–2579.
- Zamorani, G, JP Henry, T Maccacaro, H Tananbaum, A Soltan, Y Avni, J Liebert, J Stocke, PA Strittmatter, RJ Weymann, *et al.* (1981). „X-ray studies of quasars with the Einstein Observatory. II“. In: *The Astrophysical Journal* 245, pp. 357–374.

Emission and absorption lines

A.1 S0

In this appendix, we show images of emission and absorption features not shown in the main text.

For the emission line, we use the blue profile to mark the emission profile of the Gaussian fit. The blue dotted line represents the center wavelength given by the fitting, and the area between the red dotted lines is the area used to calculate the equivalent width and flux. For profiles with different components, we use light blue dotted lines to represent individual components.

For absorption lines, the gray area is the part used to calculate the continuum. The blue dotted line marks the theoretical wavelength, and the area between the black dotted lines marks the part of the area used to calculate the equivalent width.

Table A.1.: S0(a) emission fitting

Line	Amplitude ($10^{-20} \text{ erg s}^{-1} \text{ cm}^{-2} \text{ \AA}^{-1}$)	Central wavelength (\AA)	FWHM (\AA)
Fe I 2523.6080	269.5803	2523.8132	1.7639
Fe II* 2612.6542	240.8336	2612.3098	1.6504
Fe II* 2626.4511	289.4205	2625.9405	2.1310

A.1.1 Emission

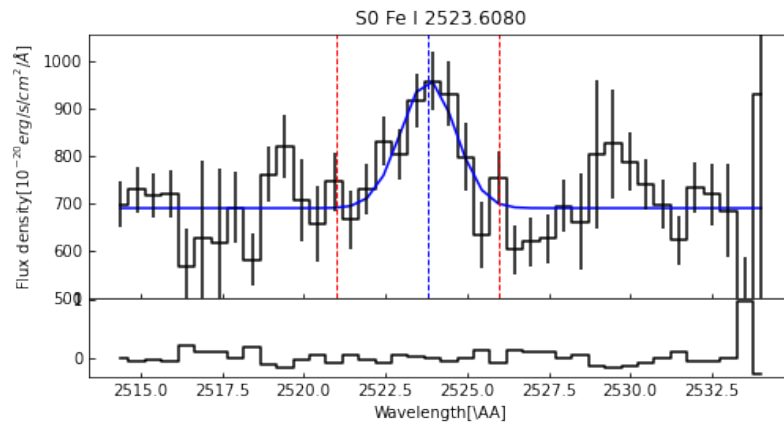


Figure A.1.: Fe I 2523.6080

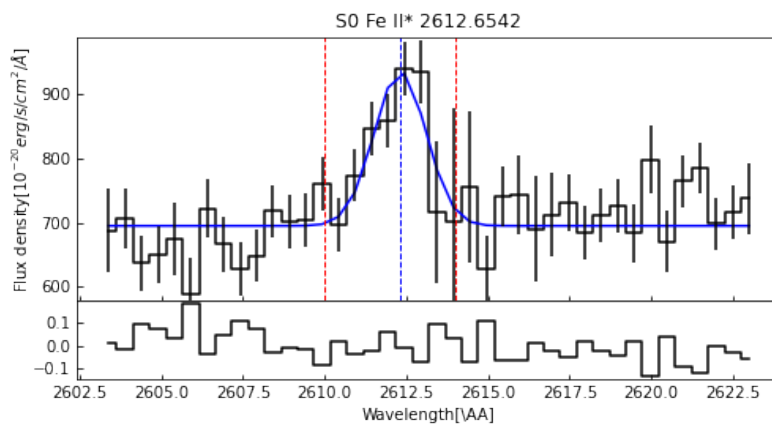


Figure A.2.: Fe II 2612

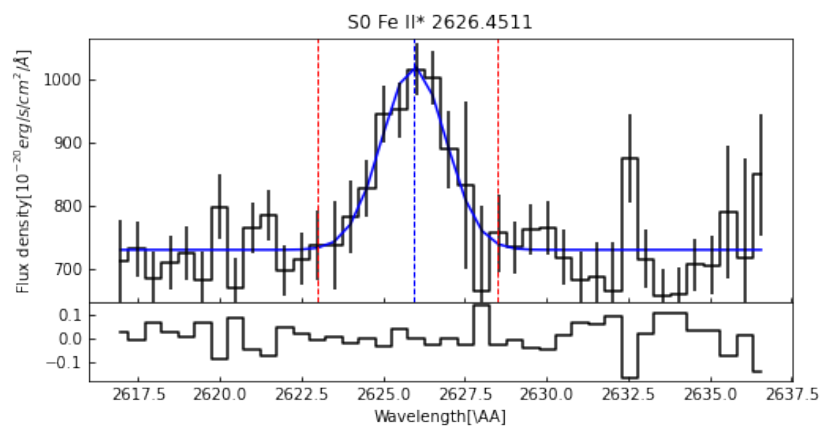


Figure A.3.: Fe II 2626

A.1.2 Absorption

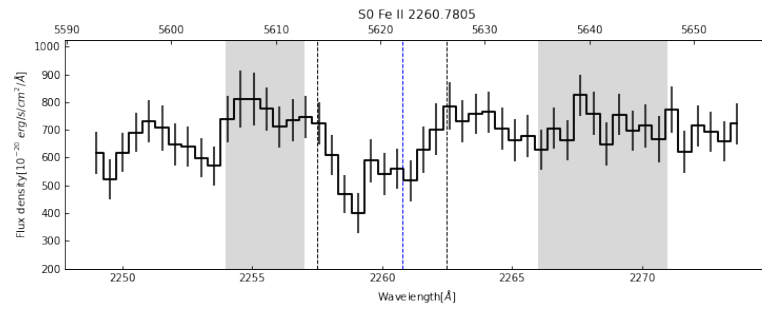


Figure A.4.: Fe II 2260

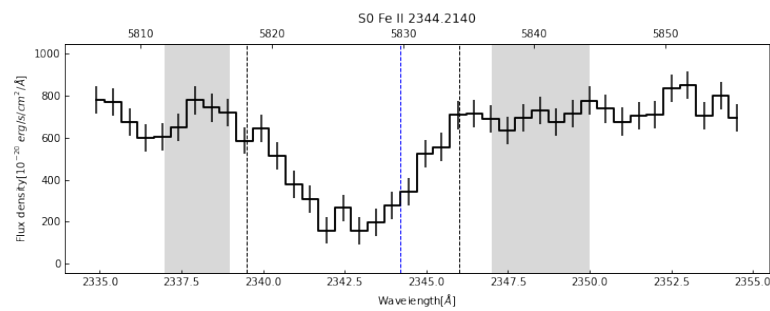


Figure A.5.: Fe II 2344

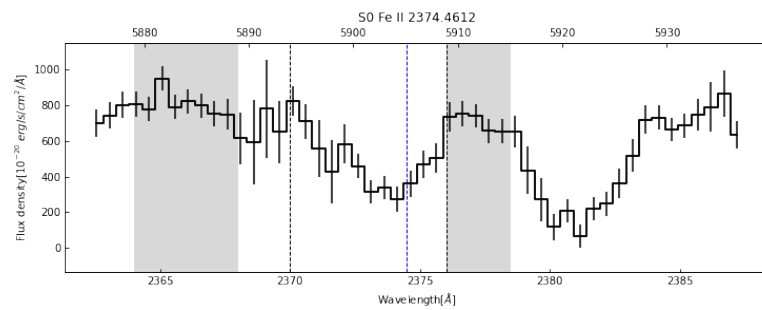


Figure A.6.: Fe II 2374

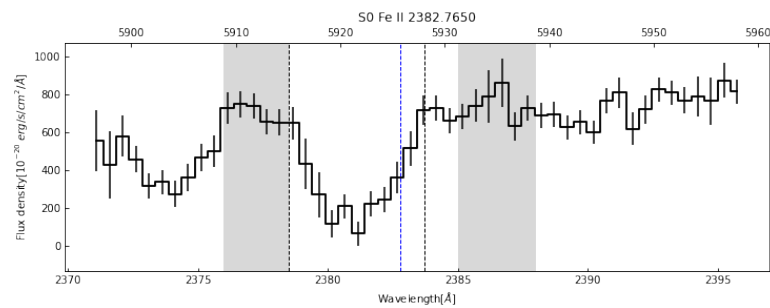


Figure A.7.: Fe II 2382

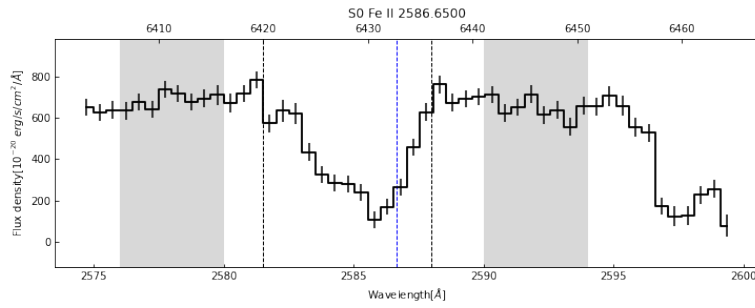


Figure A.8.: Fe II 2586

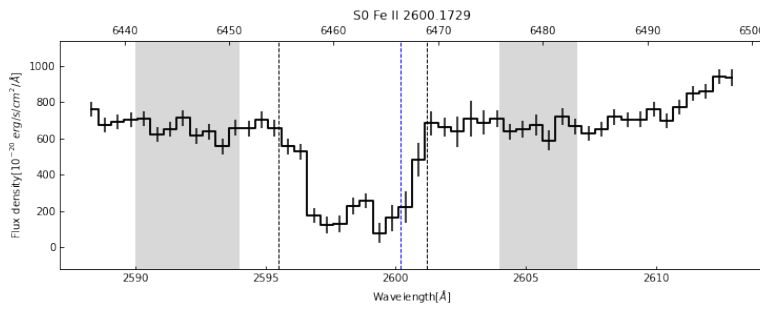


Figure A.9.: Fe II 2600

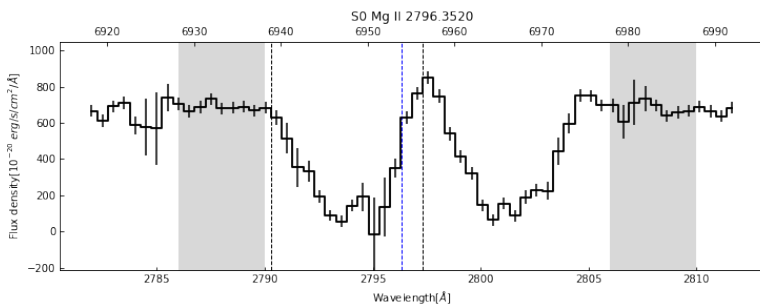


Figure A.10.: Mg II 2796

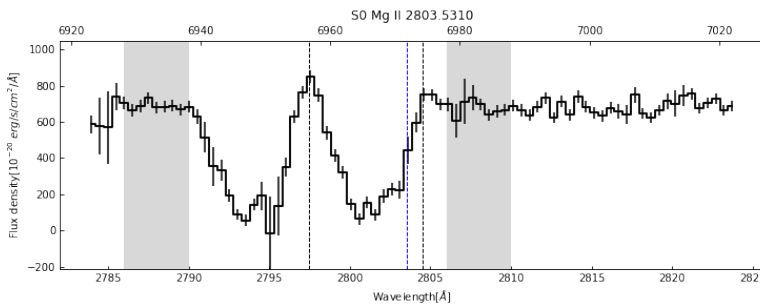


Figure A.11.: Mg II 2803

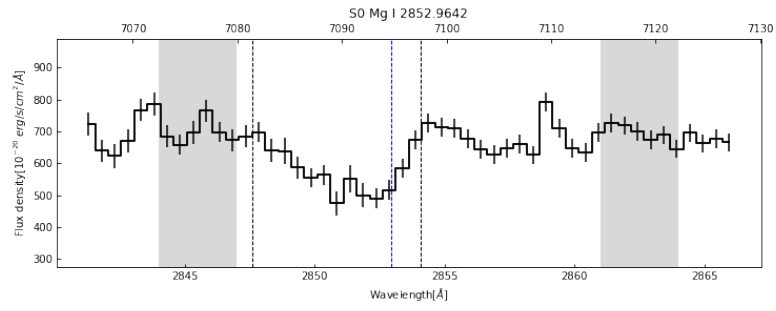


Figure A.12.: Mg I 2852

A.2 S3

A.2.1 Emission

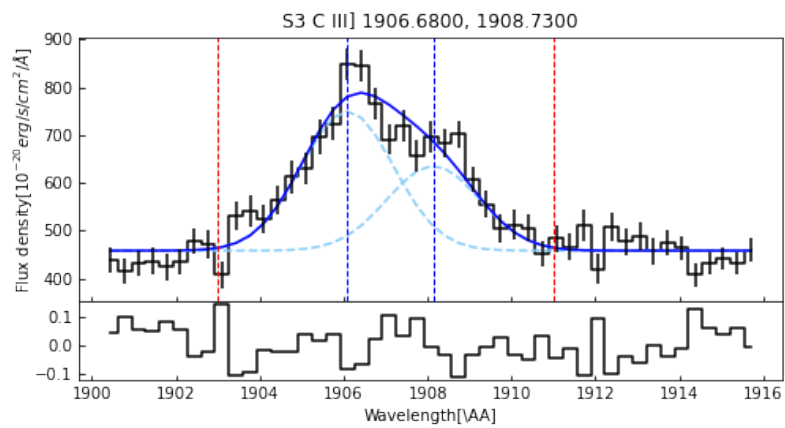


Figure A.13.: C III] 1906.6800, 1908.7300



Figure A.14.: C IV 1548.2000, 1550.7700

Table A.2.: S3(b) emission fitting

Line	Amplitude ($10^{-20} \text{erg s}^{-1} \text{cm}^{-2} \text{\AA}^{-1}$)	Central wavelength (\AA)	FWHM (\AA)
C III] 1906.6800	290.7825	1906.0862	2.5133
C III] 1908.7300	176.9488	1908.1356	2.5133
C IV 1548.2000	-	-	-
C IV 1550.7700	-	-	-

A.2.2 Absorption

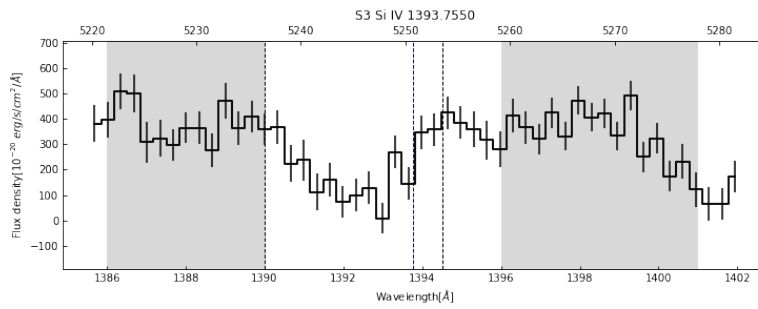


Figure A.15.: Si IV 1393

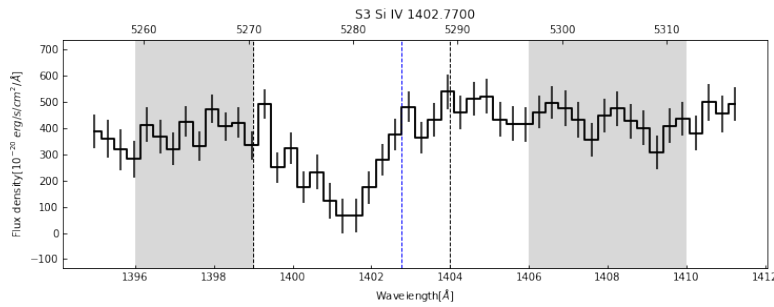


Figure A.16.: Si IV 1402

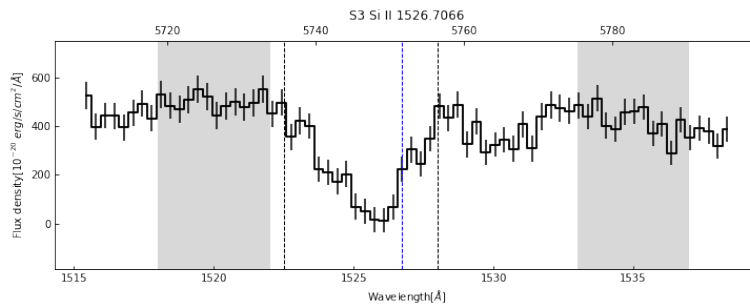


Figure A.17.: Si II 1526

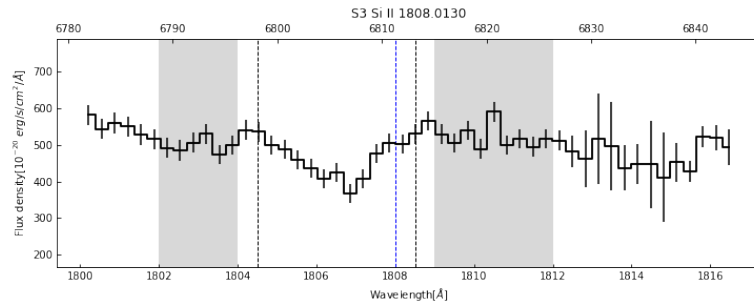


Figure A.18.: Si II 1808

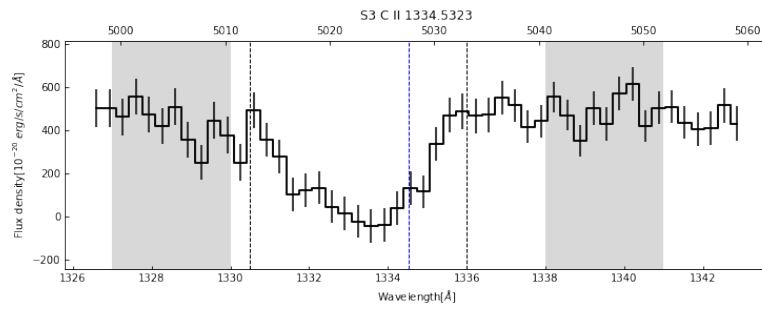


Figure A.19.: C II 1334

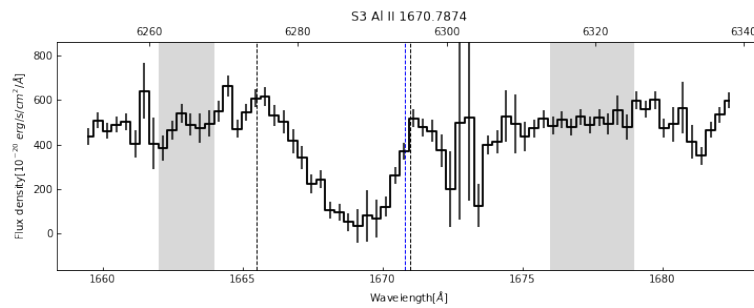


Figure A.20.: Al II 1670

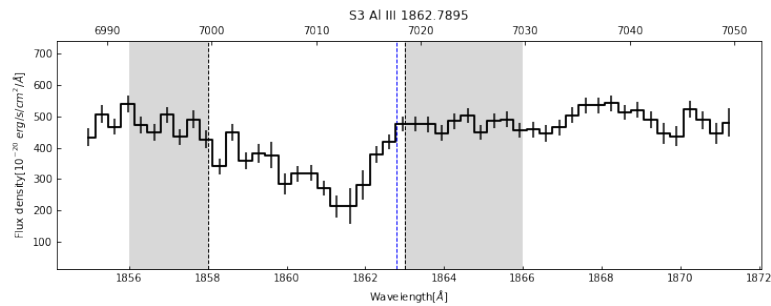


Figure A.21.: Al III 1862

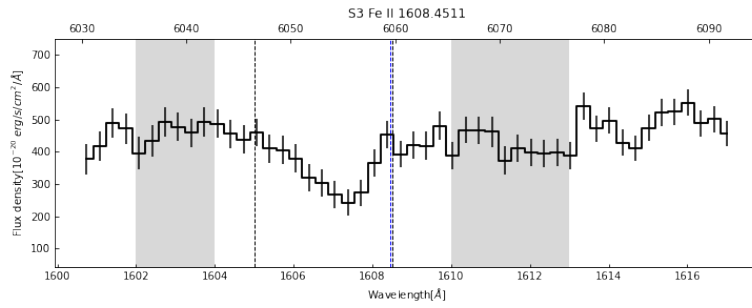


Figure A.22.: Fe II 1608

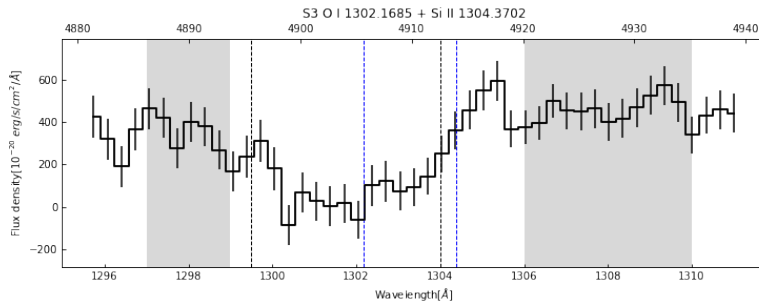


Figure A.23.: O I 1302.1685+ Si II 1304.3702

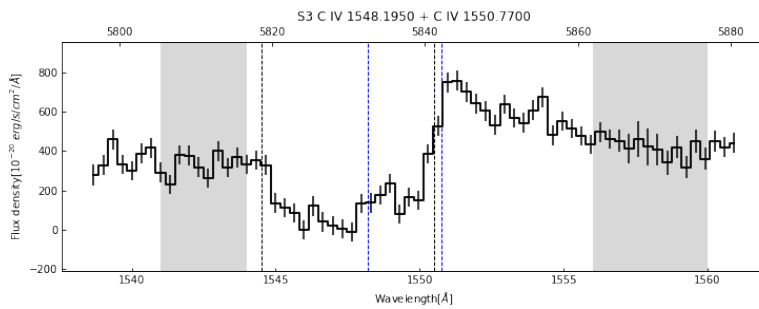


Figure A.24.: C IV 1548.1950, 1550.7700

A.3 Foreground object absorption

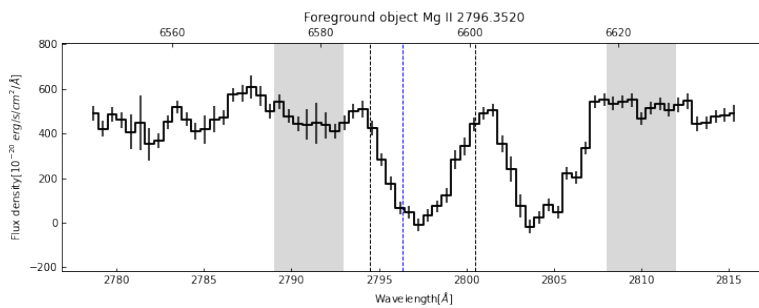


Figure A.25.: Mg II 2796

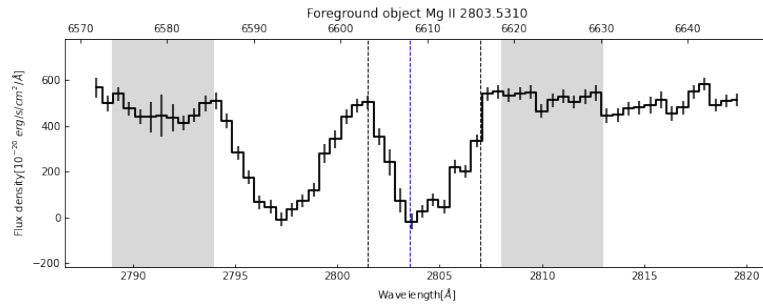


Figure A.26.: Mg II 2803

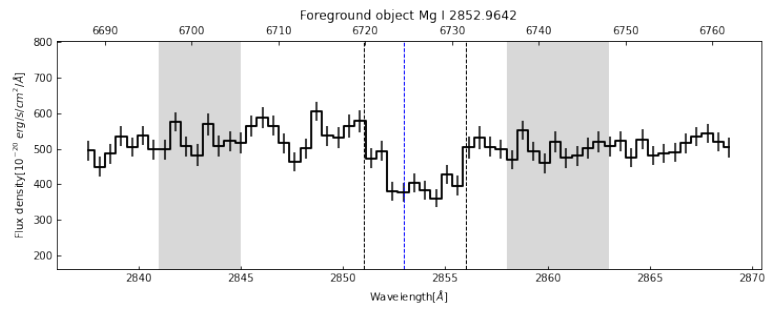


Figure A.27.: Mg I 2852

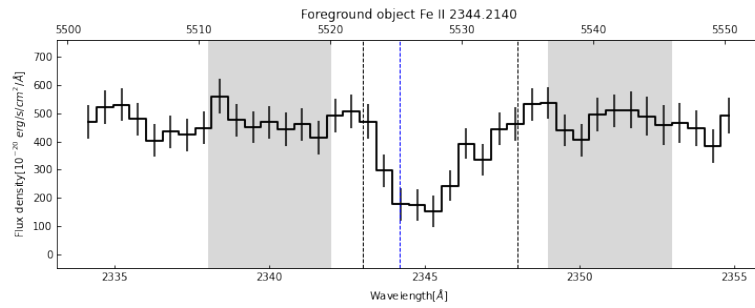


Figure A.28.: Fe II 2344

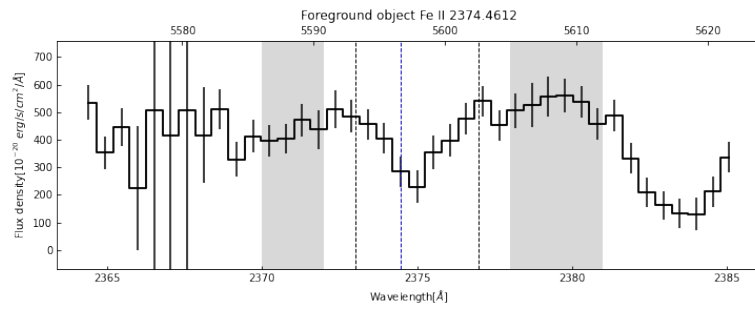


Figure A.29.: Fe II 2374

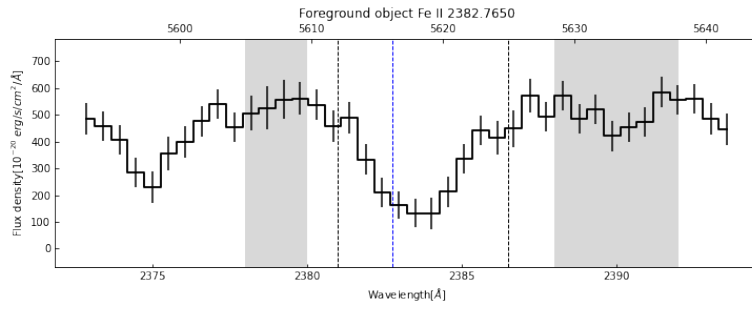


Figure A.30.: Fe II 2382

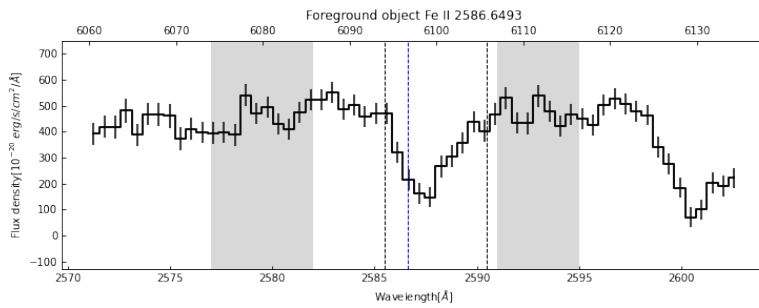


Figure A.31.: Fe II 2586

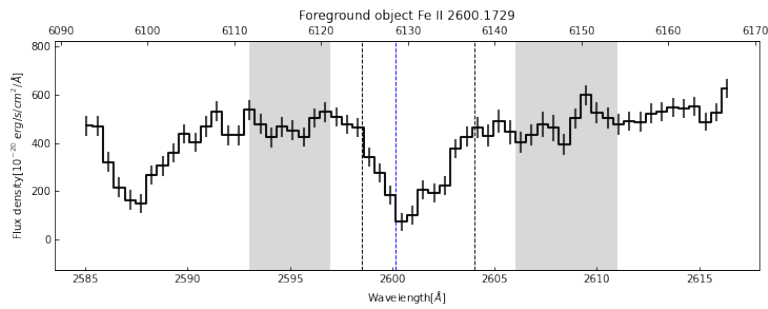


Figure A.32.: Fe II 2600